Institut für Physik und Astronomie
Astrophysik

Massive stars in the Galactic Center Quintuplet cluster

Dissertation
zur Erlangung des akademischen Grades
Doktor der Naturwissenschaften (Dr. rer. nat.)

eingereicht an der
Mathematisch-Naturwissenschaftlichen Fakultät
der Universität Potsdam

von
Adriane Liermann

Potsdam, Juni 2009

Published online at the
Institutional Repository of the University of Potsdam:
URL http://opus.kobv.de/ubp/volltexte/2009/3722/
URN urn:nbn:de:kobv:517-opus-37223
[http://nbn-resolving.org/urn:nbn:de:kobv:517-opus-37223]

Summary

The presented thesis describes the observations of the Galactic center Quintuplet cluster, the spectral analysis of the cluster Wolf-Rayet stars of the nitrogen sequence to determine their fundamental stellar parameters, and discusses the obtained results in a general context.

The Quintuplet cluster was discovered in one of the first infrared surveys of the Galactic center region (Okuda et al. 1987, 1989) and was observed for this project with the ESO-VLT near-infrared integral field instrument SINFONI-SPIFFI. The subsequent data reduction was performed in parts with a self-written pipeline to obtain flux-calibrated spectra of all objects detected in the imaged field of view. First results of the observation were compiled and published in a spectral catalog of 160 flux-calibrated K-band spectra in the range of 1.95 to 2.45 μm, containing 85 early-type (OB) stars, 62 late-type (KM) stars, and 13 Wolf-Rayet stars. About 100 of these stars are cataloged for the first time.

The main part of the thesis project was concentrated on the analysis of the WR stars of the nitrogen sequence and one further identified emission line star (Of/WN) with tailored Potsdam Wolf-Rayet (PoWR) models for expanding atmospheres (Hamann et al. 1995) that are applied to derive the stellar parameters of these stars. For this purpose, the atomic input data of the PoWR models had to be extended by further line transitions in the near-infrared spectral range to enable adaequate model spectra to be calculated. These models were then fitted to the observed spectra, revealing typical paramters for this class of stars.

A significant amount of hydrogen of up to $X_{\rm H} \sim 0.2$ by mass fraction is still present in their stellar atmospheres. The stars are also found to be very luminous ($\log(L/L_\odot) > 6.0$) and show mass-loss rates and wind characteristics typical for radiation-driven winds. By comparison with stellar evolutionary models (Meynet & Maeder 2003a; Langer et al. 1994), the initial masses were estimated and indicate that the Quintuplet WN stars are descendants from the most massive O stars with $M_{\rm init} > 60 M_\odot$ and their ages correspond to a cluster age of 3-5 million years.

The analysis of the individual WN stars revealed an average extinction of $A_K = 3.1 \pm 0.5$ mag ($A_V = 27 \pm 4$) towards the Quintuplet cluster. This extinction was applied to derive the stellar luminosities of the remaining early-type and late-type stars in the catalog and a Hertzsprung-Russell diagram could be compiled. Surprisingly, two stellar populations are found, a group of main sequence OB stars and a group of evolved late-type stars, i.e. red supergiants (RSG). The main sequence stars indicate a cluster age of 4 million years, which would be too young for red supergiants to be already present. A star formation event lasting for a few million years might possibly explain the Quintuplet's population and the cluster would still be considered coeval. However, the unexpected and simultaneous presence of red supergiants and Wolf-Rayet stars in the cluster points out that the details of star formation and cluster evolution are not yet well understood for the Quintuplet cluster.

Zusammenfassung

Die vorgelegte Arbeit befasst sich mit der Spektralanalyse der massereichen Sterne, speziell der Wolf-Rayet Sterne der Stickstoffsequenz, des Quintuplet-Sternhaufens im Galaktischen Zentrum, welches durch Staubwolken vor visuellen Beobachtungen verborgen ist. Der Sternhaufen wurde in einer der ersten Infrarot-Durchmusterungen entdeckt (Okuda et al. 1987, 1989) und für dieses Projekt mit dem Großteleskop ESO-VLT und dem Infrarotinstrument SINFONI-SPIFFI beobachtet. Die Daten wurden aufbereitet und die flusskalibrierten Spektren in einem Katalog veröffentlicht. Darin enthalten sind 85 Sterne frühen Spektraltyps (O- und B-Sterne), 62 Sterne späten Spektraltyps (K- und M-Sterne), sowie 13 Wolf-Rayet Sterne. Etwa 100 Sterne sind zum ersten mal detektiert und katalogisiert worden.

Die flusskalibrierten Spektren der Wolf-Rayet Sterne der Stickstoffsequenz (WN) wurden mit den Potsdam Wolf-Rayet Modellen für expandierende Sternatmosphären (Hamann et al. 1995) untersucht, wozu zunächst Atomdaten der Modelle für den Infrarotbereich ergänzt werden mussten. Verschiedene Modellspektren und -energieverteilungen wurden mit den Beobachtungen verglichen, um die Sternparameter Temperatur, Radius, Leuchtkraft und die Charakteristik des Sternwinds Geschwindigkeit, chemische Zusammensetzung und Massenverlustrate zu bestimmen. Der ermittelte hohe Wasserstoffgehalt der Winde der WN-Sterne zeigt, dass sie Abkömmlinge von massereichen O-Sternen sind, die die Hauptreihe verlassen haben. Desweiteren sind die Sterne sehr leuchtkräftig ($\log(L/L_\odot) > 6$) und zeigen Massenverlustraten, die typisch sind für strahlungsgetriebenen Sternwinde. Im Vergleich mit Sternentwicklungsmodellen (Meynet & Maeder 2003a; Langer et al. 1994) ergeben sich Anfangsmassen von $M_{\rm init} > 60\,M_\odot$, sowie ungefähre Sternalter von 3-5 Millionen Jahren für die WN-Sterne, was dem angenommenen Altern des Quintuplet-Haufens entspricht.

Durch die Analyse der spektralen Energieverteilungen der einzelnen WN-Sterne konnte eine mittlere interstellare Extinktion von $A_K = 3.1 \pm 0.5\,\mathrm{mag}$ ($A_V = 27 \pm 4\,\mathrm{mag}$) in der Richtung des Quintuplet-Haufens ermittelt und für die Bestimmung der Leuchtkräfte der verbleibenden Sterne des Katalog verwendet werden. Die anschließende vorläufige Analyse ergab eine Dichotomie der Sternpopulation von frühen und späten Sternen im Hertzsprung-Russell-Diagramm. Während die OB-Sterne entsprechend der Entwicklungstheorie auf der Hauptreihe des Haufens liegen, befinden sich die KM-Sterne im entwickelten Stadium der Roten Riesen, welches für Sterne diesen Typs frühestens nach 7 Millionen Jahren erwartet wird. Somit steht die zeitgleiche Entstehung aller Sterne des Sternhaufens in Frage. Sie wird im Rahmen von Haufenzugehörigkeit und einer Phase ausgedehnter Sternentstehung diskutiert. Es bleibt anzuerkennen, dass die Sternentstehung und -entwicklung auch im speziellen Fall des Quintuplet-Haufens noch nicht hinreichend gut verstanden sind.

Contents

List of Figures

List of Tables

"Wir alle aber, die wir an dem weiteren Ausbau einzelner Zweige der Wissenschaft arbeiten, können unsere Zeit nur zu einem sehr kleinen Theile auf das gleichzeitige Studium anderer Theile derselben verwenden. Wir müssen, sobald wir irgend eine einzelne Untersuchung vornehmen, alle unsere Kräfte auf ein eng begrenztes Feld concentriren. Wir haben nicht nur, wie der Philologe oder Historiker, Bücher herbeizuschaffen und durchzusehen, Notizen zu sammeln von dem, was Andere schon über denselben Gegenstand gefunden haben; das ist im Gegentheil nur ein untergeordneter Theil unserer Arbeit. Wir müssen die Dinge selbst angreifen, und jedes von ihnen bietet seine neuen und eigenthümlichen Schwierigkeiten von ganz anderer Art, als der Büchergelehrte sie kennt. Und was am meisten Zeit und Arbeit kostet, sind in der Mehrzahl der Fälle Nebendinge, die nur in entfernter Verbindung mit dem Ziele der Untersuchung stehen."

H. von Helmholtz, "Über das Ziel und die Fortschritte der Naturwissenschaft." Eröffnungsrede für die Naturforscherversammlung zu Innsbruck, (1869)

Chapter 1

Introduction

1.1 The Galactic Center

From early radio observations we know that a strong, variable radio source, Sagittarius A*, resides in the center of the Milky Way. The state-of-the-art assumption is that a black hole is found in the center of every galaxy, some in quiescent state, i.e. non-accreting, others in non-quiescent state, i.e. accreting. Observations confirmed accreting black holes in extra-galactic objects such as Active Galactic Nuclei (AGN) or Quasars (QSO) of several millions of solar masses (supermassive black holes). In contrast to these objects, the nature of Sagittarius A* is considered to be a supermassive black hole in its quiescent state, which is not accreting at all or temporarily only on very low rates. Unfortunately, the Galactic center is shielded by dust lanes which strongly absorb light in the ultraviolet (UV) and visual spectral range. Thus further investigations of the Galactic center region beyond radio observations became only possible in the past decade with new instruments for the infrared spectral range (IR).

With the first near-IR photometric studies of the Galactic center, three surprisingly young and massive stellar clusters were found within 35 pc projected distance from Sagittarius A*: the Arches, the Quintuplet and the Central Parsec cluster. These clusters are rich in massive stars (Arches: Blum et al. 2001; Figer 2004; Martins et al. 2008; Quintuplet: Figer et al. 1997, 1999a; Figer 2004; Galactic center: Eckart et al. 2004; Figer 2004).

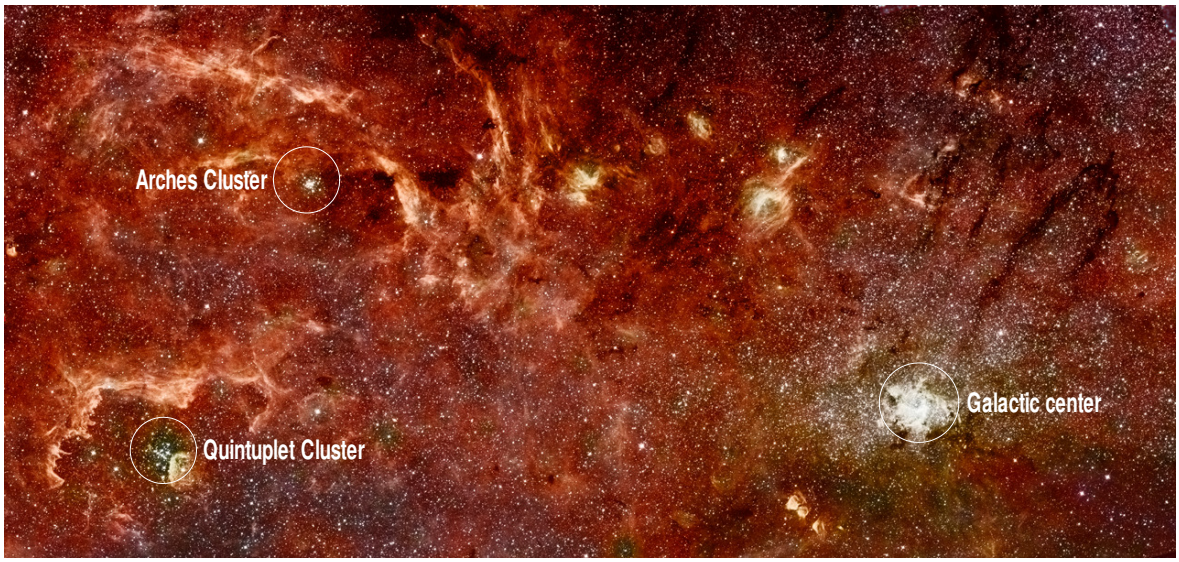

Figure 1.1: Composite infrared image of the Galactic center region from the Hubble Space Telescope (HST) and Spitzer Space Telescope (Spitzer). The Quintuplet cluster is in the lower left, the Arches cluster in the upper left below the stretched arch-like filaments and the Galactic center with the Central Parsec cluster around Sgr A* in the lower right.

The Quintuplet cluster The prominent constellation of five IR-bright stars gave reason to name the cluster the "Quintuplet cluster" (Okuda et al. 1987, 1989). It has a projected distance of 30 pc to the Galactic center, a cluster radius of about 1 pc, and an estimated age of about 4 million years (Okuda et al. 1990; Figer et al. 1999a).

The first spectroscopic observations of the five "Quintuplet proper" stars (later named Q1, Q2, Q3, Q4, and Q9 by Figer et al. 1999a) showed only a continuum without any spectral features. Later some of them were detected as far-IR and radio sources (Lang et al. 1997, 1999, 2005) as well. Tuthill et al. (2006) resolved two of the original Quintuplet stars (Q2

and Q3) spatially and in time as colliding wind binaries (CWB), ejecting dust in the shape of a rotating "pinwheel". According to further spectroscopic studies (Figer et al. 1999a; Figer 2004), the cluster contains at least 100 O stars and 16 Wolf-Rayet stars. Two massive evolved stars in their luminous blue variable (LBV) phase, the well known Pistol star and one further LBV candidate, qF 362, were found within the Quintuplet cluster (Geballe et al. 2000). Additionally, two stars of late spectral types K and M were found in the cluster as well (Glass et al. 1990). Hence, this cluster appears to be a very interesting case to study massive stars and their evolutionary phases from the main sequence to Wolf-Rayet stars in the vicinity of the Galactic central black hole.

1.2 High-mass Stars and Wolf-Rayet Stars

High-mass stars, the terms "high-mass star" and "massive star" will be used synonymously in the following, have initial masses of at least 8 solar masses ($M_\odot$) and determine their lives as supernova. These stars process hydrogen to helium via the CNO cycle in their center, core-hydrogen burning (CHB), to sustain their luminosities and to ensure hydrostatic equilibrium while being on the main sequence. Additionally, these stars are characterized by stellar winds that cause a continuous mass-loss, which has great impact on the further evolution. In the Hertzsprung-Russell diagram (HRD), massive stars populate the upper left region on the main sequence, they are of spectral types O and B, see Fig. 1.2. Depending on their initial masses

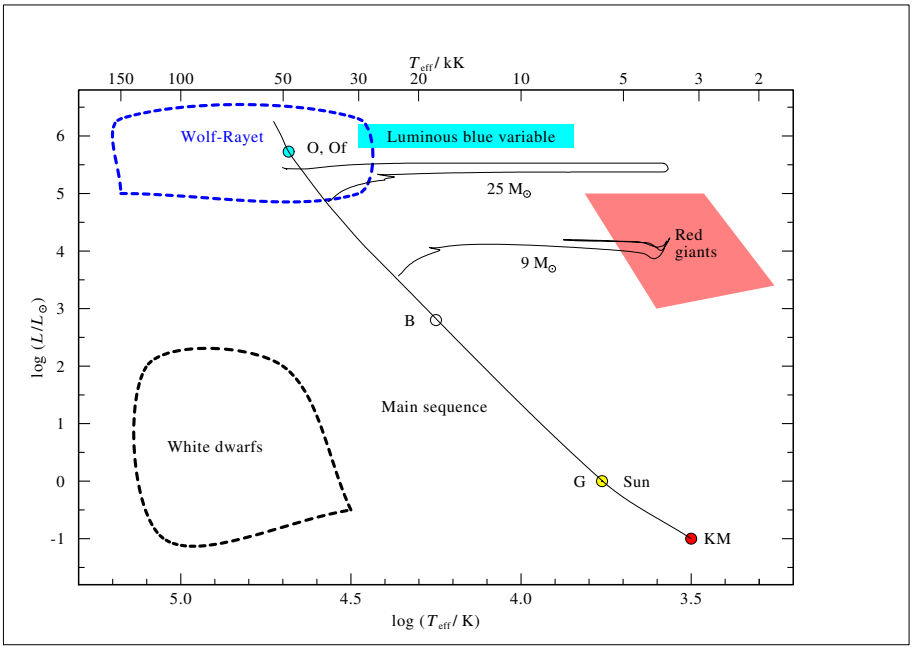

Figure 1.2: Hertzsprung-Russell diagram showing the main sequence with late-type stars (KM stars), the Sun, and early-type stars (OB stars). Additionally, regions for specific evolutionary phases are indicated: red (super-) giants, luminous blue variables, Wolf-Rayet stars, and white dwarfs.

the stars follow different evolutionary tracks in the HRD. Low-mass stars like the Sun will become red giants, loose outer shells of their stellar atmospheres and cool slowly down as white dwarfs. OB stars with higher initial masses become red super giants (RSG) and might

even pass the luminous blue variable (LBV) phase before they explode as supernova (SN). To become a Wolf-Rayet (WR) star in the Milky Way, the star has to have at least 25 $M_\odot$ initial mass, but it is not yet know in detail if the stars passes the RSG and the LBV phase or might skip either of them before it becomes a WR star. Finally, it will explode as SN.

WR stars are important for the chemical evolution of the universe. Their short lifetimes, strong radiation fields, and strong stellar winds give fast feedback to the ambient medium by mechanical energy, ionizing photons, and nuclear processed material. In this way, the stars enrich the interstellar medium (ISM) with metals, blow circumstellar bubbles and drive shocks in the ISM that might trigger or terminate stars formation processes nearby. Massive stars passing the WR phase are also suspected to represent the first stars after the Big Bang, which re-ionized the early universe and enriched it chemically for further generations of stars.

The observed spectra of WR stars display broad emission lines in the UV/visual spectral range by which they are classified spectroscopically (e.g. van der Hucht 2001). Lines of highly ionized elements indicate high stellar temperatures, while the broad emission line profiles are interpreted to arise in a fast extending atmosphere. However, the WN stars analyzed in this work cannot be observed in the classical spectral range due to the high interstellar extinction towards the Galactic center, but are studied in the infrared range.

1.3 Scope of this work

The discovery of young clusters hosting massive stars in the vicinity of the supermassive black hole in the Galactic center give rise to numerous questions, e.g.

- Where do stars form in the Galactic center regions and is star formation different in the Galactic center?
- How can stellar cluster survive so close to the supermassive black hole in the Galactic center?
- What is the stellar population of these clusters and what are the stellar parameters of the stars?
- Why do the Galactic center clusters seem to host so many massive stars compared to other regions in the Galaxy?

Unfortunately, it is out of limits of this thesis to answer all of these questions. Some require the expertise of specific fields of research on their on, such as high-mass star formation and cluster dynamics and evolution. This work focuses on the analysis of the most massive evolved stars within the Quintuplet cluster, to determine their fundamental stellar parameters and evolutionary phase. The following chapter 2 describes the obtained observations of the Quintuplet cluster and the data reduction process. Chapter 3 introduces the model atmospheres, which were applied in chapter 4 for the analysis of the Quintuplet WN stars. Finally, chapter 5 gives an overview to the general cluster properties. This thesis concludes with a context-biased outlook in chapter 6.

Chapter 2

Observations & the spectral catalog

In this chapter, we will introduce the observational data obtained at the ESO-VLT, describe the data reduction process and present the available spectral catalog (hereafter the "LHO catalog") for the stars of Quintuplet cluster (see also Liermann et al. 2009).

2.1 Observations

2.1.1 The data

Observations were obtained in service mode with the ESO-VLT UT4 (Yepun) telescope between May and July 2006 using the integral field spectrograph of the SINFONI [1] instrument, that allows to obtain imaging and spectral information simultaneously. The observations were taken in 22 observation blocks (OBs) covering the dense center of the cluster with slightly overlapping fields each of $8''\times 8''$ field of view (FOV), see Fig. 2.1. However, the adaptive optics module could not be used since no suitable guide star is available in the region to observe and the laser guide star was not offered in the period (P77). The deformable mirror was adjusted according to the wavefront sensor at the beginning of the observational run. Therefore, the observations are seeing limited. Standard ABBA cycles were performed with an alternating pointing to the science field (A) and a nearby blank sky field (B), with an exposure time of 2×5 min on each field. This observational pattern is crucial for infrared (IR) observations since molecular OH emission [2] of the night sky can severely affect the science data, and thus have to be subtracted carefully. The spectral coverage of the observations is limited to the infra-red K-band (1.95 - 2.45 μm), with a spectral resolution of $R \approx 4000$, since prominent hydrogen and helium lines of massive stars are to be expected here. Table 2.1 gives an overview of the observations with their date and the center coordinates of the $8''\times 8''$ FOV.

For appropriate data reduction and flux calibration of the spectra, bias and flat-field frames were taken, and standard stars were observed, the latter at airmasses similar to those of the science observations.

2.1.2 Data reduction

Data reduction was severely hampered by the fact that the chosen sky fields of the observations were not blank, but accidentally did contain stars in some cases. Therefore the sky frames were useless, as these "contaminating stars" would result in negative fluxes and holes in the reduced science data. The first attempts of the data reduction were performed with the official ESO-SINFONI pipeline but soon turned out to be not good enough, leaving residual sky emission lines in the resulting data (see below).

Data reduction was then performed using the SPRED software (Abuter et al. 2006) from the Max-Planck-Institute for Extraterrestrial Physics, Garching, which is an "inofficial pipeline" from the working group that has built the SPIFFI instrument. However, due to the bad quality

[1] SINFONI = Spectrograph for INtegral Field Observations in the Near Infrared, consisting of an adaptive optics module (MACAO) and a SPectrometer for Infrared Faint Field Imaging (SPIFFI) http://www.eso.org/sci/facilities/paranal/instruments/sinfoni/

[2] In the Earth's atmosphere up to about 80 km altitude the chemical reduction of ozone to oxygen takes places via the ozone-oxygen cycle. In this process atmospheric ozone is produces by photo-dissociation of molecular oxygen. Under the influence of ultra-violet photons and with the production of chemical radicals such as nitroxyl and hydroxyl the ozone can be reduced to oxygen. The reaction $H + O_3 \rightarrow OH + O_2$ is one main channel to reduce ozone and leaves the hydroxyl to absorb part of the heat of the reaction. The molecule basically emits in the spectral range between 0.85 and 2.2 μm, the near-IR bands J, H, and K.

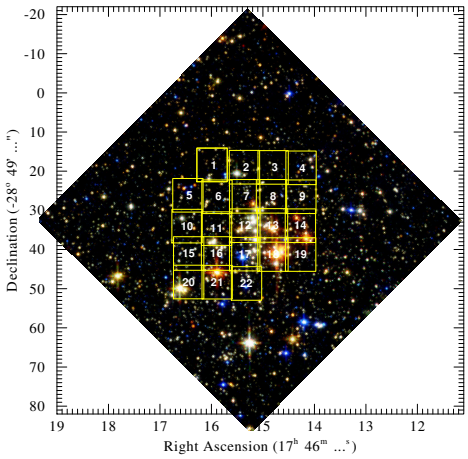

Figure 2.1: The 22 observed fields, overlayed on an HST composite image (HST Heritage archive).

Table 2.1: List of observation blocks (OBs). Running numbers of the names of individual OBs refer to the fields in Fig. 2.1.

OB-ID	Name of OB	Date 2006	R.A. $17^h\ 46^m$	Dec. $-28°\ 49'$
229060	Quintuplet-01	18.05.	$15^s.99$	$18''.4$
229062	Quintuplet-02	01.06.	$15^s.36$	$19''.0$
229064	Quintuplet-03	01.06.	$14^s.80$	$19''.0$
229066	Quintuplet-04	07.06.	$14^s.26$	$19''.1$
229068	Quintuplet-05	07.06.	$16^s.46$	$26''.1$
229070	Quintuplet-06	07.06.	$15^s.89$	$26''.5$
229072	Quintuplet-07	24.06.	$15^s.35$	$26''.4$
229074	Quintuplet-08	24.06.	$14^s.83$	$26''.4$
229076	Quintuplet-09	24.06.	$14^s.26$	$26''.5$
229078	Quintuplet-10	24.06.	$16^s.47$	$34''.0$
229080	Quintuplet-11	24.06.	$15^s.90$	$34''.7$
229082	Quintuplet-12	24.06.	$15^s.37$	$33''.9$
229084	Quintuplet-13	24.06.	$14^s.81$	$33''.9$
229086	Quintuplet-14	24.06.	$14^s.27$	$33''.9$
229088	Quintuplet-15	24.06.	$16^s.44$	$41''.0$
229090	Quintuplet-16	24.06.	$15^s.90$	$41''.0$
229092	Quintuplet-17	29.06.	$15^s.35$	$41''.2$
229094	Quintuplet-18	29.06.	$14^s.81$	$41''.3$
229096	Quintuplet-19	29.06.	$14^s.27$	$41''.3$
229098	Quintuplet-20	30.06.	$16^s.44$	$48''.3$
229100	Quintuplet-21	01.07.	$15^s.89$	$48''.3$
229102	Quintuplet-22	01.07.	$15^s.32$	$48''.7$

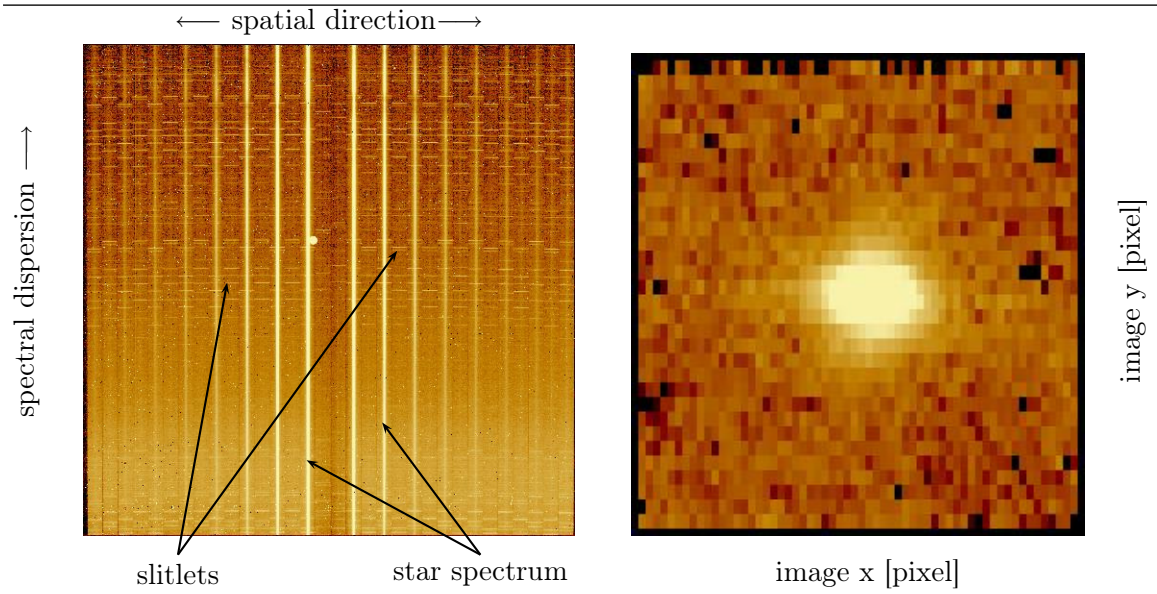

Figure 2.2: Detector raw image (left) of one observed standard star with slitlets of the spectrally dispersed star; resulting monochromatic cube layer imaging the standard star (right).

of the obtained sky fields the science raw frames were only corrected for bad pixels, distortion, and flat field, followed by the wavelength calibration. The important sky subtraction was skipped at this point of the data reduction, and carried out at a later point (see below). A detector raw frame is shown in the left panel of Fig. 2.2 with the spectrally dispersed image parts, i.e. slitlets, and the spectrum of the observed object (bright lines along the direction of dispersion). These slitlets were then stacked into a data cube according to their spatial position in the field of view. The data cube consists of layers of monochromatic two-dimensional images (x, y) along the spectral axis ($z = \lambda$), see right panel of Fig. 2.2. This limited pipeline reduction was applied to the science data as well as to the standard-star observations.

For further data reduction, sky subtraction was performed first for the standard stars, then for the science data. To overcome the drawback of bad-quality sky fields, a "star-free" subarray was defined within each pre-reduced data cube. This subarray was split into its monochromatic layers and the median for each layer was determined, the "monochromatic median" in the following. For these steps, a self-written IDL routine consisting of three parts was used.

STD-MUSIQ The standard star (STD) sky subtraction was performed first, since they are crucial elements for the flux-calibration of the science data. The monochromatic median was subtracted as local sky from each wavelength layer. Then, the standard star spectra were extracted by adding all pixels within a predefined extraction radius, a synthetic aperture. For each standard star spectrum a Kurucz model (Kurucz 1993) was identified according to the spectral type of the star (between types B and G), and scaled to the star's 2MASS K_s-band magnitude (Skrutskie et al. 2006). Then the ratio between the model flux and standard star spectrum was calculated. This ratio is the calibration curve for the flux calibration of the science data. The Kurucz models do not perfectly reproduce the Br γ line; the residual feature in the calibration curve had to be smoothed out by interpolation between 2.15 and 2.17 μm.

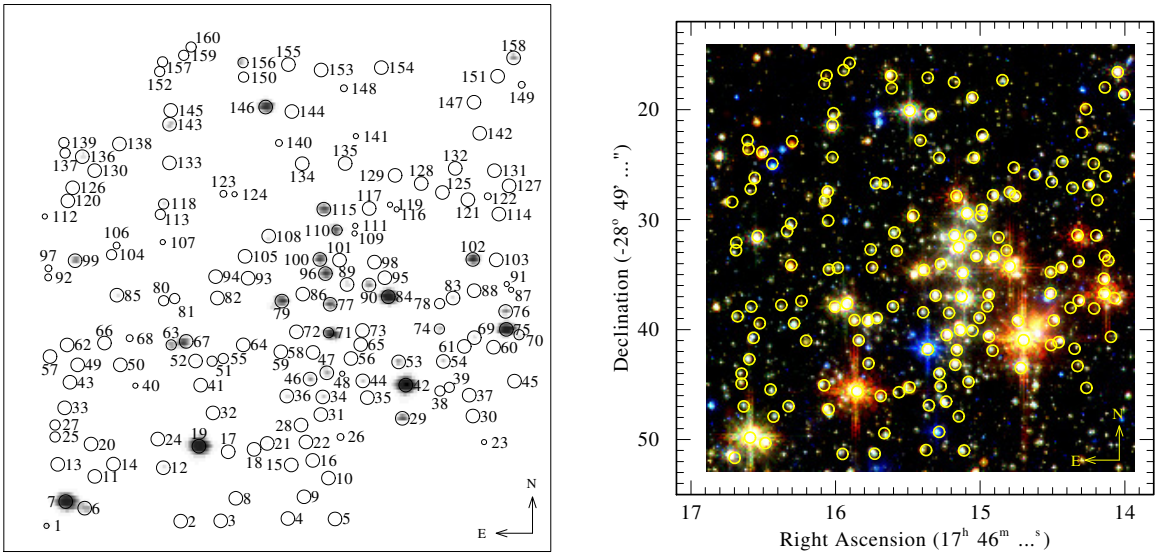

Figure 2.3: *Left:* Gray-scale image of the collapsed final grand mosaic cube. Open circles mark the detected sources with their running number in the LHO catalog. Circle radii correspond to the synthetic apertures for the object spectra. *Right:* Detected sources in the Quintuplet cluster as overlay on a detail of the HST composite image (compare to the figure on the right for object identification; note that figures have not the same scale).

CALIBMUSIQ Sky subtraction for the science observations was performed with a monochromatic median of a pre-defined "star-free" subarray of each cube, too. Subsequently, the science data were flux-calibrated by multiplying each cube wavelength plane with the corresponding value of the corresponding calibration curve. In a final step all 22 cubes were combined into one grand mosaic cube. For this purpose, 2D images were generated for all cubes by "collapsing" the data cubes to passband images. The spacial offsets between the OBs were determined by manually overlaying them on the HST composite by D. Figer (HST program 7364, STScI-PRC1990-30b, see Fig. 2.3). In overlapping regions, the flux per pixel was averaged.

SPECTRAL-MUSIQ The last part of the IDL cascade takes the grand mosaic cube, collapses it to a passband image, and runs an automated search for point source detection on this image. The number of detected sources was refined by comparison with the cube passband image and the HST image. Parameters for the source detection were fine tuned. In total, 160 point sources were detected, see Fig. 2.3. For each source, a spectrum was extracted from the grand mosaic cube with an extraction radius generally set to 4 pixels. A smaller synthetic aperture had to be chosen for stars which have close neighbors or are at the borders of the mosaic cube. In any case the applied calibration curve was based on standard star spectra extracted with the same aperture.

However, some extracted spectra still show sharp emission-line peaks, especially those of the fainter objects. These peaks are caused by telluric OH contamination (see Fig. 2.4), a residual of the imperfect work-around for the sky subtraction.

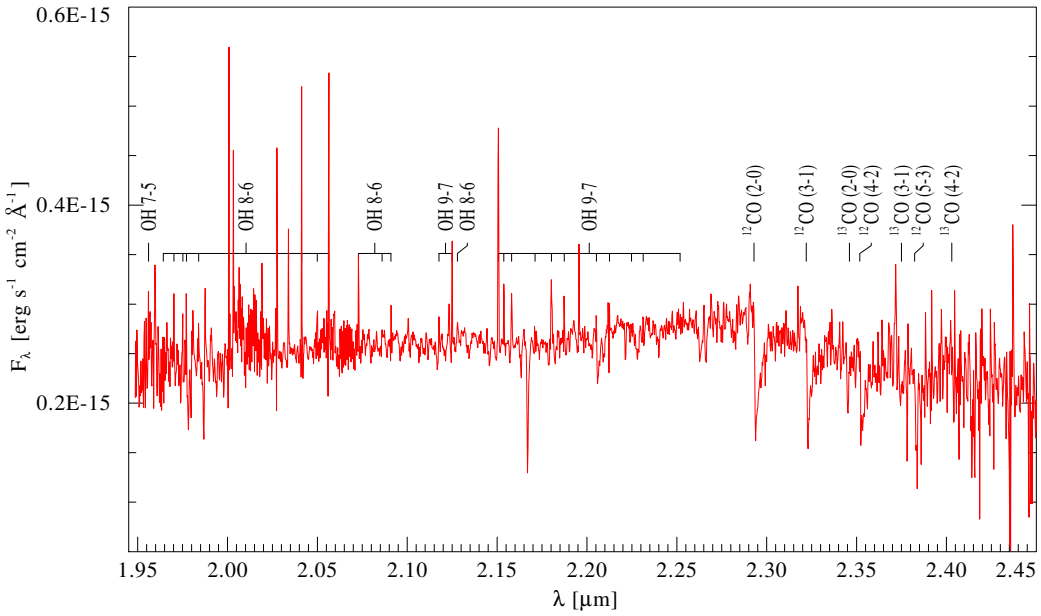

Figure 2.4: Flux-calibrated K-band spectrum of an M star (LHO 4). Identifications for the telluric OH lines are from Rousselot et al. (2000). The prominent molecular absorption bands are produced by CO. Their identifications are based on Gorlova et al. (2006) and Wallace & Hinkle (1997). Note the different absorption bands of the ^{12}CO and ^{13}CO.

2.2 The catalog

2.2.1 Coordinates and identification

Coordinates of the detected sources were derived with a linear transformation. Their map-coordinates (in pixels) were superimposed on the HST image of the field. Well-known positions of foreground stars from the USNO-B catalog (Monet et al. 2003) were used to orientate the overlay and verify the mapping between pixel positions and celestial coordinates. The resulting overlay is shown in Fig. 2.3 (right) and Table B.1 lists all 160 extracted sources with their running number in the LHO catalog (column 1), followed by the coordinates (right ascension and declination) in columns 2 and 3.

The SIMBAD database [3] was employed to find cross-identifications with known objects. The results were verified with the literature and finally listed Table B.1, column 7. However, this is not considered to be a complete list of alias names and references. For example, Lang et al. (2005) detected three radio sources QR 1, QR 2, and QR 3 in the Quintuplet region which cannot be identified with near-IR counterparts. The LHO catalog only confirms the absence of K-band counterparts for these radio sources in the data.

2.2.2 Spectral classification

OB stars For the classification of the OB stars we followed Hanson et al. (1996, 2005) and Morris et al. (1996), and concentrated on the most prominent lines in the K-band region: He I $\lambda\,2.0587\,\mu$m, C IV triplet around $\lambda\,2.0796\,\mu$m, N III/C III $\lambda\,2.1155\,\mu$m, H I $\lambda\,2.1661\,\mu$m (Br γ), He II $\lambda\,2.1891\,\mu$m. Furthermore, the He I lines $\lambda\,2.1127/37\,\mu$m, $\lambda\,2.1499\,\mu$m, and $\lambda\,2.1623\,\mu$m

[3] This research has made use of the SIMBAD database, operated at CDS, Strasbourg, France: http://simbad.u-strasbg.fr/simbad/

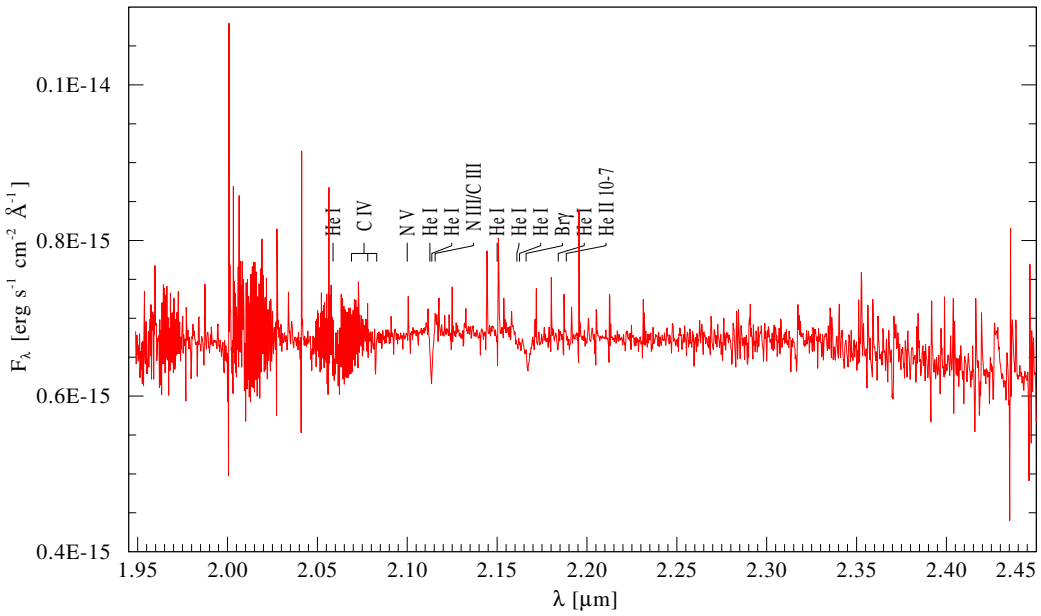

Figure 2.5: Flux-calibrated K-band spectrum of an O star (LHO 55) with line identifications as used for spectral classification.

were used to distinguish supergiants from giants by comparison with template spectra. Some spectral peculiarities of the classification are listed in Table 2.2. In uncertain cases, e.g. noisy spectra or blends with telluric OH lines, the classification is followed by ":" in Table B.1. An example of an O-star spectrum is shown in Fig. 2.5.

Table 2.2: Nomenclature of spectral peculiarities

Sign	Description
:	uncertain classification
e	emission lines
eq	emission lines with P Cygni profile
f	emission lines of N III and He II
p	unspecified peculiarities
d	dust emission assumed from a continuum rising with wavelength (IR excess)

WR stars To classify the Wolf-Rayet stars in the sample, the criteria from Crowther et al. (2006) have been used. For WC stars the line equivalent widths were measured to determine the ratio C IV/C III ($\lambda\,2.079\,\mu$m/$\lambda\,2.108\,\mu$m). The spectral type WC9 was assigned to stars with a ratio below one, WC8 for a ratio between one and four. All WC stars are of late spectral types WC8 and WC9, and interestingly all WC9 stars show a continuum that is increasing with wavelength. This excess is considered to emerge from hot circumstellar dust and the spectral classification is marked with "d" in Table B.1. The WC8 stars, on the other hand, do not display such dust emission. For the WN stars the ratio He II/Br γ ($\lambda\,2.189\,\mu$m/$\lambda\,2.166\,\mu$m)

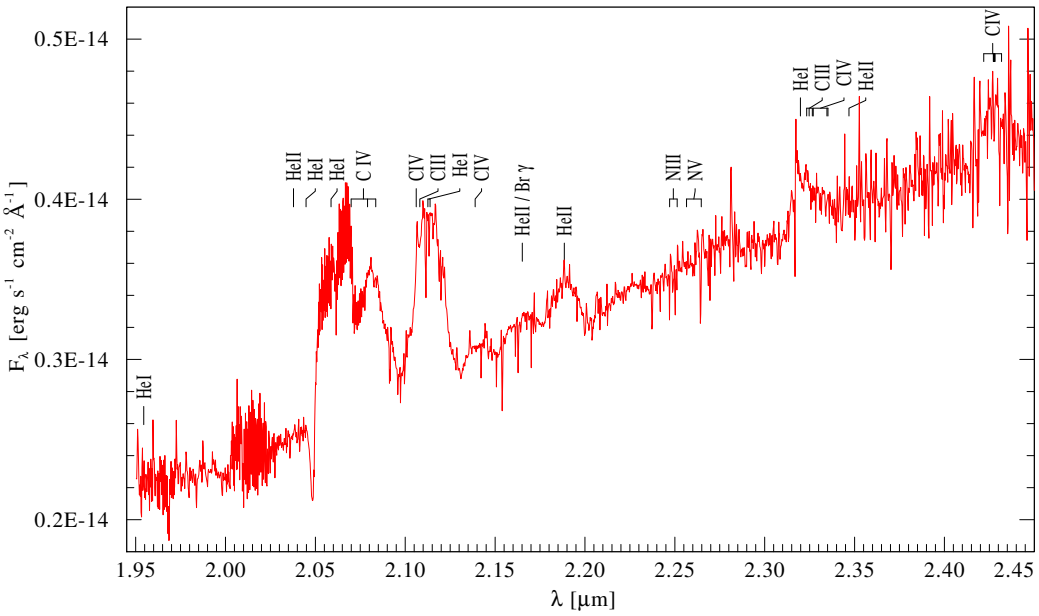

Figure 2.6: Flux-calibrated K-band spectrum of the newly discovered WR star LHO 76 with line identifications. Note the rising continuum towards longer wavelengths, indicative of hot dust. Accordingly, the spectral type is WC9d.

was determined to classify them. Since all stars show a ratio < 0.1, they all are of subtype WN9. Thus the catalog sample contains eleven WR stars, four WN9 stars, and seven WC stars which were previously known. Additionally, two new WR stars are found: LHO 76 and 79.

The star LHO 76 is claimed to be a newly discovered WR star in the Quintuplet cluster, because it could not be identified with any known source. Its spectral type is WC9d, see Fig. 2.6. Naming the star is quite tricky and has to follow the generally accepted naming scheme of van der Hucht (2001). Thus this star would have to be called WR 102db, belonging to the subgroup of WR 102d-stars. However, this group comprises already four stars and would have to be renamed with the new member:

- WR 102da (old) = WR 102da (new)
- LHO 76 → WR 102db (new)
- WR 102db (old) → WR 102dc (new)
- WR 102dc (old) → WR 102dd (new)
- WR 102dd (old) → WR 102de (new)

Renaming an existing/established group of stars is always ambiguous and will only prove useful when the new names are accepted and applied by the community. However, it is not unusual to rename WR stars especially in the Galactic-center region; hence, it might be considered appropriate for clusters with such a limited number of stars as the Quintuplet.

The second new WR star, LHO 79, is identified with a star listed by Figer et al. (1999a) as source qF 250. Considering its spectral appearance, a re-classification from type $<$ B0 I to WC9d is necessary, see also Fig. 2.7. Thus the total number of WR stars in the Quintuplet cluster is 13 in the LHO catalog.

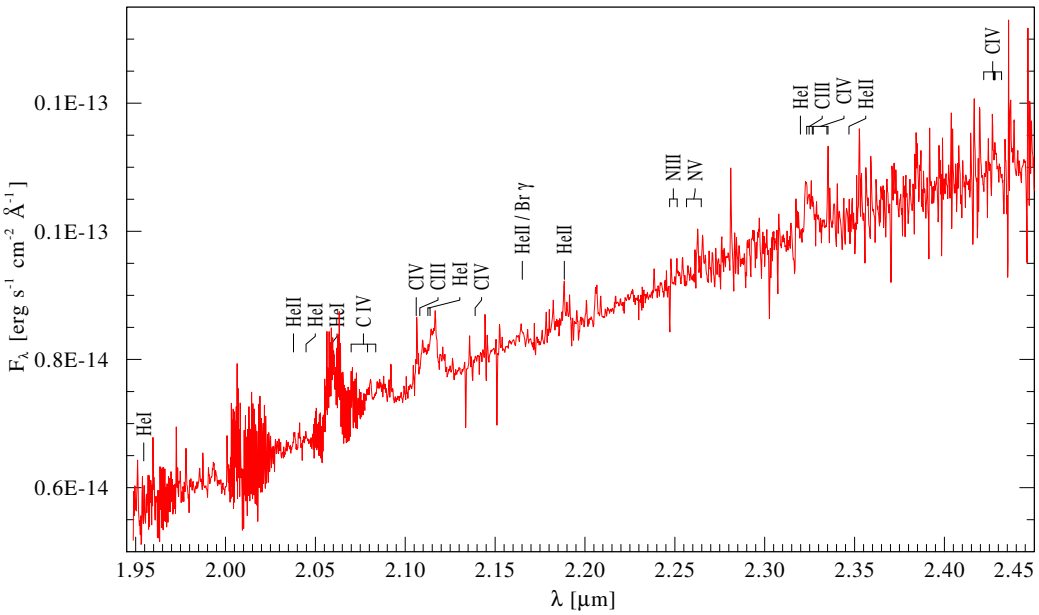

Figure 2.7: Flux-calibrated K-band spectrum of Q 6 (LHO 79) showing broad emission line features superimposed on a warm-dust continuum as evidenced by a rising continuum. The spectral class is WC9d, revising the classification by (Figer et al. 1999a) who gave "< B0 I" for the alias-named object qF 250.

Late-type stars The spectra of late-type stars are a special challenge for classification. Usually these stars are much fainter than the brighter O stars and WR stars, and the spectra might look rather noisy which makes it hard to identify absorption lines for classification. Fortunately, one very dominating feature can be found in the K-band spectra which is the absorption bands of the CO molecule (first overtone bands), see Fig. 2.4. Both isotopic lines, ^{12}CO and ^{13}CO, can be found in absorption. The isotope ^{13}C is considered to be an indicator of late-type (super-) giant stars (Goorvitch 1994; Wallace & Hinkle 1997; Kleinmann & Hall 1986). As shown by Kraus (2009) the ratio ^{12}C/^{13}C decreases with stellar age, see Fig. 2.8. The equivalent width (EW) of the ^{12}CO (2-0) band-head was measured to determine the effective temperature of the star following

$$T_{\rm eff} = 4895 - 62 \times {\rm EW(CO)} \tag{2.1}$$

and its spectral subtype

$$G = 0.56 \times {\rm EW(CO)} - 3.0\,, \tag{2.2}$$

as described by González-Fernández et al. (2008). From the integer number G in the range of 0 to 13, the subtypes can be derived, e.g. $G = 6$ gives M0. Both relations are only applicable for (super-) giant stars, an assumption that seems justified by the presence of the ^{13}CO band absorption and by the derived synthetic magnitudes, see below. Seven stars showed a very small measured EW, which resulted in negative G values. Therefore these stars are classified as "K0?" in Table B.1 since they might be of an earlier spectral subtype.

2.2.3 Photometry

The flux-calibrated spectra can be used to derive synthetic K-band magnitudes . The 2MASS $K_{\rm s}$ (K "short") filter of was chosen for comparability. It is centered at 2.159 μm with the

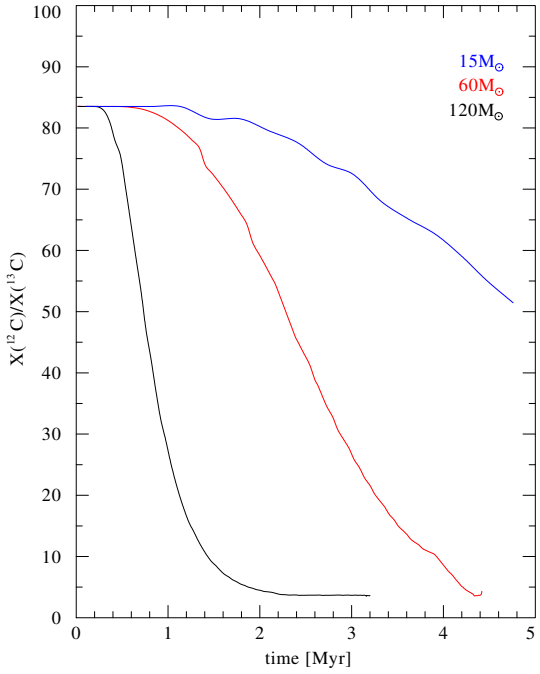

Figure 2.8: Decreasing carbon isotope ratio $^{12}C/^{13}C$ over stellar evolution from Geneva models with rotation (Meynet & Maeder 2003b); tracks are calculated with 300 km/s initial rotation for 15 $M_\odot$ (blue), 60 $M_\odot$ (red), and 120 $M_\odot$ (black).

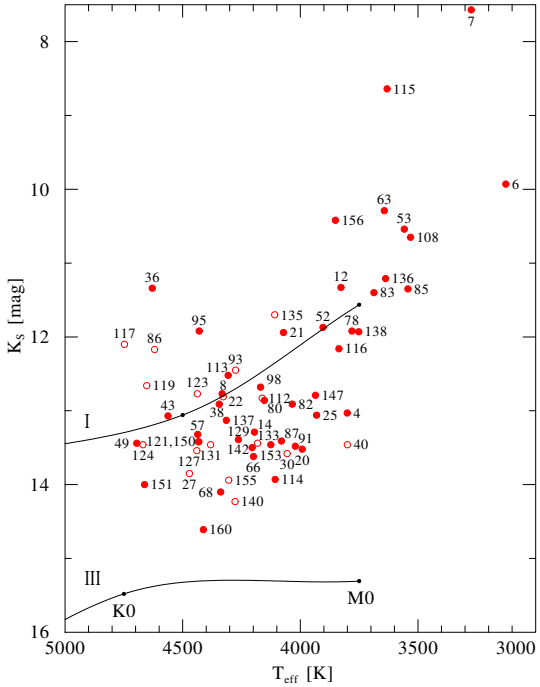

Figure 2.9: K_s magnitude vs. $T_{\rm eff}$ for the late-type stars of the sample, identified by their LHO number. Open circles denote stars for which the radial velocity is uncertain or indicates that they are foreground objects. The solid lines interpolate Kurucz models for K0, and M0 stars of luminosity classes I and III.

transmission curve shown in Fig. 2.10. The area-normalized transmission curve is multiplied with the flux-calibrated spectrum and integrated over the spectral range to obtain a mean flux per wavelength f_λ. Magnitudes are derived following

$$K_{\rm s} = -2.5 \times \log\left(\frac{\lambda_{\rm c}^2}{c} f_\lambda\right) - C_{\rm zp} \tag{2.3}$$

with the constant for the photometric zero-point $C_{\rm zp} = 50.440$ mag measured by Cohen et al. (2003) , and the conversion factor $\lambda_{\rm c}^2/c$ to transform f_λ into f_ν (flux per frequency).

About 22 LHO stars are in common with the sample of Glass et al. (1999) as listed in Table 2.3. The derived synthetic magnitudes are compared with their values and a mean difference of 0.2 mag is found. This is considered to be the error to the synthetic $K_{\rm s}$, see also Fig. 2.11. Magnitudes for all catalog objects are listed in Table B.1. To derive an estimate for the photometric completeness of the catalog, the number of stars per magnitude is shown in Fig. 2.12 as a histogram. The logarithmic distribution (red circles) can be fitted by a linear slope resulting in a power law up to $K_{\rm s} = 13$ mag. This value is therefore considered the photometric completeness limit.

From the spectral classification of the late-type stars the luminosity class still remains to determined. In Fig. 2.9, the derived $K_{\rm s}$ magnitudes are plotted versus the effective temperatures of the stars. To evaluate the stars' location in the Hertzsprung-Russell diagram

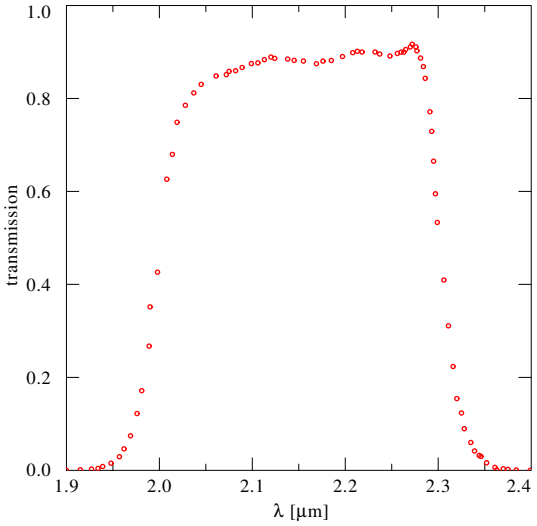

Figure 2.10: Transmission curve of the 2MASS K_s filter. For the synthetic-aperture photometry the area-normalized curve is applied to derive K_s-magnitudes.

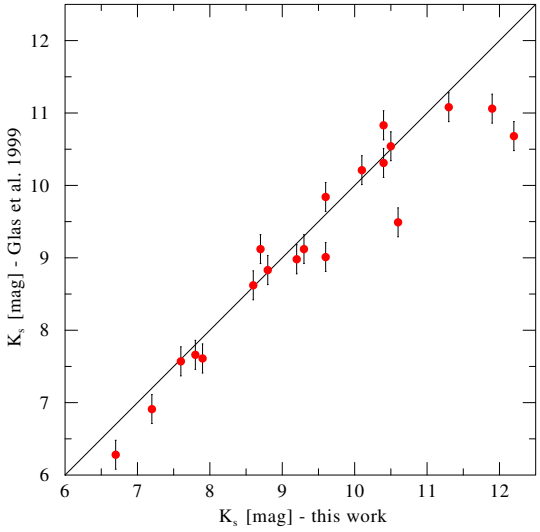

Figure 2.11: Verification of the applied synthetic-aperture photometry method. Comparison of the obtained K_s-magnitudes, see Table 2.3.

they are compared to Kurucz models (Kurucz 1993) for spectral subtypes G0, K0, and M0 of the luminosity classes I and III. Typical masses of $1.1\,M_\odot$ (G type), $0.8\,M_\odot$ (K type), and $0.4\,M_\odot$ (M type) are assumed and the model fluxes are scaled to the adopted cluster distance of 8 kpc (Reid 1993). An average interstellar extinction of $A_K = 3.28$ mag (Figer et al. 1999a) is applied to diminish the model fluxes and to calculate their K_s magnitudes. Then the model magnitudes are connected by linear fits in Fig. 2.9 to represent the approximate regions of the corresponding luminosity class. The catalog stars scatter around the upper line for supergiants with some stars being slightly less bright; to these the luminosity class II was assigned.

2.2.4 Cluster membership

Establishing a new catalog of stars in the Quintuplet cluster is rendered difficult by the line-of-sight effect, which might lead to a star being considered a cluster member although it is spatially not related to the cluster but just happens to lie in front or behind the cluster. Therefore, radial velocities (RVs) of all stars in the catalog are determined by comparing the observed wavelength of a prominent spectral feature to its theoretical one. The difference in wavelength is a measure for the radial velocity $RV = (\Delta\lambda/\lambda) \cdot c$. Since stars that belong to the Quintuplet cluster are spatially related, they show similar RVs, while stars that are no cluster members should show a different RV.

However, this is an incomplete measure of the position of an object along the line-of-sight. Since the radial velocity is just one component of the proper motion of a star, this method can for example be affected by RV variations due to binary companions and it is insensitive to line-of-sight objects that have by chance similar RVs as the cluster.

For the early-type stars in this sample the wavelength of the Br γ was measured and the ^{12}CO (2-0) bandhead for late-type stars, and compared to the respective laboratory wavelength. The derived heliocentric RVs are listed in Table B.1. The spectral resolution of the

Table 2.3: Comparison of synthetic K_s magnitudes with known photometry for individual stars.

LHO	t. w.	Glass et al. (1999)	
No.	K_s [mag]	K_s[mag]	ID
7	7.6	7.57	Q 7
12	11.3	11.08	D 3605
19	7.2	6.91	Q 3
39	12.2	10.68	D 3606
42	6.7	6.28	Q 2
47	10.4	10.31	Q 11
52	11.9	11.06	D 334
67	9.6	9.01	Q 8
71	8.8	8.83	Q 10
74	10.9	10.95	D 309
75	7.9	7.61	Q 1
77	9.6	9.84	Q 12
79	9.3	9.12	Q 6
84	7.8	7.66	Q 4
99	10.1	10.21	D 215
102	9.2	8.98	Q 9
108	10.7	10.65	D 322
110	10.6	9.49	Q 15
115	8.6	8.62	Q 5
143	10.5	10.54	D 271
146	8.7	9.12	Q 14
156	10.4	10.83	D 307

observations is not very high, $R = \lambda/\Delta\lambda \approx 4000$ which leaves a rather high error to the determined radial velocities of ± 37 km/s. For noisy spectra the results are more uncertain (marked with ":" in Table B.1).

Under the assumption that the 15 bright Quintuplet stars from the QPM list by Glass et al. (1990, see also Table 2.3) are real cluster members, a mean radial velocity $\overline{RV}_{\rm QPM} = 113 \pm 17$ km/s is derived. This assumption seems reasonable given the K_s magnitudes, although the magnitude alone is no criterion for cluster membership. Comparable RV values of 127, 133, and 135 km/s were found by measuring line-of-sight velocities from the Br γ line by Figer (1995) for the Pistol star, Q 8, and Q 15, respectively. From this the average cluster velocity was estimated to 130 km/s by Figer et al. (1999a). Of course, not all stars in a cluster have the same RV due to initial variations at star formation and cluster evolution. A measure for the spread of RVs is the internal cluster-velocity dispersion. Following Kroupa (2002), a virialized cluster shows a velocity dispersion

$$\sigma_{\rm cluster} = \sqrt{\frac{G \cdot M_{\rm stars}}{\epsilon \cdot R}}\,, \tag{2.4}$$

with $M_{\rm stars}$ the mass of stars in the cluster, ϵ the star-formation efficiency, G gravitational constant and R cluster radius, i.e. usually the half-light radius.

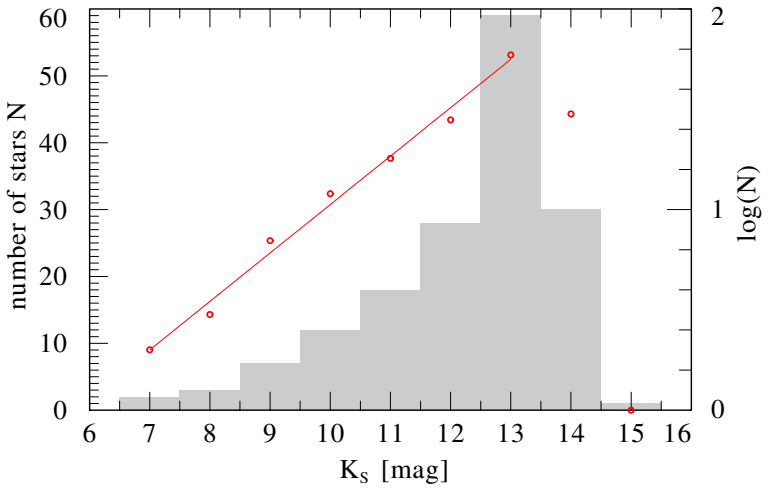

Figure 2.12: Histogram of the synthetic K-band magnitudes with a bin size of 1 mag (gray areas). The linear fit to the logarithmic distribution (red line and circles) indicates a photometric completeness of the catalog up to $K_s = 13$ mag.

The Quintuplet cluster is a young cluster of about 4 million years of age that is very likely not yet virialized. However, to assume a virialized cluster is the only way to derive the first cluster dispersion for the Quintuplet cluster at all, and to be able to evaluate the derived RVs in terms of a cluster membership. Thus equation (2.4) is applied with a star formation efficiency ϵ between 20 and 40 % (Kroupa 2002), a stellar mass in the range of $10^{3.8-4.2}\,M_\odot$ (Figer et al. 1999a), and a cluster radius of 1 pc (Figer et al. 1999a). A cluster dispersion of $\sigma_{\rm cluster} = 8 - 18$ km/s is obtained, well in agreement with the determined error of the QPM stars ($\sigma_{\rm QPM} = 17$ km/s). By this means, the 3σ interval around $\overline{RV}_{\rm QPM}$ can be considered a criterion for cluster membership, see Fig. 2.13. A few stars in the sample show lower RVs; they are mainly of late spectral type and considered as foreground objects (marked "f" in Table B.1).

2.3 Summary

The presented K-band spectral catalog of 160 stellar sources in the central region of the Quintuplet cluster is the first catalog based on integral field spectra in the range of 1.95 to 2.45 μm, obtained with the ESO SINFONI-SPIFFI instrument. It comprises flux-calibrated spectra of 98 early-type (OB and WR) stars and 62 late-type (K to M) stars with a spectral resolution of $R \approx 4000$; see Table 2.4 for details.

The 160 sources are listed in Appendix B Table B.1 with their LHO-catalog number (column 1), the coordinates of each source (columns 2 and 3), and the synthetic K_s magnitude (column 4). Spectral type and radial velocities are given in column 5 and 6. Uncertain classification or RV values are indicated by ":", while foreground objects are indicated by "f". Additionally, a complete list of aliases and cross-identification with previous catalogs and surveys is given in column 7.
About 100 objects in the list are cataloged for the first time and two new WR stars are found in the sample.

Appendix B shows the flux-calibrated spectra of all catalog stars rebinned to 4 Å spectral resolution. Unfortunately, some of the spectra are heavily contaminated with OH emission

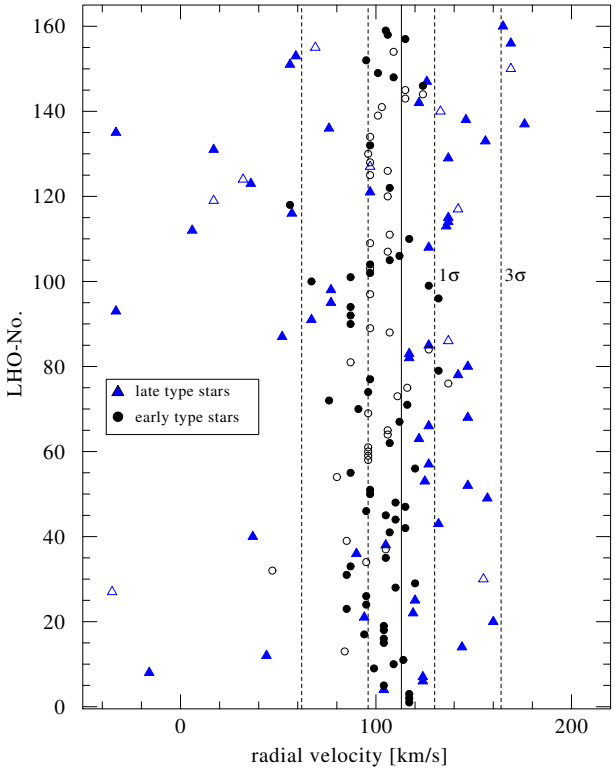

Figure 2.13: RVs of the catalog stars. Circles denote early-type stars, triangles denote late-type stars. Open symbols are for uncertain values due to noisy spectra. The solid vertical line indicates $\overline{RV}_{\mathrm{QPM}} = 113\,\mathrm{km/s}$, while the dashed lines indicate intervals of $\pm\sigma$ and $\pm 3\sigma$ ($\pm 17\,\mathrm{km/s}$ and $\pm 51\,\mathrm{km/s}$), respectively.

Table 2.4: Distribution of spectral-type in the LHO catalog

Spectral Type	No. of stars	Luminosity class	
		II/III	I
WN	4	-	-
WC	9	-	-
WR total	*13*	-	-
O	60	12	48
B	25	7	18
OB total	*85*	*19*	*66*
K	43	23	20
M	19	5	14
KM total	*62*	*28*	*34*
total	160	-	-

lines that limit the visibility of stellar spectral features.

Chapter 3

The Models

In this chapter the basic parameters of stars and stellar atmospheres that are fundamental for the spectral analysis are established. The radiative transfer in stellar atmospheres is described in detail in Mihalas & Mihalas (1984) and the theoretical model of a line-driven stellar wind can be found in Castor et al. (1975), we restrict this part to a brief overview. The Potsdam Wolf-Rayet models (PoWR) for expanding atmospheres are introduced in the second part of this chapter, with respect to the specific input that was used in this work to analyze the obtained WR spectra. Further details about the PoWR code can be found in Gräfener (1999); Barniske (2008) and Gräfener et al. (2002).

3.1 Introduction

The intensity $I_\nu(\vec{x}, t, \vec{n}, \nu)$ is the fundamental parameter to describe an electro-magnetic field as the amount of energy emerging at a specific position per time interval, per frequency interval, per solid angle and per unit area. Usually, stars are unresolved objects that appear as point sources for which the emergent flux F_ν^+ is the fundamental observable

$$H_\nu = \pi\, F_\nu^+ \quad = \quad \int_0^{2\pi} \int_0^{\pi/2} I_\nu \cos\theta\, \sin\theta\, \mathrm{d}\theta\, \mathrm{d}\phi\,. \tag{3.1}$$

By definition this is the first moment of the radiation field, with the general moments defined as follows ($\mu = \cos\theta$)

$$[J_\nu, H_\nu, K_\nu, N_\nu] = \frac{1}{2} \int_{-1}^{1} I_\nu(\mu)\, [1, \mu, \mu^2, \mu^3] \mathrm{d}\mu\,. \tag{3.2}$$

On the way to the observer the intensity is subject to the interplay with an medium in which the electro-magnetic wave is propagating. The two basic parameters that describe the radiative characteristics of the medium are the extinction or opacity κ_ν and the emissivity η_ν.

The intensity emitted can thus be diminished or increased along the geometrical path $\mathrm{d}s$ following the radiative transfer equation

$$\frac{\mathrm{d}I_\nu}{\mathrm{d}s} = \eta_\nu - \kappa_\nu I_\nu\,. \tag{3.3}$$

The path integral of the opacity κ_ν along the line of sight $\mathrm{d}s$ gives a dimensionless quantity called optical depth τ_ν. We will use the relation $\mathrm{d}\tau = -\kappa \mathrm{d}s$ with $\tau(s = s_{\max}) = 0$. The ratio of all emissivities over all opacities defines the source function

$$S_\nu := \frac{\sum \eta_\nu}{\sum \kappa_\nu} \tag{3.4}$$

by which means equation (3.3) is transformed to

$$\frac{\mathrm{d}I_\nu}{\mathrm{d}\tau_\nu} = S_\nu - I_\nu\,. \tag{3.5}$$

Formal solution With a given source function, i.e. the opacity and emissivity of the medium are known, the formal solution of the radiative transfer equation follows as

$$I_\nu^+(\tau_\nu) = I_\nu^+(\tau_{\max}) e^{-(\tau_{\max} - \tau)} + \int_{\tau_\nu}^{\tau_{\max}} S_\nu(t_\nu) e^{-(t_\nu - \tau_\nu)}\, \mathrm{d}t_\nu \tag{3.6}$$

3.2 Model atmospheres

Stellar atmospheres of WR stars are anisotropic; the strong radiation field and the low particle densities do not longer support an LTE regime, but lead to a non-LTE scenario . Further on, the expansion of the atmosphere renders it necessary to take Doppler shifts for all frequency-dependent parameters into account.

Model atmospheres allow the evaluation of this scheme by solving two sets of equations consistently, the radiative transfer equation and rate equations for the population numbers. These population numbers depend on the local radiation field and enter into the emissivities and opacities that define the source function for the radiative transfer.

3.2.1 Rate equations

In the stationary case ($\dot{\vec{n}} = 0$) the gains and losses of the population numbers of each level are balancing each other (statistical equilibrium)

$$\sum_{\mathrm{m}} n_{\mathrm{m}} P_{\mathrm{mn}} \quad = \quad n_{\mathrm{n}} \sum_{\mathrm{m}} P_{\mathrm{nm}} \,. \tag{3.7}$$

The transitions between energy levels are possible via collisions and by radiative processes, described by the respective transition coefficients C_{nm} and R_{nm}. Thus

$$n_{\mathrm{n}} \sum_{\mathrm{m}} (R_{\mathrm{nm}} + C_{\mathrm{nm}}) \quad = \quad \sum_{\mathrm{m}} n_{\mathrm{m}} (R_{\mathrm{mn}} + C_{\mathrm{mn}}) \,. \tag{3.8}$$

Collisionally excited transitions Concerning collisional processes, there are four characteristic transition channels. Ions and atoms can enter into or leave energetically exited states by collisions. Further on, the ionization of a neutral atom or recombination to a neutral atom are possible. The temperatures in Wolf-Rayet atmospheres usually are very high, i.e. most atomic species are already ionized. The important number density of collisional partners is therefore the one of the free electrons in the atmosphere. The electrons are considered to be in LTE, their velocity distribution follows the Maxwell distribution $f(v_{\mathrm{e}})$. The cross-section for a transition between two atomic or ionic levels is σ_{mn}, the electron density n_{e} and it follows

$$C_{\mathrm{mn}} = n_{\mathrm{e}} \int_{v_0}^{\infty} \sigma_{\mathrm{mn}}(v)\, f(v_{\mathrm{e}})\, \mathrm{d}v \tag{3.9}$$

with a threshold velocity v_0 referring to the minimum energy needed for the considered transition.

Radiatively excited transitions For radiatively exited transitions it can be distinguished between spontaneous and radiation-induced ones, described by the Einstein coefficients

$$A_{\mathrm{mn}} = \frac{2h\nu^3}{c^2} \qquad\qquad B_{\mathrm{mn}} = \frac{g_{\mathrm{n}}}{g_{\mathrm{m}}} B_{\mathrm{nm}} \,, \tag{3.10}$$

respectively. The radiative transition probabilities follow as

$$R_{\mathrm{mn}} = A_{\mathrm{mn}} + B_{\mathrm{mn}} \int J_\nu \phi(\nu)\, \mathrm{d}\nu = A_{\mathrm{mn}} + B_{\mathrm{mn}} \bar{J} \tag{3.11}$$

with the radiation-induced transition depending on the radiation field.
Radiatively excited transitions can be distinguished further into free-free transitions, involving

an ion and a free electron, bound-free transitions representing photo-ionization and recombination processes, and bound-bound transitions with an electron changing energy levels within an atom or ion.

The challenging part about the different transition processes is, that the population numbers and the radiation field have to be determined simultaneously. However, it is more practical to solve for the population numbers and derive the radiation field later on. Iterated over several steps this should converge to a solution for every point in the atmosphere.

3.2.2 Radiative transfer

As can be seen from equation (3.11) the statistical equations for the population numbers depend on the angle-averaged mean intensity J which is integrated over the profile function $\phi(\nu)$. This intensity has to be evaluated in the co-moving frame of the corresponding volume element of the atmosphere. Due to the expansion all elements are receding from each other which introduces frequency shifts in the propagating photons. For an atmospheric element moving with the velocity $v(r)$ the comoving frequency can be written as

$$\nu(r,\mu) = \nu_0 \left(1 + \mu\frac{v(r)}{c}\right) \approx \nu_0 + \mu\frac{v(r)}{c}\cdot\nu_\mathrm{c} \tag{3.12}$$

with ν_0 the frequency in the observers frame and c the speed of light. The approximation holds for the line center ν_c.

Thus, the radiation seen by the particles in a volume element, the frequency-dependent emissivity and opacity, have to be considered under the aspect of Doppler shift . The intensity I_ν becomes $I_\nu^\mathrm{CMF}(\nu_0)$ in the co-moving frame (CMF) with

$$\frac{\mathrm{d}I_\nu}{\mathrm{d}s} \rightarrow \frac{\mathrm{d}I_\nu^\mathrm{CMF}}{\mathrm{d}s} + \frac{\partial I_\nu^\mathrm{CMF}}{\partial\nu_0}\frac{\mathrm{d}\nu_0}{\mathrm{d}s}\,. \tag{3.13}$$

The superscript is left in the following equations.

For the extended atmosphere of a WR star spherical symmetry is assumed and spherical coordinates are more appropriate $s \rightarrow (r,\mu)$. The coordinate transformation follows as

$$\frac{\mathrm{d}r}{\mathrm{d}s} = \mu \qquad \frac{\mathrm{d}\mu}{\mathrm{d}s} = \frac{1-\mu^2}{r} \qquad \frac{\mathrm{d}\nu_0}{\mathrm{d}s} = -\frac{\nu_0}{c}\left(\mu\frac{\mathrm{d}v}{\mathrm{d}r}\frac{\mathrm{d}r}{\mathrm{d}s} + v\frac{\mathrm{d}\mu}{\mathrm{d}s}\right) = -\frac{\nu_0}{c}\left(\mu^2\frac{\mathrm{d}v}{\mathrm{d}r} + v\frac{1-\mu^2}{r}\right) \tag{3.14}$$

and the radiative transfer equation in the co-moving frame is obtained

$$\frac{\partial I_\nu}{\partial r}\mu + \frac{\partial I_\nu}{\partial\mu}\frac{1-\mu^2}{r} + \frac{\nu_0}{c}\left(-\mu^2\frac{\mathrm{d}v}{\mathrm{d}r} - v\frac{1-\mu^2}{r}\right)\frac{\partial I_\nu}{\partial\nu_0} = \eta_\nu - \kappa_\nu I_\nu\,. \tag{3.15}$$

An dimensionless frequency x and velocity $V(r)$ in Doppler units are introduced to transform the transfer equation to

$$\frac{\partial I_\nu}{\partial r}\mu + \frac{\partial I_\nu}{\partial\mu}\frac{1-\mu^2}{r} + \frac{\nu_0}{c}\left(-\mu^2\frac{\mathrm{d}V(r)}{\mathrm{d}r} - (1-\mu^2)\frac{V(r)}{r}\right)\frac{\partial I_\nu}{\partial x} = \eta_\nu - \kappa_\nu I_\nu\,. \tag{3.16}$$

3.2.3 Solution

Equation (3.15) can be solved for all frequencies and spatial points in the model atmosphere to obtain the mean intensity J that is needed for the rate equations. Regular models contain up to 200 000 frequency points and ca. 3000 spatial points which makes one iteration rather

expensive. However, it is more efficient to solve the moment equations of the transfer equation as proposed by Auer & Mihalas (1970) for static and Mihalas et al. (1976) for expanding atmospheres. The moment equations are obtained as angle integral $\int \mathrm{d}\mu$ with the same definition as the moments of the radiation field, see equation (3.2) for comparison. The zeroth and first moment are

$$-\frac{\partial H_\nu}{\partial r} + \left(\frac{\mathrm{d}V(r)}{\mathrm{d}r} - \frac{V(r)}{r}\right)\frac{\partial K_\nu}{\partial x} + \frac{V(r)}{r}\frac{\partial J_\nu}{\partial x} = (J_\nu(r) - S_\nu(r))\,\kappa_\nu(x,r) \tag{3.17}$$

$$\frac{\partial(qK_\nu)}{-q\partial r} + \left(\frac{\mathrm{d}V(r)}{\mathrm{d}r} - \frac{V(r)}{r}\right)\frac{\partial N_\nu}{\partial x} + \frac{V(r)}{r}\frac{\partial H_\nu}{\partial x} = \kappa_\nu H_\nu\,. \tag{3.18}$$

The factor q is the sphericity factor and the closure relations for the moment equations are

$$f = \frac{K}{J} \qquad g = \frac{N}{H}\,, \tag{3.19}$$

defining the Eddington factors .

The Eddington factors are obtained from equation (3.16) in a ray-by-ray scheme (short characteristics integration). This full calculation of the radiative transfer equation is not performed at each iteration. Since the Eddington factors are well-behaved in iterations (Mihalas & Mihalas 1984), they can be kept constant for those iterations solving the moment equations, and need to be updated only from time to time. With the given Eddington factors, the moment equations provide a system of two partial differential equations for J and H which is solved in a differencing scheme. The obtained J is then applied for the rate equations to calculate the population numbers.

3.2.4 Boundary conditions

To solve the radiative transfer equation for an expanding atmosphere, boundary conditions need to be defined. A first requirement was already introduced in the stationarity of the atmosphere which resulted in the statistical equilibrium for the population numbers (Sect. 3.2.1). Further boundary conditions are introduced here:

Radiative equilibrium If a volume element of the atmosphere is emitting the same amount of energy that it had been absorbing, the element will neither be heated nor cooled. This aspect can be expressed with an equation of continuity for radiation

$$\int_0^\infty (\eta_\nu - \kappa_\nu J_\nu)\mathrm{d}\nu = 0\,. \tag{3.20}$$

For a static, non-expanding atmosphere the radiative flux is constant. However, in an expanding atmosphere it has to be considered that the photons transfer momentum to the matter. Thus, the luminosity is a sum of a radiative component and a mechanical component of the energy; for an expanding atmosphere only the total energy flux is constant.

Diffusion approximation The inner boundary has to be chosen such that the emergent intensity (I_ν^+) into the atmosphere can be described by the diffusion approximation . In the stellar interior at small radii and large optical depths, a thermalized radiation field is assumed – the source function is given by the Planck function. The intensity emerging into the atmosphere from the hydrostatic core can thus be adjusted by the temperature at a specific radius.

Back-scattering The outer boundary of the stellar atmosphere should be set at a large radius, which either allows to neglect back-scattering effects ($I_\nu^- = 0$) into the atmosphere or to make simplifying assumptions. For example, it usually is assumed that the source function will decay as the density with r^{-2}. Different methods to obtain I_ν^- are, for example, specifically prescribed source-function values for large stellar radii, or the extrapolation to the outermost boundary point.

3.3 Potsdam Wolf-Rayet models (PoWR)

The code for the PoWR models is grown over decades, with new implementations and improvements, as well as the basic details described in various papers, e.g. Schmutz et al. (1989); Hamann et al. (1995); Hamann & Koesterke (1998); Gräfener et al. (2002); Hamann & Gräfener (2004). To solve the radiative transfer for an expanding atmosphere, the velocity field $v(r)$ and the density $\rho(r)$ are prescribed. Although first models exist that solve the radiative transfer hydrodynamically self-consistent (Gräfener & Hamann 2003; Gräfener & Hamann 2005), they were not used in this work.

3.3.1 Overview

Basically, a stationary, spherically symmetric, homogeneous stellar atmosphere is assumed. The hydrodynamic equation of motion follows as

$$\rho v \frac{\mathrm{d}v}{\mathrm{d}r} = -\frac{\mathrm{d}P}{\mathrm{d}r} - \frac{GM}{r^2}\rho \tag{3.21}$$

with $\rho\, v$ the mass flow per cm^2 per second, $\mathrm{d}v/\mathrm{d}r$ the gradient of the radial velocity component, $\mathrm{d}P/\mathrm{d}r$ the pressure gradient, and the last term describing gravitation. In this form the pressure gradient absorbs the components of the thermal gas pressure, the continuum-radiation pressure caused mainly by Thomson scattering, and the line-radiation pressure.
For each radial shell of the area $4\pi r^2$ the mass flow has to be constant, resulting in the equation of continuity (mass conservation)

$$4\pi r^2 \rho v = \text{constant}\,. \tag{3.22}$$

In contrast to a hydrodynamically self-consistent model, the density $\rho(r)$ and velocity $v(r)$ are prescribed for each radius point in the atmosphere. Therefore, the WR star is divided in two parts, a hydrostatic core and the expanding atmosphere. The hydrostatic core is characterized by a hydrostatic density stratification with a subsonic radial velocity component. For the atmosphere a supersonic velocity is specified by a beta-law

$$v(r) = v_\infty \left(1 - \frac{R_*}{r}\right)^\beta \tag{3.23}$$

with v_∞ the terminal wind velocity and the exponent β as free parameters. For all calculated models we assumed $\beta = 1$ while the terminal velocity v_∞ [1] was adjusted individually.
The mass-loss rate follows as

$$\frac{\mathrm{d}M}{\mathrm{d}t} = \dot{M} = 4\pi r^2 \rho(r) v(r)\,. \tag{3.24}$$

To evaluate the stellar luminosity, it has to be taken into account that no stellar surface is given for an expanding atmosphere. Hence, a special radius is defined as the inner boundary such that the wind-emitting region above will be included in a sphere which is then used to derive the luminosity. This radius is defined by the Rosseland opacity, an approximation to overcome the frequency dependence of the opacity, as in the case of a gray atmosphere in LTE,

$$\frac{1}{\kappa_\mathrm{R}} = \left[\int_0^\infty \frac{\mathrm{d}B_\nu(T)}{\mathrm{d}T}\mathrm{d}\nu\right]^{-1} \int_0^\infty \frac{1}{\kappa_\nu}\frac{\mathrm{d}B_\nu(T)}{\mathrm{d}T}\mathrm{d}\nu \tag{3.25}$$

[1] The terminal velocity can also be measured directly, for example from the blue absorption component of a P Cygni resonance line.

which then leads to a Rosseland optical depth $\mathrm{d}\tau_\mathrm{R} = \kappa_\mathrm{R}\,\mathrm{d}r$. For the applied models

$$R_* := R(\tau_\mathrm{R} = 20)\,, \tag{3.26}$$

sets the inner boundary Hamann et al. (1995). Together with the assumption that the velocity $v(r = R_*)$ is subsonic, this radius defines the size of the hydrostatic stellar core. In the models the stellar luminosity is set constant to $\log L/L_\odot = 5.3$ and adjust the stellar temperature. From the Stefan-Boltzmann law the stellar radius (in solar units) is derived immediately,

$$\left(\frac{R_*}{R_\odot}\right)^2 = \frac{L}{L_\odot}\left(\frac{T_\odot}{T_*}\right)^4\,, \tag{3.27}$$

where T_* represents the effective temperature of the star referring to the stellar radius R_*. A specific radius defined in the models is the transformed radius

$$R_\mathrm{t} = R_*\left[\frac{v_\infty}{2500\mathrm{km\,s^{-1}}}\Big/\frac{\sqrt{D}\dot{M}}{10^{-4}M_\odot\mathrm{yr}^{-1}}\right]^{2/3}\,, \tag{3.28}$$

including the stellar radius R_*, the clumping factor D, the mass-loss rate $\dot{M}$ and the terminal wind velocity v_∞. However, it rather resembles the emission measure of the wind scaled to the stellar surface than a real radius and thus has impact on the equivalent width of of the emission lines. The transformed radius shows a scale-invariance, which allows the models to be parameterized by the stellar temperature T_* and the transformed radius R_t: for a fixed temperature and chemical abundance, the same equivalent width of an emission line can be reproduced with a different set of R_*, D, v_∞, and $\dot{M}$.

The general assumption of a homogeneous stellar atmosphere is questioned by observations of discrete absorption components in O-star spectra and discrete wind-emission elements in WR-star spectra (Prinja & Howarth 1988; Moffat et al. 1988). Moreover, the observed wings of emission lines caused by Thomson scattering of free electrons in the wind are weaker than predicted by the models. It can be assumed that the wind material is condensed into entities of enhanced density, i.e. "clumps", with the interclump medium assumed to be vacuum. A factor $D = \rho_\mathrm{clump}/\rho_\mathrm{smooth}$, i.e. the clumping factor, describes the density enhancement in the clumps. This factor can also be understood in terms of a volume-filling factor $f_\mathrm{V} = D^{-1}$; the same amount of material as in the smooth wind is now collected in a smaller volume. For Galactic WN stars, empirical clumping factors are in the range $D = 4$ to 10 (Hamann et al. 2006). There are observational indications that the clumping factor has a radial dependence $D(r)$ (Puls et al. 2006; Liermann & Hamann 2008). However, for all models in this work $D = 4$ is assumed.

Further line-broadening by micro-turbulence is accounted for with a Doppler velocity v_D. Thus the line profile function becomes

$$\phi(\nu - \nu_0) = \frac{1}{\sqrt{\pi}\Delta\nu_\mathrm{D}}e^{-\left(\frac{\nu-\nu_0}{\Delta\nu_\mathrm{D}}\right)^2} \quad \text{with} \quad \Delta\nu_\mathrm{D} = \nu_0\frac{v_\mathrm{D}}{c}\,. \tag{3.29}$$

A typical value of $v_\mathrm{D} = 100\,\mathrm{km/s}$ is applied for all models.

The Potsdam group has established two grids of models [2] for the analysis of WN stars which are parameterized by the stellar temperature T_* and R_t (see also Hamann et al. 2006). These grids comprise normalized model spectra from the ultraviolet to the infra-red spectral range, as well as model spectral energy distributions. However, for the analysis of the Quintuplet WN stars individual models were calculated by adjusting the input parameters of grid models.

[2] http://www.astro.physik.uni-potsdam.de/PoWR.html

3.3.2 Input to the code

CARDS – stellar parameters The CARDS file specifies the basic stellar parameters temperature, transformed radius, terminal velocity, and chemical abundances. A set of input lines ("-" denotes comment lines) may look as follows

```
--------------------  stellar parameters  ------------------------------
DENSCON = 4.
TEFF= 28184.
-RSTAR (SOLAR UNITS):  2.977
LOG L = 5.3
-MSTAR = 1.2
-LOG G= 4.9
-MDOT= -5.282                  (LOG OF SOLAR MASSES PER YEAR)
RTRANS = 1.40DEX
RMAX_IN_RSUN
VELPAR: VFINAL (KM/S)=  400. VMIN= 12.  BETA=1.0 RMAX=1000. XXXXXXX
xxxxxxxxxxxxxxxxxxxxx.......xxxxx......xxxxx....xxxxx......xxxxxxx
VDOP=100.
```

In some cases as with the velocity parameters (VELPAR) a fixed formatted input is expected, specifying the terminal velocity, a minimum velocity, the β-exponent to the velocity law and the maximum radius (in solar radii). The parameters TEFF, RSTAR and LOG L are connected via the Stefan-Boltzmann law in which case the parameter not specified (here RSTAR) is derived from the two others. The mass-loss rate (MDOT) is derived from the transformed radius, clumping factor, stellar radius, and terminal velocity following equation (3.28).
The chemical abundance of an element can be specified in either particle number fraction or mass fraction (set keyword "mass fraction"),

```
--------------------  abundances  -------------------------------------
xxxxxxxxxx----------xxxxxxxxxx
HYDROGEN:  0.10     (mass fraction)
NITROGEN:  0.015    (mass fraction)
CARBON:    1.E-4    (mass fraction)
-OXYGEN:     0.15    (mass fraction)
GENERIC:   1.4E-3    (mass fraction)
```

but any listed element needs to be specified in the DATOM file. Model atoms comprise hydrogen, helium, and CNO. The iron-group elements [3] are supplied as extra input (FEDAT file) and are accounted for in a "superlevel" approach enabling for blanketing by millions of lines (see Gräfener et al. 2002).
Further (optional) parameters in the CARDS file specify the start approximation, the radius grid for the calculations, and optional output such as the temperature stratification, or derived population numbers.

DATOM – atomic data To obtain a meaningful and realistic synthetic spectrum for the analysis of observed spectra, it is crucial to implement sufficient and appropriate atomic data . The spectral classification of WR stars is based on the prominent features in the UV

[3] scandium, titanium, vanadium, chromium, mangan, iron, cobalt, nickel

Table 3.1: Basic chemical abundances (mass fractions) applied for the models in this work.

	WN (grid)	WN (Asplund)
$X_{\rm N}$	1.5×10^{-2}	8.2×10^{-3}
$X_{\rm C}$	1.0×10^{-4}	1.4×10^{-4}
$X_{\rm Fe}$	1.4×10^{-3}	1.2×10^{-4}
$X_{\rm H}$	0.00 - 0.20	
$X_{\rm He}$	0.78 - 0.98	

and optical range since the stars have their radiative maximum in the UV. Therefore, the current version of the atomic data is trimmed to fit the UV and optical spectra of WR stars. However, the stars to be analyzed are located in the Galactic center and highly obscured in the UV and optical. Although the main spectral features for hydrogen and helium are already implemented up to the mid-IR range, the data are quite coarse for other atomic species. Some single IR lines for N III, N V, C III, and C IV have been added by various (former) group members. To overcome a part of this incompleteness, new atomic data were assembled.

Data retrieval As described in Section 3.2.1 the necessary information for each atomic species comprise rates for radiative and collisional transitions such as oscillator strengths, or Einstein coefficients and collisional coefficients. To implement extensions for further line transitions in the models, new atomic data were obtained from databases available to the community, e.g. `The Opacity Project` [4], `The Atomic Line List` [5], and the `NIST - Atomic Spectra Database` [6]. However, these datasets are not complete, especially when it comes to transitions between levels with high quantum numbers, highly ionized species, and ions with complex transitions.

The two major changes in the atomic data used in the models concern the elements helium and nitrogen. The existing atomic data for He II contained energy levels for the main quantum numbers $n = 1 \ldots 16$. Newly implemented extensions reach up to $n = 23$. The extension of helium and hydrogen atomic data for the near-IR and mid-IR were indepently and simultaneously prepared by two members of our group, A. Barniske and A. Liermann. Both data sets were checked in test models and found to result in improved infrared model spectra. The database is almost identical and therefore one "group version" was compiled and agreed on. While N V atomic data were already contained in the DATOM file the line transitions in the near-IR aimed at, required higher energy levels up to $n = 12$. These data are not available from the public archives and databanks. The used oscillator strengths and cross-sections were provided by Dr. Keith Butler [7] together with NIST level energies, which are available for the low-n levels. A completely new model ion N V was compiled to replace the former version.

Levels, lines, and continua The atomic data are implemented via energy levels, line transitions and continuum cards. Each energy level is labeled with a ten-digit string that

[4] The Opacity Project – http://cdsweb.u-strasbg.fr/topbase/op.html
[5] The Atomic Line List – http://www.pa.uky.edu/ peter/atomic/
[6] National Institute of Standards and Technology (NIST) – http://physics.nist.gov/PhysRefData/ASD/index.html
[7] Dr. Keith Butler, Ludwig-Maximilians-Unviversität München

should identify the atomic species, ionization state, and main quantum number. Possibly, the term or spin quantum number are included, or the last digits may indicate the level running number:

```
*KEYWORD--  ---NAME--- CH WEIG--ENERGY-- EION----- QN
LEVEL       N V 2S...1  4    2       0.0  789537.2
LEVEL       N V 2P...2  4    6   80635.7
LEVEL       N V 3S...3  4    2  456126.6
...
```

The LEVEL keyword specifies the definition of a new energy level in the DATOM file with the assigned name (NAME), the ionic charge (CH), the statistical weight of the level (WEIG) and the level energy in Rydberg (ENERGY). The ionization energy (EION) is listed only for the lowest level.

For each transition that should be considered in the formal integral the line transition has to be specified as follows:

```
*KEYWORD--UPPERLEVEL  LOWERLEVEL--EINSTEIN  RUD-CEY --COLLISIONAL COEFFICIENTS--
LINE      N V 2P...2  N V 2S...1-0.235         KB22    0.70
LINE      N V 3S...3  N V 2S...1             X KB24    0.05
LINE      N V 3S...3  N V 2P...2-3.233E-02     KB22    0.20
...
```

The LINE keyword defines a transition between the specified upper and lower energy level. Additionally, the Einstein coefficient (positive sign) or the oscillator strength (negative sign) of the transition need to be given. This can be followed by a keyword that marks rudimental lines (`X KB24`), i.e. such lines that have oscillator strength values in the range $0.01 > f \geq$ 1.E-98 and are only accounted for calculating the population numbers. This mark also influences the collisional coefficients. The `KB22` key marks allowed line transitions and takes the oscillator strength f for calculating the collisional coefficients as $\Omega_{\mathrm{KB22}} = 0.20 + 0.50 \cdot f$, while rudimental lines are calculated with $\Omega_{\mathrm{KB24}} = 0.05 + 0.95 \cdot f$.
Further keywords for the different atomic species exist to derive the collisional cross-sections in approximative ways. They were not used for the He II or N V extensions.

Finally, energy levels can give contributions to the continuum emission by photoionization or recombination. This is specified by the keyword CONTINUUM for each energy level.:

```
*KEYWORD  LOWERLEVEL ----SIGMA ----ALPHA ----SEXPO -IGAUNT- -CBFCODE --IONLEV--
CONTINUUM N V 2S...1    0.5       1.5        2.3
CONTINUUM N V 2P...2    1.64      1.5        2.6
CONTINUUM N V 3S...3    0.7       1.5        2.1
...
```

The photo cross-sections σ from the Opacity Project or the ones from Dr. Butler are fitted with the empirical formula by Seaton (1958)

$$\sigma = \sigma_{\mathrm{th}} \cdot x^{-s} \left[\alpha + \frac{(1. - \alpha)}{x} \right]^{-1} \tag{3.30}$$

where σ_{th} is the threshold cross-section, $x = \nu/\nu_{\mathrm{th}}$ the frequency in units of threshold frequency, s the exponent and α the . In some cases the hydrogenic cross-sections (SIGMA) are

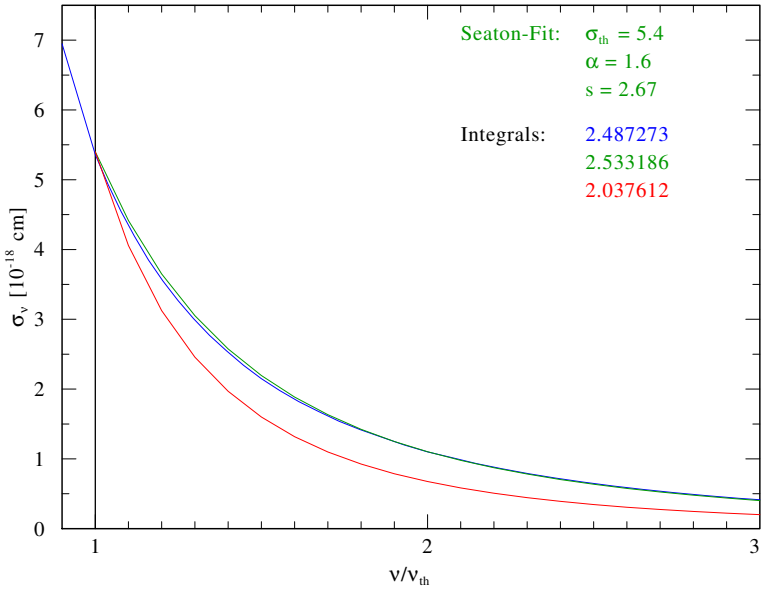

Figure 3.1: Photo-ionization cross-sections of the N V 5D..12 level, data from Dr. Butler (blue), Seaton-fit to the data (green), and hydrogenic approximation (red). For cross-checking, the integrals should give about the same area under each curve. The derived Seaton-fit parameters $\sigma_{\rm th}$, α, and s are applied for the continua in the DATOM file.

listed only. These are strictly valid for hydrogen-like ions but can be considered as a good approximation where no further details about cross-sections are available.

Two sets of DATOM files were compiled for the analysis, one with extended N II data to account for lower stellar temperatures. Table 3.2 gives an overview of the considered energy levels for each ionic species, without the separate iron-group elements. The highest ion just appears as control level. The implemented energy levels account for numerous lines to be calculated in the emergent spectrum, depending on the chosen spectral range.

Table 3.2: Number of energy levels in the applied DATOM files, the extended N II (DATOM-2) is considered for the cooler stars in the sample.

Ion	DATOM-1	DATOM-2
H I	10	10
H II	1	1
He I	17	17
He II	23	23
He III	1	1
N II	2	38
N III	33	33
N IV	38	38
N V	20	20
N VI	1	1
C II	32	32
C III	40	40
C IV	21	21
C V	1	1
total	240	276

FORMAL_CARDS

The final step in the model calculations is to obtain the integrated spectrum in the observers frame. For this attempt it is necessary to specify the line transitions that should be included in the formal integral. This information is supplied with a specific file, FORMAL_CARDS , that contains line transitions and multiplet transition comprising several subsystems of lines.

The more complex and complete the FORMAL_CARDS file, the more detailed the spectrum. But this advantage has to be bought by computational efforts, e.g. array size and computing time.

```
...
+LINE ???
UPPERLEVEL=HE II....7 LOWERLEVEL=HE II....3
...
+MULTIPLET ?
UPPERLEVEL=N V 2P...2 LOWERLEVEL=N V 2S...1
/LOWERLEVEL N 05..1..2    2              0.000
/UPPERLEVEL N 05..2..2    2          80463.200
/UPPERLEVEL N 05..2..4    4          80721.900
/SUBLINE N 05..2..2  N 05..1..2-0.783E-01     1242.80
/SUBLINE N 05..2..4  N 05..1..2-0.157E+00     1238.82
-MULTIPLET
...
```

Chapter 4

Analysis of the WN Stars

In this chapter, we present the analysis of the Quintuplet WN stars WR 102d, WR 102i, WR 102hb, WR 102ea, and the Of/WN star LHO 110. The observed K-band spectra are modeled with the Potsdam Wolf-Rayet (PoWR) model atmospheres to derive the fundamental stellar parameters: temperature, radius, luminosity, mass, mass-loss rate. The mass-loss rates determined from the analysis of the K-band spectra are compared with mass-loss rates derived from radio emission measurements for the sample stars, WR 102d, WR 102ea and LHO 110.

Finally, the results are discussed in the context of stellar evolution. We compare the characteristics of the sample stars with previous analyses of WN stars in the Arches cluster (Martins et al. 2008), two WR stars nearby the Quintuplet cluster (Barniske et al. 2008), and Galactic field WN stars (Hamann et al. 2006). Evolutionary tracks with and without rotation from Meynet & Maeder (2003b) are compared to the stellar parameters to determine initial and present masses of the stars, and their age. The results of this spectral analysis of the WN stars are prepared for publication (Liermann et al., submitted).

4.1 WN stars in the Quintuplet cluster

In Sect. 2.3 the total number of WR stars in the LHO catalog is 13 with 4 WN and 9 WC stars. This number is slightly smaller than the number of known WR stars in the Quintuplet cluster (van der Hucht 2006, 6 WN stars among 17 WR stars in total) due to the limited field-of-view of the observations being focused on the central region of the cluster. However, the presented analysis concentrates on these four WN stars. Additionally, the star LHO 110 star is analyzed which shows an interesting spectrum with emission lines and was classified as Of/WN (?), see Table 4.1.

The flux-calibrated spectra for these sample stars from the LHO catalog analyzed with respect to prominent spectral features, see Table 4.2. Tailored PoWR models are fitted to the observations to derive the stellar parameters.

4.2 The analysis

4.2.1 WN model fitting

As explained in Sect. 3.3, the emission line spectra of WN stars can be parameterized with the stellar temperature T_* and the transformed radius R_t. The Potsdam group has established

Table 4.1: Details of the sample stars from the LHO catalog (Liermann et al. 2009). The Q identifiers are from Glass et al. (1990), the QR radio source from Lang et al. (1999), and WR names are from van der Hucht (2006).

LHO No.	R.A. 17^h 46^m [s]	Dec. -28 ° 49′ [″]	Spectral type	Alias names
67	15.92	37.6	WN9	**Q 8**, WR 102hb
71	15.13	37.0	WN9	**Q 10**, WR 102ea, QR 5
99	16.54	31.5	WN9	WR 102i
110	15.09	29.4	O6-8 I f (Of/WN?)	**Q 15**, QR 4
158	14.05	16.6	WN9	WR 102d, QR 8

Table 4.2: Spectral lines considered for the WN analysis.

dominant lines	additional lines
He I(1s2s ^{1}S–1s2p ^{1}P) $\lambda\,2.059\,\mu$m	He II (8–15) $\lambda\,2.038\,\mu$m
He I(1s3p ^{1}P–1s4s ^{1}S) blend, $\lambda\,2.113\,\mu$m	He II (8–13) $\lambda\,2.347\,\mu$m
He II(7–10) $\lambda\,2.189\,\mu$m	He II (9–22) $\lambda\,2.216\,\mu$m
Br γ/He II(8–14) blend, $\lambda\,2.165\,\mu$m	He II (9–21) $\lambda\,2.261\,\mu$m
	N V $\lambda\,2.317\,\mu$m

two grids [1] of WN-type models, which are calculated with a hydrogen abundance of 20% by mass (WNL grid) and for hydrogen-free stars (WNE grid). The analysis starts with models from this grid basis to find reference models.

The fit of an emission line spectrum is an iterative process. A model is chosen such that it reproduces the observed spectral features. Simultaneously the model continuum fitted to the spectral energy distribution is applied to normalized the emission line spectrum. The two steps are described in the following separately.

Emission line spectrum All sample stars in this work are of late spectral type with signatures of hydrogen in their spectra (WN9h), the WNL grid was applied to find reference models. The basic model parameters T_* and R_t are chosen such that all lines in the spectra could be reproduced. A fixed terminal wind velocity $v_\infty = 1000\,\mathrm{km\ s^{-1}}$ is set in this grid. In the next step, tailored models were calculated with adjusted v_∞ and hydrogen abundance to match the line widths and the height of the Br γ/He II blend. Additionally, models with different metallicities were calculated to test for a possible metal enrichment or depletion, see Sec. 4.3.3. The best fitting model for each WN star is shown in Fig. 4.2.

Spectral energy distribution The spectral energy distribution (SED) for the near-infrared spectral range is fitted to the observed flux-calibrated K-band spectrum as shown in Fig. 4.1. The model-continuum flux (dotted lines) is reddened following the law tabulated by Moneti et al. (2001) for the infrared range below $24\,\mu$m, and adjusted to match the star's luminosity. The available spectra just cover the K-band, therefore photometry marks from the 2MASS J, H and K_s-band (Skrutskie et al. 2006) are applied in addition to the LHO-K_s magnitude to adjust the shape of the model SED properly, see Fig 4.1. Further details on the reddening and extinction are discussed in Sec. 4.3.6.

Unfortunately, the 2MASS photometry is of very poor quality for WR 102d. The listed values are without error bars and could therefore only be considered as upper limits on magnitudes. Additionally, a coordinate offset of almost $5''$ is found between the 2MASS position and the LHO position of WR 102d. The 2MASS coordinates rather match LHO 147 (see also Table B.1). Besides, data from the 2MASS *intermediate release* catalog (Skrutskie et al. 1997), although considered to be obsolete, are on the LHO position of WR 102d and fit the SED very well. Therefore, these magnitudes are adopted and plotted together with the SED in Fig. 4.1. Towards the crowded cluster center it cannot be ruled out that the photometry was affected by nearby sources. This crowding also does not allow further photometry in the

[1] `http://www.astro.physik.uni-potsdam.de/PoWR.html`

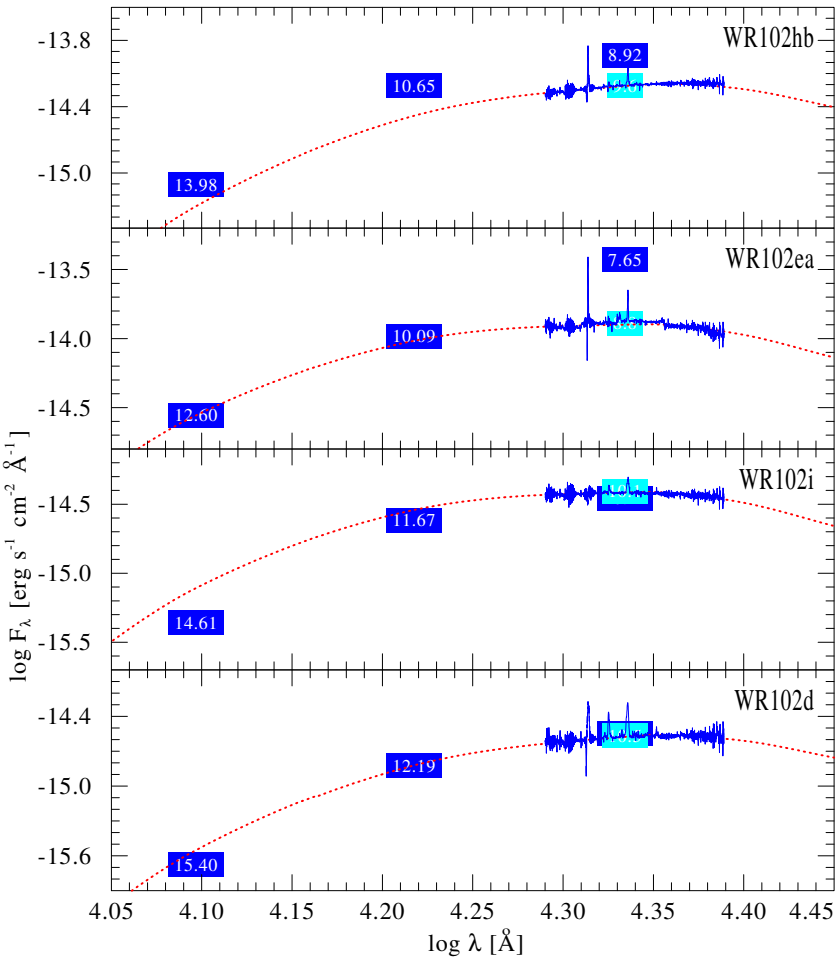

Figure 4.1: Spectral energy distributions for the sample WN stars. The flux-calibrated spectrum (solid line) is fitted with the model continuum (dotted line), blocks refer to the 2MASS and LHO magnitudes.

mid-IR to be obtained. Both the archives of SPITZER-IRAS and MSX were searched for data, but they list only fluxes for the cluster in total without resolving individual sources. However, the slope of the SED is reproduced very well in each case, given the small spectral range that is available.

4.2.2 LHO 110

The star LHO 110 was classified as O6-8 Ife in the LHO catalog. Its emission line spectrum is very similar to the spectral appearance of the WN stars, although the spectral features are less pronounced. In detail, the star has a similar K_s magnitude as the WN sample stars and also shows similar line ratios for (He II 2.189 μm)/(Br γ/He II 2.166 μm) and (Br γ)/(He I 2.058 μm). Therefore, LHO 110 was additionally classified as Of/WN "slash" star and included in this analysis.

The emission line spectrum and SED were fitted as described above for the WN stars, see Fig 4.3. However, as in the case of WR 102d the flux-calibrated spectrum and model SED cannot be matched with the 2MASS photometry. As the star lies in the central region of the cluster crowding might have affected the 2MASS measurements. For the emission

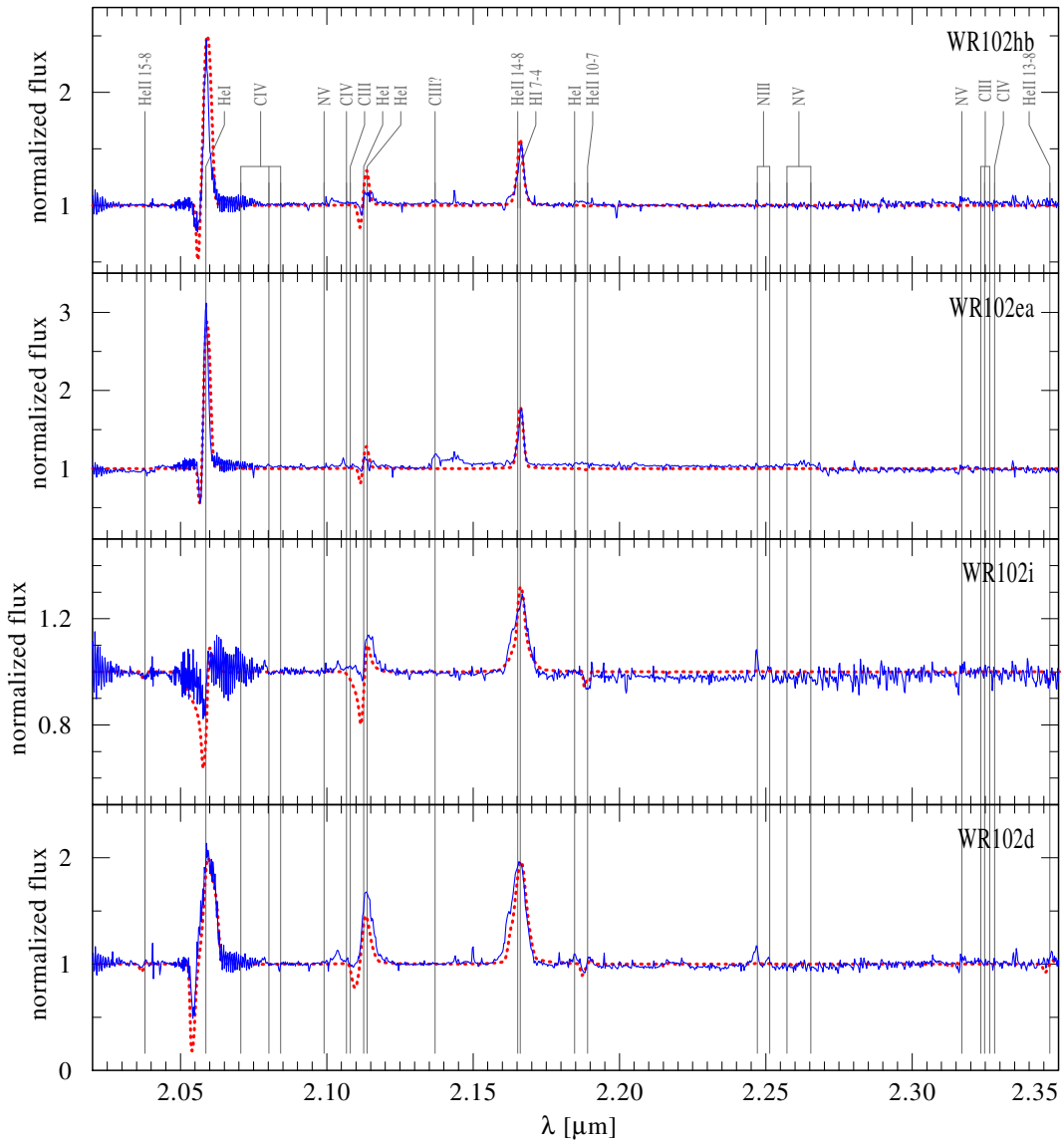

Figure 4.2: Emission line spectra of the sample WN stars (solid lines), normalized with their reddened model continuum. The observed spectra are corrected for radial velocities according to Table 2 in the LHO catalog. The model spectrum is overplotted (dotted lines).

line spectrum (Fig. 4.3 lower panel), the Br γ/ He II blend cannot be reproduced very well. After the normalization with the model continuum the observed spectrum seems somewhat depressed in this region. The fit is a challenge with respect to the determination of the hydrogen abundance, see Sect. 4.3.3.

Additionally, a set of small absorption lines is found in the spectrum, which cannot be identified unambiguously. Thus, it might be possible that LHO 110 is a binary star. However, binary WR stars tend to be bright in X-rays, but LHO 110 is not detected as an X-ray source, as none of the other sample stars is either (Wang et al. 2006). The lack of X-ray detection of the sample stars is consistent with the stars being single and further observation would be necessary to detect photometric and spectral variability.

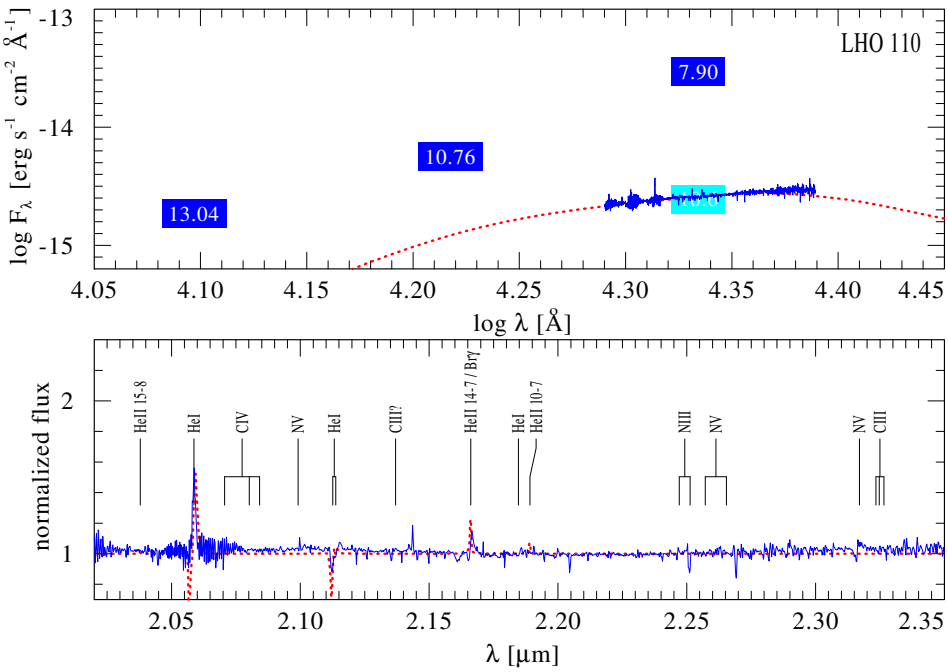

Figure 4.3: SED (upper panel) and emission line spectrum (lower panel) of LHO 110. 2MASS and LHO K_s magnitudes are indicated. The flux-calibrated spectrum (solid lines) is fitted with the (dotted lines).

4.3 Results

4.3.1 Stellar parameters

From fitting the emission line spectrum the stellar temperature T_* and the transformed radius R_t are obtained directly. The stellar radius R_* is calculated with the Stefan-Boltzmann law from the luminosity L and temperature T_*. Since the terminal velocity v_∞ and the clumping factor D were specified as model input the mass-loss rate can be derived from the transformed radius. The results for each star are given in Table 4.3.

Table 4.3: Stellar parameters for the analyzed stars in the Quintuplet cluster.

LHO No.	K_s [mag]	T_* [kK]	R_t [$R_\odot$]	v_∞ [km/s]	X_H [%]	E_{b-v} [mag]	M_K [mag]	R_* [$R_\odot$]	log $\dot{M}$ [$M_\odot$/a]	log L [$L_\odot$]	$\frac{\dot{M}v_\infty}{L/c}$
67	9.6	28.18	25.11	400.	10	7.85	-7.65	74.79	-4.39	6.50	0.3
71	8.8	28.18	25.11	300.	15	6.1	-7.84	74.79	-4.51	6.50	0.1
99	10.1	31.62	31.62	1000.	20	6.3	-6.61	41.10	-4.53	6.18	1.0
158	10.5	35.48	12.58	700.	22	7.1	-6.49	28.11	-4.33	6.05	1.4
110	10.6	28.18	39.81	300.	1	8.7	-6.95	62.21	-4.93	6.34	0.1

The derived empirical mass-loss rates versus stellar luminosity are shown in Fig. 4.4 with the mass-luminosity relation of Nugis & Lamers (2000). All sample stars fall below the re-

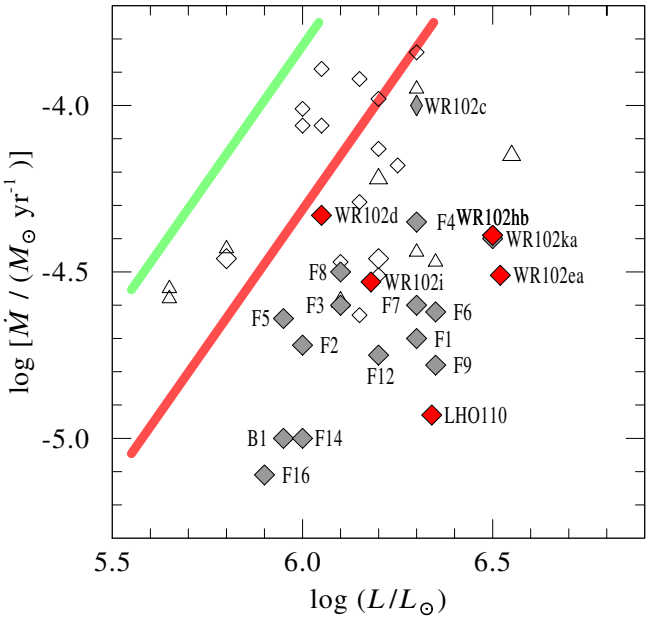

Figure 4.4: Mass-loss rate versus stellar luminosity for the sample stars. Arches WNL stars from Martins et al. (2008, labeled with F and B numbers), WR102c and WR102ka from Barniske et al. (2008), and Galactic WN stars (Hamann et al. 2006, open symbols) are shown for comparison. The solid lines refer to the mass loss–luminosity relation of Nugis & Lamers (2000) for hydrogen-free stars (upper line) and stars containing 40 % hydrogen per mass (lower line).

lation for stars containing 40 % hydrogen (lower line), but from their determined hydrogen abundances of $X_\mathrm{H} \leq 0.2$ (by mass) they show lie between this relation and the one for hydrogen-free stars (upper line). With respect to the high luminosities, the stars have rather low mass-loss rates. The same is true for other Galactic WN stars of similar spectral subtype and hydrogen abundance, included in Fig. 4.4: Hamann et al. (2006, open symbols), Arches WNL stars (Martins et al. 2008, labeled B and F), and Barniske et al. (2008, WR 102c and WR 102ka).

From the stellar parameters the wind efficiency number $\eta = \dot{M} v_\infty c/L$ can be derived as well. In the theory of radiation-driven winds (Castor et al. 1975, CAK), this number cannot exceed unity, i.e. each photon can just transfer energy and momentum to an atom or ion once, and multiple scattering is not taken into account. Gräfener & Hamann (2005, 2008) have shown that η-values of a few can easily be obtained in hydrodynamically self-consistent WR models with full radiative transfer. However, in this work these models were not applied, but values of η close to unity are found for all sample stars (see Table 4.3), implying that these stellar winds are driven by radiation.

Further on, for radiation-driven winds the modified wind momentum D_mom should depend on the luminosity (i.e. spectral type respectively) only and result in a wind momentum-luminosity relation (WLR) (e.g. Puls et al. 1996; Kudritzki & Puls 2000; Vink et al. 2000). Thus, $D_\mathrm{mom} = \dot{M} v_\infty \sqrt{R_*}$, with $\dot{M}$ and v_∞ in cgs-units, and R_* in $R_\odot$ is derived for all sample stars with the parameters given in Table 4.3, see Fig. 4.5. For the Arches WNL stars D_mom is calculated from the parameters given in Martins et al. (2008, Table 2). The dashed line in

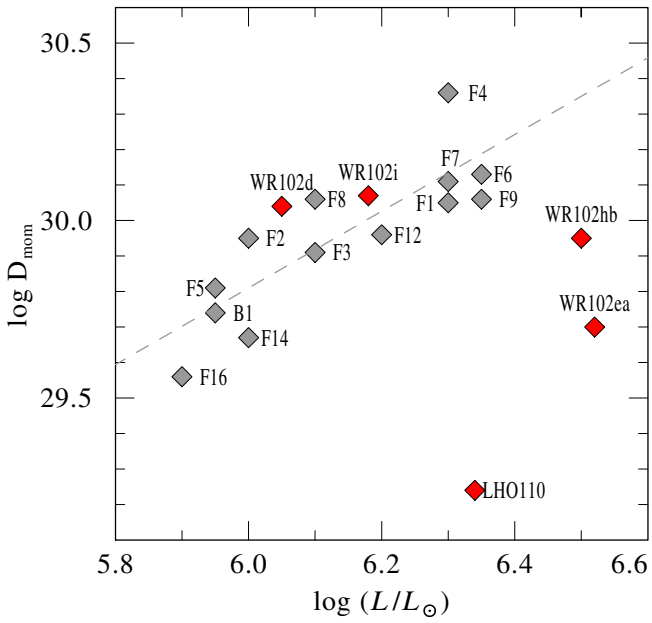

Figure 4.5: Wind momentum versus luminosity for the Quintuplet WN. For comparison the Arches stars are show with the derived modified wind momentum-luminosity relation (WLR) for WNLh stars (Martins et al. 2008, dashed line), and the WLR for O supergiants is shown as well (Kudritzki & Puls 2000, solid lines).

Fig. 4.5 presents their derived WLR

$$\log D_{\rm mom} = 1.08 \log L/L_\odot + 23.33\,. \tag{4.1}$$

This relation is slightly steeper than that those for O stars, indicating different evolutionary phases of the stars. The Quintuplet WN stars show a large scatter around this WLR. However, the limited number of stars in the sample render it unreasonable to derive a WLR from the Quintuplet WN stars alone. Together with the wind efficiency numbers discussed above, the obtained $D_{\rm mom}$ strengthen the indication that the stellar winds of the Quintuplet WN stars are driven by radiation.

Since the mass-loss rates of radiation-driven stellar winds scale with the metallicity (Gräfener & Hamann 2008), the low mass-loss rates derived in this work are an indirect argument that the metallicity in the Quintuplet WN stars cannot be significantly higher than in other Galactic WN stars.

The assumption that the Galactic Center might be metal enriched is still under debate. Najarro et al. (2004) found solar abundances ($Z_\odot$) for a sample of stars in the Arches cluster, while later results on a larger sample in the same cluster favored a slight metal enrichment in the range of 1.3-1.4 $Z_\odot$ (Martins et al. 2008). In the Quintuplet region, solar iron abundances were found for the nearby Pistol star and FMM 362 by Najarro (2006); Najarro et al. (2009). A red supergiant in the Quintuplet cluster, LHO 7 (GMM 7), was analyzed by Davies et al. (2009) who determined slight super-solar iron abundances. The authors argue that this result can originate from the evolved state of the object and the corresponding hydrogen depletion. Thus, the "initial" iron abundance would be in agreement with solar values. It has to be acknowledged that a sample of four WN stars is not large enough to draw strict conclusions on the metal abundances in the Quintuplet

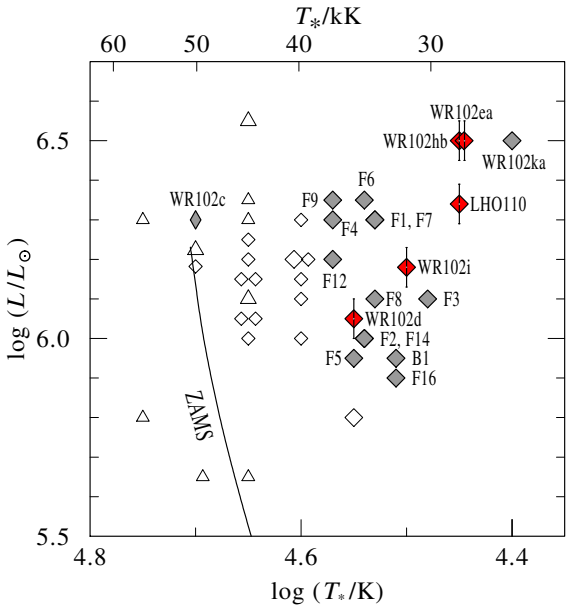

Figure 4.6: HRD showing the analyzed Quintuplet WN stars. The same WNL stars as in Fig. 4.4 are shown for comparison and the hydrogen main sequence is indicated.

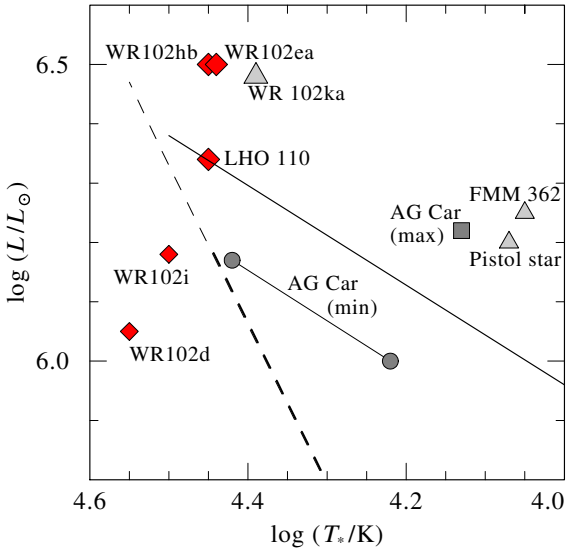

Figure 4.7: HRD with the LBV (candidate) stars from Table 4.4. The empirical Humphreys-Davidson limit (solid line) and the hot LBV minimum light strip (dashed line) are indicated.

The Hertzsprung-Russell diagram (HRD, Fig. 4.6) shows the sample stars compared to other Galactic WN stars, the Arches WNL stars (same symbols as in Fig. 4.4), and WR102c and WR102ka, in the vicinity of the Quintuplet. Both, the Arches and the Quintuplet WN stars, are located in the same position in the HRD as the Galactic WN stars of the same spectral subtype, i.e. WN7-9. These stars form a group of cool, $T_* \leq 50\,000\,\mathrm{K}$ but very luminous WN stars with $\log(L/L_\odot) > 6.0$, and still contain a significant amount of hydrogen. Their evolutionary status is discussed in Sec. 4.3.5.

4.3.2 LBV candidates?

The LBV phenomenon is a morphological classification for the very massive early-type stars, that are suspect to undergo periodical mass loss (van Genderen 2001). The classification is based primarily on the photometric variability, e.g. the brightness can vary up to almost two magnitudes. Two phases can be distinguished, a phase of eruption with high luminosity at cooler temperatures and a quiescent phase with lower luminosity at high temperatures. Further fundamental parameters change between these phases, e.g. the stellar radius, the terminal wind velocity, and the mass-loss rate, resulting also in a spectroscopic variability. From a "snapshot" spectrum, as available for this work, it is not possible to draw conclusions on the variability of the star. However, three stars in the sample, WR102ea, WR102hb, and LHO 110, have very high luminosities and low terminal velocities.

In Table 4.4, parameters of different Galactic LBVs are compared, including the well know LBV prototype AG Car. From this star, it can be seen that even the stellar parameters derived from different minimum epochs of the LBV phase over the last 20 years can differ significantly (Groh et al. 2009). The parameters derived for the sample stars in this work

Table 4.4: Comparison of the stellar parameters of the Quintuplet LBV candidates with AG Car.

star	T_* [kK]	$\log L$ [$L_\odot$]	v_∞ [km s^{-1}]	$\log \dot{M}$ [$M_\odot$ a^{-1}]	reference
WR 102ea	28.2	6.50	400	-4.39	this work
WR 102hb	28.2	6.50	300	-4.51	this work
LHO 110	28.2	6.34	300	-4.93	this work
Pistol	11.8	6.20	105	-4.68	Najarro et al. (2009)
FMM 362	11.3	6.25	170	-4.92	Najarro et al. (2009)
WR 102ka	25.1	6.50	400	-4.40	Barniske et al. (2008)
AG Car (min.)	16.7/26.5	6.00/6.17	105/300	-4.82/-4.22	Groh et al. (2009)
AG Car (max.)	13.5[a]	6.22[a]	40[b]	-3.83[b]	[a] van Genderen (2001)
					[b] Stahl et al. (2001)

are comparable to those of the other Galactic LBVs, leading to the conclusion that the stars might be LBV candidates.

Fig. 4.7 shows all sample stars and the Galactic LBVs from Table 4.4 in the HRD. LHO 110 is located just at the empirical Humphreys-Davidson limit adapted from Figer et al. (1998, their Fig 12), with the other Quintuplet LBV candidates above this relation. Clark et al. (2005a) proposed an empirical lower limit for LBV (candidate) stars in the quiescent state: the hot LBV minimum light strip. It is defined up to luminosities $\log(L/L_\odot) \sim 6.2$ by observed LBVs and LBV candidates, with a possible extension towards higher luminosities. These authors also discuss that LBV stars of such high luminosities might look like "regular" WNL stars. Maeder et al. (2008) recently described that stars with $M > 90\,M_\odot$ initial mass might skip the LBV phase completely in their evolution:

$$\mathrm{O} \rightarrow \mathrm{Of} \rightarrow \mathrm{WNL} \rightarrow (\mathrm{WNE}) - \mathrm{WCL} \rightarrow \mathrm{WCE} \rightarrow \mathrm{SN}\,.$$

From the comparison with evolutionary tracks, see Sect. 4.3.5, all three stars should have initial masses between 150 and 200 $M_\odot$. Further observations are needed to finally settle the status of these stars.

4.3.3 Hydrogen abundance

The basic chemical abundance that was determined in this work is the hydrogen abundance X_H (mass fraction) . Models with different X_H were calculated and fitted to the spectra. The Br γ/He II blend is very sensitive to the hydrogen abundance. A detail plot of the observed spectrum showing the Br γ/He II blend with the best-fitting model is shown in Fig. 4.8 for the WN stars. For comparison models with different X_H are overplotted (dashed and dash-dotted lines) estimating a systematic error of $\pm 5\,\%$ on the determined abundances.

In the case of LHO 110, the fit of the emission line spectrum was difficult with respect to the Br γ/He II blend. The spectrum seems somewhat depressed in this region after the normalization with the model continuum, see Fig. 4.9. The resulting hydrogen abundance of $X_\mathrm{H} \sim 1\,\%$ has to be considered as a very rough estimate.

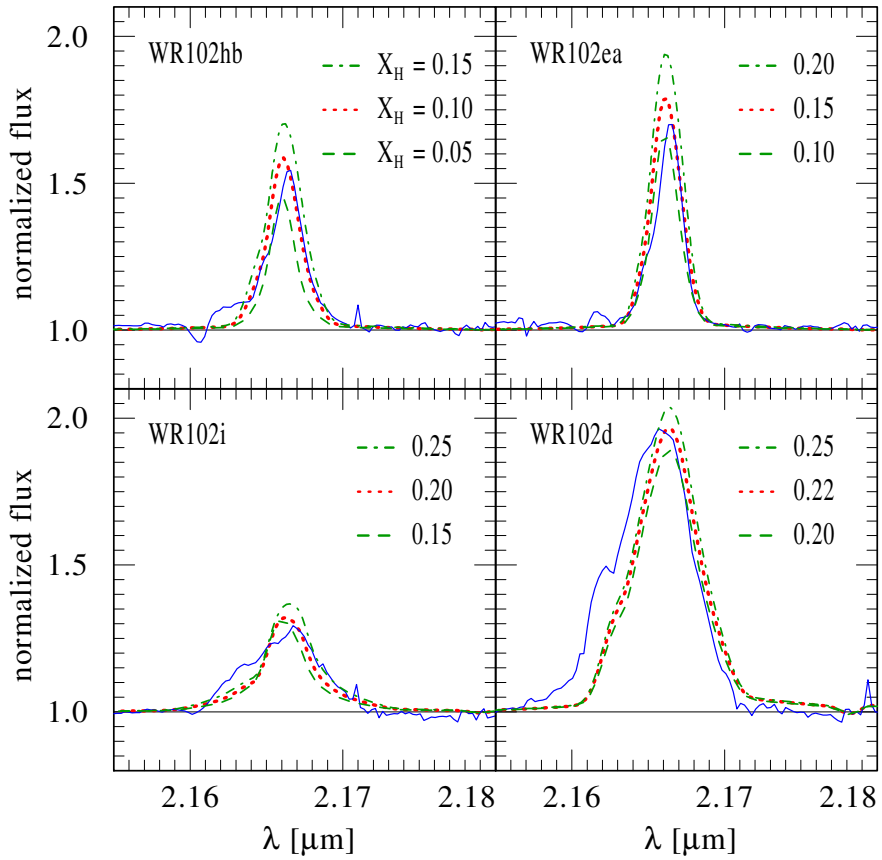

Figure 4.8: Hydrogen abundances determined for the sample WN stars from the Br γ/He II blend at 2.165/6 μm. The observed spectra (solid lines) are fitted with models containing different mass fractions of hydrogen.

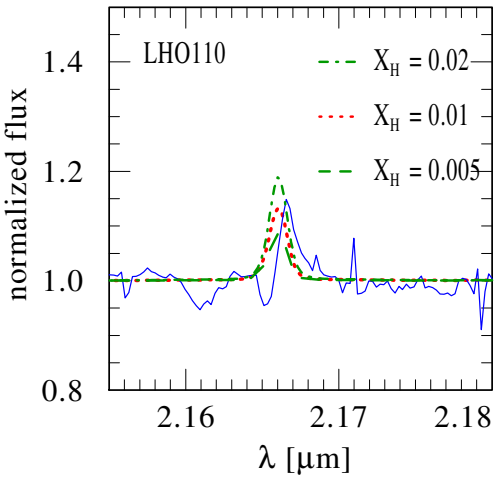

Figure 4.9: Detail of the observed LHO 110 spectrum showing the Br γ/He II blend (solid line) fitted with models of different hydrogen abundance.

4.3.4 Radio mass-loss rates

Historically, the first observations to overcome the visual extinction towards the Galactic center were radio observations. With the discovery of the GC massive stellar clusters in the infrared it became natural to observe these in the radio range as well. From the LHO catalog three stars are detected in radio (Lang et al. 2005): WR 102ea (QR 5), WR 102d (QR 8), and LHO 110 (QR 4).

The radio emission is attributed to the thermal free-free emission of ionized wind material. Under the assumption of a stationary, spherical wind of completely ionized gas that is expanding with constant velocity, the stellar mass-loss rates can be derived from the radio free-free emission as proposed by Wright & Barlow (1975)

$$\dot{M} = v_\infty \frac{f_\nu^{3/4}\, d^{3/2}}{(23.2)^{3/4}(\gamma g_{\rm ff}\nu)^{1/2}} \left(\frac{\mu}{Z}\right) . \tag{4.2}$$

The parameters are the observed radio flux f_ν at frequency ν, the free-free Gaunt factor $g_{\rm ff}$, the distance of the object d, the mean molecular weight μ, the mean number of electrons γ, and the mean ionic charge Z. For WR stars, it is expected that the radio emission arises far out in the stellar wind were the material is already moving with constant velocity $v = v_\infty$. The terminal velocity and mean molecular weight are taken directly from the individual models of each star (see Table 4.5). If helium stays ionized in the radio emitting region, the mean number of electrons and the mean ionic charge are assumed to be $\gamma = Z = 1$. A cluster distance of 8 kpc is adopted (Reid 1993). To derive the free-free Gaunt factor with the relation by Leitherer & Robert (1991)

$$g_{\rm ff} = 9.77 + 1.91 \log T_{\rm e} - 1.2701 \log Z\nu \,, \tag{4.3}$$

the mean electron temperature is taken to be 10 000 K. Radio-flux measurements from Lang et al. (2005) and the radio mass-loss rates derived in this work are listed in Table 4.5. For comparison the original mass-loss rates from Lang et al. (2005) derived under the assumption of $v_\infty = 1000\,\mathrm{km/s}$ and $\mu = 2$ are listed as well.

The radio mass-loss rates of QR 5(WR 102ea) and QR 8 (WR 102d) agree very well with the ones obtained from the model analysis of the K-band spectrum (see Table 4.5). Thus, both radio sources can be confirmed as stellar wind radio emission.

However, radio mass-loss rates were derived for an unclumped wind ($D = 1$), while the models applied to determine the mass-loss rate from the K-band spectra were calculated under the assumption of a slightly clumped wind ($D = 4$) . Since the mass-loss rate scales with $\dot{M} \propto D^{-1/2}$, the unclumped mass-loss rates from the IR analysis would be 0.3 dex higher than the clumped ones. The spectral lines detected in the K-band spectra of the stars arise close to the wind base, while the radio free-free emission emerges at larger stellar radii. Indications for a radial dependence of the clumping were found for O stars (Puls et al. 2006) and WR stars (Liermann & Hamann 2008). From the ratio of the clumping factors $D_{\rm IR}/D_{\rm radio}$ listed in Table 4.5 it can be concluded that clumping is less pronounced in the radio emitting region for QR 5 (WR 102ea) and QR 8 (WR 102d).

In contrast, the mass-loss rate derived for QR 4 (LHO 110) from the Wright & Barlow model does not compare well to the one derived from the K-band spectrum. The radio flux measured for this star is brighter then expected. As LHO 110 lies in the more crowded cluster center, already Lang et al. (2005) found that the measurements might be affected by extended radio emission from nearby structures such as the Sickle and Pistol H II regions. The unclear nature of LHO 110 as possible binary might also imply radio emission from a colliding-wind

Table 4.5: Mass-loss rates derived from radio free-free emission ($\dot{M}_{\rm radio}$) compared to those derived from the K-band spectral analysis ($\dot{M}_{\rm IR}$) and the original values derived by Lang et al. (2005, $\dot{M}_{\rm Lang}$) who adopted $v_\infty = 1000\,{\rm km/s}$ and $\mu = 2$ for all stars. Additionally, the ratio of clumping factors is given.

star	v_∞ [km s^{-1}]	μ	ν [GHz]	f_ν [mJy]	$\log \dot{M}_{\rm radio}$ [$M_\odot$ a^{-1}]	$\log \dot{M}_{\rm Lang}$ [$M_\odot$ a^{-1}]	$\log \dot{M}_{\rm IR}$ [$M_\odot$ a^{-1}]	$D_{\rm IR}/D_{\rm radio}$
WR102ea	300.	2.78	4.9	0.35	-4.54			
(QR 5)			8.5	0.54	-4.50			
			22.5	1.50	-4.36	-3.96	-4.51	3.3
WR102d	700.	2.52	4.9	0.24	-4.34			
(QR 8)			8.5	0.28	-4.39			
			22.5	0.57	-4.34	-4.37	-4.33	4.6
LHO 110	300.	3.09	4.9	0.60	-4.32			
(QR 4)			8.5	1.30	-4.17	-3.82	-4.93	0.2

zone (CWZ). However, this emission often shows a non-thermal radio spectrum. According to Lang et al. (2005) the radio spectral index of QR 4 (LHO 110) is +1.4 being more indicative for a thermal radio spectrum. Thus, the status of LHO 110 remains unsettled.

4.3.5 Stellar evolution

Massive stars with initial masses above $20\,M_\odot$ are supposed to pass the WR phase after they left the main sequence. In dependence of the initial stellar mass evolutionary scenarios are possible, which might exclude specific phases such as the blue or red supergiant (BSG/RSG) or LBV phase completely. For example Crowther (2007) proposed

$$M_{\rm init} \sim 25\text{-}40\,M_\odot:\ {\rm O} \rightarrow {\rm LBV/RSG} \rightarrow {\rm WN\ (H\text{-}poor)} \rightarrow {\rm SN\,Ib}$$

$$M_{\rm init} \sim 40\text{-}75\,M_\odot:\ {\rm O} \rightarrow {\rm LBV} \rightarrow {\rm WN\ (H\text{-}poor)} \rightarrow {\rm WC} \rightarrow {\rm SN\,Ic}$$

$$M_{\rm init} > 75\,M_\odot:\ {\rm O} \rightarrow {\rm WN\ (H\text{-}rich)} \rightarrow {\rm LBV} \rightarrow {\rm WN\ (H\text{-}poor)} \rightarrow {\rm WC} \rightarrow {\rm SN\,Ic}\,,$$

while Maeder et al. (2008) discuss alternative ways for the most massive stars, e. g.

$$M_{\rm init} > 60\text{-}90\,M_\odot:\ {\rm O} \rightarrow {\rm Of/WNL} \leftrightarrow {\rm LBV} \rightarrow {\rm WNL\ (H\ poor)} \rightarrow {\rm WCL/E} \rightarrow {\rm SN\,IIn?}$$

$$M_{\rm init} > 90\,M_\odot:\ {\rm O} \rightarrow {\rm Of} \rightarrow {\rm WNL} \rightarrow {\rm (WNE)} \rightarrow {\rm WCL} \rightarrow {\rm WCE} \rightarrow {\rm SN\ (Hypernova?)}\,.$$

However, in any evolutionary sequence the luminous late-type WN stars (WNL) are an interphase between O stars leaving the main-sequence and WR stars of the carbon sequence (WC), before these massive stars explode as supernova (SN). The details of the different transition phases are not yet completely understood.

The analyzed Quintuplet WN stars are shown in an HRD with evolutionary tracks from Meynet & Maeder (2003b, Geneva tracks) , see Fig. 4.10. The tracks were calculated for solar metallicity and different initial masses including the effects of rotation. All sample stars lie at or above the tracks with $M_{\rm init} > 60 M_\odot$. This implies that the stars are descendants from very massive O stars. As already observed for other Galactic WR stars (see Hamann et al. 2006)

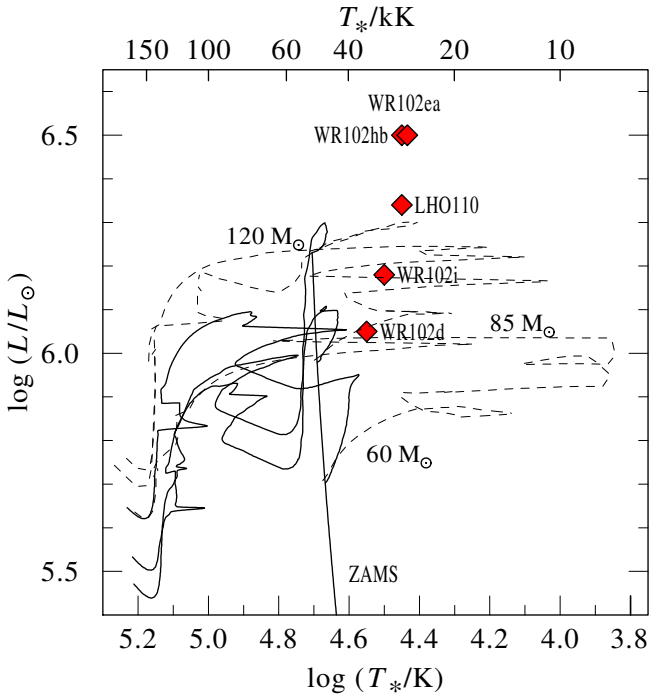

Figure 4.10: HRD with evolutionary tracks from Meynet & Maeder (2003b) for $M_{\rm init}$ of 60, 85 and 120 $M_\odot$. The dashed lines refer to tracks without rotation, solid lines to tracks with $v_{\rm init} = 300\,{\rm km\ s^{-1}}$.

the evolutionary tracks without rotation (dashed lines) extend further into the regime of lower temperatures than the tracks including rotation (solid lines). Thus, the initial equatorial rotational velocity might be lower than the 300 km/s assumed in the evolutionary models. The most massive evolutionary tracks which already yields an initial mass of 120 $M_\odot$ leaves two WN stars, WR102hb and WR102ea, quite isolated in the HRD. The derived stellar parameters of these stars are compared with evolutionary tracks by Langer et al. (1994) shown by Figer et al. (1998, Fig. 15a). This leads to an initial mass range of 150 to 200 $M_\odot$ and age estimate of >1.6 million years (Figer et al. 1998, Fig. 15b). For WR 102i, WR 102d, and LHO 110 stellar ages, initial and present-day masses are determined from the Geneva tracks. The results are listed in Table 4.6. Stellar masses can also be estimated from the empirical mass-luminosity relation for WN stars by Langer (1989)

$$\log \frac{M_{\rm WNE}}{M_\odot} = -0.158206 - 0.053868 \log \frac{L_{\rm WNE}}{L_\odot} + 0.055467 \left(\log \frac{L_{\rm WNE}}{L_\odot} \right)^2 , \qquad (4.4)$$

which agree well with those determined from the Geneva models, although the mass-luminosity relation is strictly valid for pure helium stars only. However, the derived present-day masses show that the stars already lost up to 50 % of their initial mass. Additionally, for those stars that are attributed to the Geneva tracks without rotation the comparable temperatures and luminosities reveal that the stars are still hydrogen burning objects, but the differences in the Geneva tracks with and without rotation imply that stellar evolution is not yet clearly understood.

Table 4.6: Age, initial mass ($M_{\rm init}$), and present-day mass ($M_{\rm WN}$) for the Quintuplet WN stars. The last column lists masses derived with the mass-luminosity relation by Langer (1989).

star	age [Ma]	$M_{\rm initial}$ [$M_\odot$]	$M_{\rm WN}$ [$M_\odot$]	$M_{\rm Langer}$ [$M_\odot$]
WR102hb	> 1.6	150-200	-	68
WR102ea	> 1.8	150-200	-	68
WR102i	3.1	85	40	42
WR102d	3.6	60	30	35
LHO 110	2.4	120	75	54

4.3.6 Extinction

From the fits of the spectral energy distribution of the sample stars, individual values for the interstellar reddening were determined. Table 4.7 lists the derived values and an average extinction of $A_K = 3.1 \pm 0.5$ mag for the Quintuplet cluster, which is similar to the one derived in previous studies by Barniske et al. (2008, WR 102c and WR 102ka) and Figer et al. (1999a). A slightly lower average extinction $A_K = 2.8$ mag was found for the Arches cluster

Table 4.7: Extinction derived from the model SED fit to the flux-calibrated spectra.

Object	A_V [mag]	A_K [mag]	ref.
WR102hb	29	3.3	this work (t.w.)
WR102ea	23	2.6	t.w.
WR102i	24	2.7	t.w.
WR102d	27	3.0	t.w.
LHO 110	33	3.7	t.w.
mean	27 ± 4	3.1 ± 0.5	t.w.
WR102c	26 ± 1	2.9 ± 0.1	Barniske et al. (2008)
WR102ka	27 ± 5	3.0 ± 0.6	Barniske et al. (2008)
Quintuplet mean	29 ± 5	3.28 ± 0.5	Figer et al. (1999a)
Arches mean	24.9	2.8	Martins et al. (2008)

by Martins et al. (2008). Absolute magnitudes derived with the individual reddening are listed in Table 4.3 for each sample star.

Due to the limited sample of analyzed stars it is not possible to derive an extinction map for the Quintuplet cluster, but a slight increase of the derived extinction towards LHO 110 located more in the cluster center is found, see Fig. 4.11. While the main contribution of the extinction is attributed to the foreground interstellar reddening, an intrinsic cluster extinction can be expected from the presence of dust-producing WC stars ("pinwheel stars") in the cluster center (Tuthill et al. 2006).

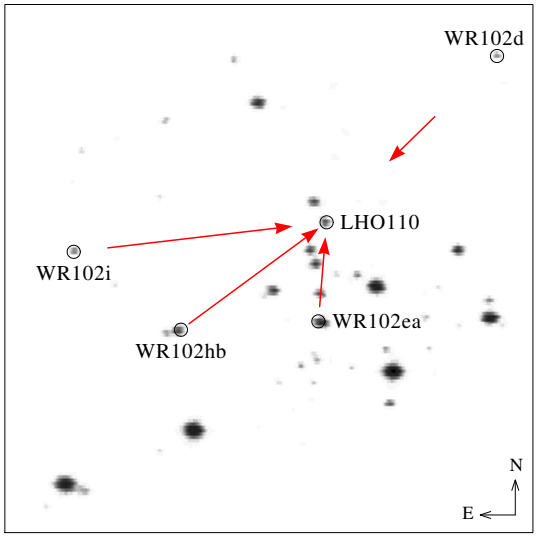

Figure 4.11: Quintuplet map with the location of the sample stars. The determined individual values of the reddening show an increase towards the cluster center, i. e. towards the star with the highest determined extinction (LHO 110) in the sample. The lengths of the arrows indicate the gradient.

4.4 Summary

The presented analysis of the four WN9h stars and one WN9/Of star in the Quintuplet cluster is the first spectroscopic study aimed at the determination of the fundamental stellar parameters by fitting tailored Potsdam non-LTE model atmospheres (PoWR) to the observed flux-calibrated K-band spectra.

The stars have stellar temperatures of 28 000 to 35 000 K corresponding to their late spectral subtype and are very luminous $\log(L/L_{\odot}) > 6.0$. A significant amount of hydrogen up to $X_{\mathrm{H}} \sim 0.2$ by mass is still present in the stellar atmospheres and the derived mass-loss rates and wind characteristics correspond to radiation-driven winds. Additionally, from the obtained wind parameters indirect arguments indicate that the WN stars in the Quintuplet cluster are not metal enriched as suspected for the Galactic center.

Three stars of the sample are detected as radio sources. For WR 102ea (QR 5) and WR 102d (QR 8) their radio emission can be attributed to the free-free emission originating in their stellar winds. For, LHO 110 (QR 4), its radio emission is too bright for this assumption and might be caused by colliding winds in a binary. Further observations are needed to settle its status.

From comparison with evolutionary models, the initial masses indicate that the Quintuplet WN stars are descendants from the most massive O stars with $M_{\mathrm{init}} > 60 M_{\odot}$ and their ages correspond to the cluster age of 3-5 million years. The location of the stars in the HRD is fitted better with evolutionary tracks without rotation, also indicating that these stars are still core-hydrogen burning objects.

An average extinction of $A_K = 3.1 \pm 0.5$ mag ($A_V = 27 \pm 4$) towards the Quintuplet cluster was derived from the analysis of the individual sample stars.

Chapter 5

Cluster Properties

This chapter focuses on the discussion of the results obtained in the preceeding analysis in context with the Quintuplet cluster in general. The Galactic rotation curve and the cluster radial velocity are applied to evaluated the position of the Quintuplet in the Galaxy. Further on, effective temperatures and luminosities are derived for the early-type and late-type stars in the LHO catalog to establish a Hertzsprung-Russell diagram, which is compared to stellar evolutionary models and isochrones. The stellar population, age and possible evolution of the Quintuplet cluster are compared to other Galactic clusters.

5.1 Stellar clusters

Stellar clusters are unique objects to study stellar populations and their evolution. In general, all cluster members are considered to be formed in one star formation event. For young clusters the observed present day mass distribution should be very close to the initial mass function (IMF). Since high-mass stars evolve on timescales much shorter than those of low-mass stars, they will be the first cluster member to leave the main sequence. The presence of WR stars for example can give indications on the cluster age, while low-mass stars, which evolve rather slowly will still remain on the main sequence. The age of the Quintuplet cluster has been estimated to be about 4 Myr (Figer et al. 1999a) from the evolved massive stars in their Wolf-Rayet (WR) phase, i.e. WN and WC stars. The analysis of the WN stars is presented in Chapter 4.2, finding that the evolutionary phases of the stars agree with the assumed cluster age. However, Glass et al. (1990) reported the presence of one red supergiant (RSG) in the cluster. The K-band spectra of the LHO catalog include 62 late-type stars and 85 OB/early-type stars with spectral classification and radial velocities (RVs); they will be the basis for the following analysis.

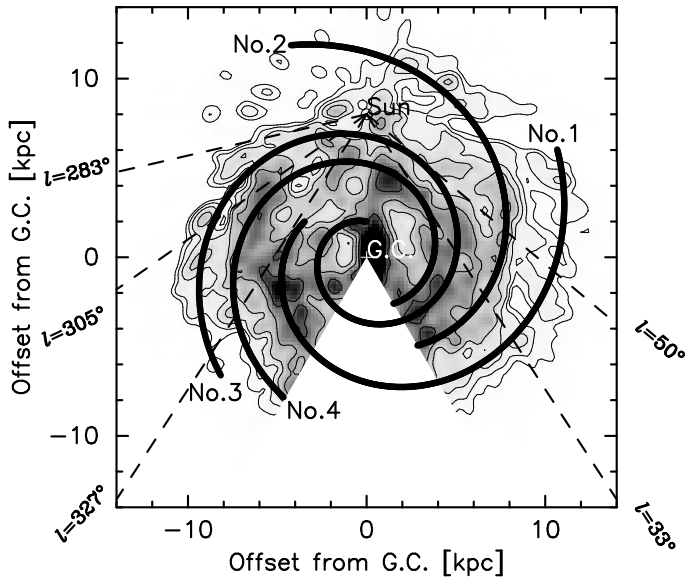

Figure 5.1: Molecular hydrogen column density as tracer of the spiral structure of the Milky Way, from Nakanishi & Sofue (2006, Fig. 14). The schematic view shows the spiral arms Norma (No. 1), Perseus (No. 2), Sagittarius-Carina (No. 3), and Scutum (No. 4).

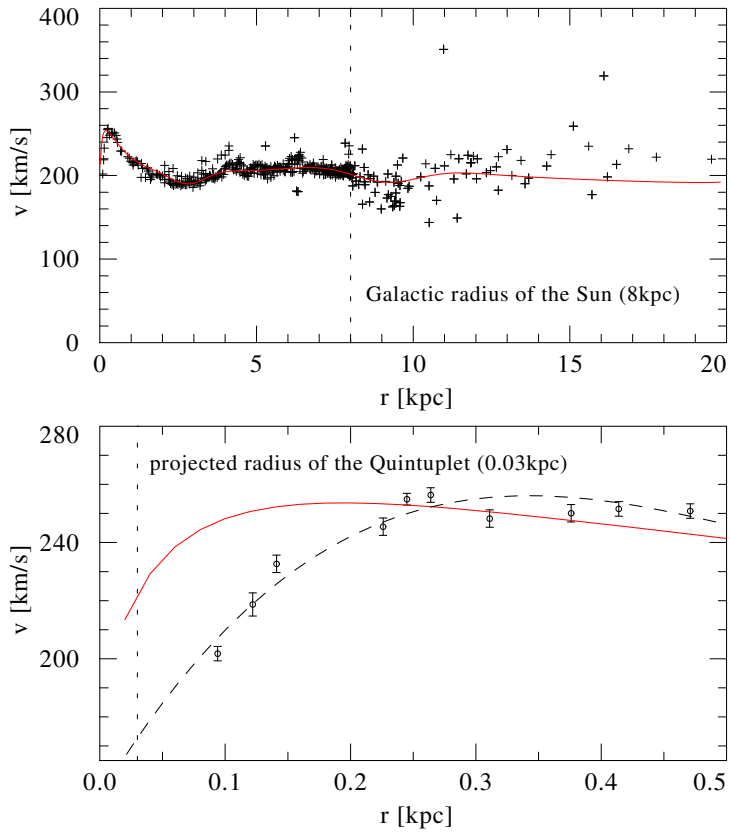

Figure 5.2: Observed Galactic rotation curve compared with the three-component model from Sofue et al. (2009) (upper panel). For the inner part, these authors provide corrected tangent point data derived from H I emission by Burton & Gordon (1978) (lower panel). The model seems to overestimate the bulge component in this inner region, resulting in a velocity of 221 km/s for a Galactocentric radius of 30 pc. A polynomial fit to the data within 1 kpc results in 173 km/s for the same distance.

5.2 Analysis

5.2.1 Velocities

Cluster velocity The Milky Way is rotating differentially and the cluster position should correspond to a specific velocity following the Galactic rotation curve. There are different approaches to derive the Galactic rotation curve: H α (λ 656 nm), forbidden [N II] and [S II] emission are the most prominent features in the visual spectral range to be measured. However, detailed information of visually obscured parts of the Galaxy are derived from CO, H I, and molecular hydrogen (H_2) emission in the infrared. This can be supplemented by observations of SiO, OH, and H_2O maser from gas clouds and circumstellar shells. Thus, the gaseous structure of the Milky Way can be constrained in addition to the observed stellar distribution, defining the Galactic spiral arm structure, see Fig. 5.1.

A homogenized sample of different observations is presented in Sofue et al. (2009) fitted with a model containing three components that contribute to the velocities at different Galactocentric radii. These components are the overall components for regular spiral galaxies: the disk, the bulge, and the halo. The sample and model are publicly available, see Fig. 5.2 (upper

Table 5.1: Comparison of rotational and radial velocities derived for the Quintuplet cluster.

	v [km/s]	reference
rotational velocities		
three-component model	221	Sofue et al. (2009), see Fig. 5.2
polynomial fit to H I tangent point data	173	data – Burton & Gordon (1978), fit – this work
radial velocities		
	127	Pistol star, Figer (1995)
	139	Q 8, Figer (1995)
	135	Q 10, Figer (1995)
cluster average	130	Figer et al. (1999a)
cluster average	113±17	this work

panel). The position of the Sun at 8 kpc is indicated. For the inner 2 pc the observations refer to corrected tangent point data derived from H I emission by Burton & Gordon (1978). Since the inner part of the Galaxy where the Quintuplet cluster is located is of greater interest in this work, a close-up for the innermost 500 pc is shown in Fig. 5.2 (lower panel). It can be seen that the observational data do not cover the innermost region completely but end at about 100 pc. While the three-component model excellently reproduces the overall shape of the rotation curve, it does not fit very well the few innermost observations $\leq$ 200 pc. The model (solid line) would give a rotational velocity of 221 km/s assuming a circular orbit around the Galactic center (GC) with a radius of 30 pc for the Quintuplet. A polynomial fit to the observational data within 1 kpc (dashed line) results in a slightly lower rotational velocity of 173 km/s. It has to be emphasized that a dedicated model is preferred over a polynomial fit for the general purpose of a Galactic rotation curve and the latter is only considered a test for the innermost Galactic region. A comparison of the different derived rotational velocities for the Quintuplet is summarized in Table 5.1.

Under the assumption that the average cluster velocity determined in Sect. 2.2.4 (see also Table 5.1) is the radial component of the rotational velocity projected on the line of sight, the true cluster distance from the Galactic GC can be estimated from geometrical considerations. Motions perpendicular to the Galactic plane are neglected, plain geometry and again circular orbits around the GC are assumed. The rotational velocities listed in Table 5.1 are applied to derive the true cluster distance, which is then taken to recalculate the rotational velocity etc. This iterative scheme converges in a cluster distance range of 49 pc to 64 pc compared to the projected cluster distance of 30 pc (Figer et al. 1999c). For the assumed circular orbits around the GC these new distances result in an orbital period of about 1.6 Ma for the Quintuplet cluster.

Radial velocities The radial velocities RV for the individual stars in the LHO catalog and a cluster radial velocity were derived in Sect. 2.2.4. Additionally, a first approximation for the velocity dispersion of the Quintuplet cluster was determined under the assumption of a virialized cluster, which is of the same order as the error on the above cluster radial velocity (see Table 5.1). On basis of the individual RVs an estimate for the cluster membership of the

stars was given but it has to be kept in mind that the radial velocities can be affected by further line-of-sight effects. A star might have an RV that is by chance in the range determined for cluster membership, although it is spatially not related to the cluster. And RVs can severely be influenced for stars in binary systems. In these cases the periodic variation of the RVs can only be detected from time series of spectra, which are not available for the Quintuplet stars.

The distribution of the radial velocities over the sample of the LHO catalog is shown in Fig. 5.3 and Fig. 5.4 as background histogram overplotted with the distributions for late-type and early-type stars, respectively. The late-type stars seem to be distributed almost homogeneously, with a tiny peak within the 3σ interval that was assumed to indicate cluster membership. A median number of 5 stars per velocity bin was found, which might be considered the mean number of late-type stars along an arbitrary line-of-sight towards the Galactic center region. For a more precise approach control fields around the Quintuplet cluster would need to be observed, to estimate the number of "field stars". Additionally, the conclusions about foreground stars have to be regarded under the aspect of the near-infrared visibilities. The disadvantage of the high visual extinction is overcome, but makes it more difficult to distinguish between foreground and background objects relative to the cluster. As can be seen from Fig. 5.5 no clear distinction by magnitude between bright foreground and faint background objects relative to the cluster is possible, but a general distribution of the K-band magnitudes over the RVs is present. Together with the lack of control fields and the peaked number distribution of late-type and early-type stars within the $3\,\sigma$ interval of the cluster radial velocity, it seems justified for the further analysis to consider these stars as cluster members. This limited sample of stars will thus be referred to as the corrected sample in the following.

5.2.2 Stellar luminosities and the HRD

To study the more general cluster properties it is essential to establish a Hertzsprung-Russell diagram for the Quintuplet cluster. Besides the WN stars, which were analyzed in Sect. 4.2 the late-type stars and early-type stars need to be analyzed. However, it is not possible in the short time available to fit tailored models to all stars. Thus, the effective temperatures for the late-type stars in the corrected sample were taken from the spectral classification, see Sect. 2.2.2, and applied for the bolometric corrections (BC) from Levesque et al. (2005)

$$\mathrm{BC}_K = 5.574 - 0.7589\,(T_{\mathrm{eff}}/1000\mathrm{K})\,. \tag{5.1}$$

The effective temperatures for OB stars were assigned following the spectral type calibration from Martins et al. (2005) and applied for their bolometric corrections

$$\mathrm{BC}_V = 27.58 - 6.80\,\log\,(T_{\mathrm{eff}}/\mathrm{K})\,. \tag{5.2}$$

These BCs are valid only for the visual spectral range as indicated by the index and a correcting term for the K-band BCs is necessary. From a previous model analysis of O stars (see Oskinova et al. 2006) an average $M_V - M_K = -0.98\,\mathrm{mag}$ was found. This sample of O stars contained spectral types O3 to O7 with luminosity classes I to V, therefore the term is considered to be applicable for the correction $\mathrm{BC}_K = \mathrm{BC}_V - (M_V - M_K)$.

Absolute stellar magnitudes M_K were derived from the synthetic K_s in the LHO catalog with the mean cluster extinction $A_K = 3.1 \pm 0.5\,\mathrm{mag}$ (see Sect. 4.3.6) and a cluster distance of 8 kpc (Reid 1993) together with the corresponding bolometric corrections. Again, it has

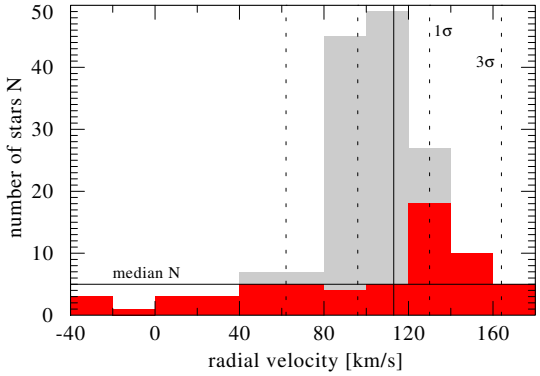

Figure 5.3: Histogram of the stellar RVs in total (gray). Overplotted is the RV distribution of the late-type stars (red). Solid and dashed lines indicate the cluster RV of 113 km s^{-1} and the 1 and 3 σ interval as discussed in Sect. 2.2.4

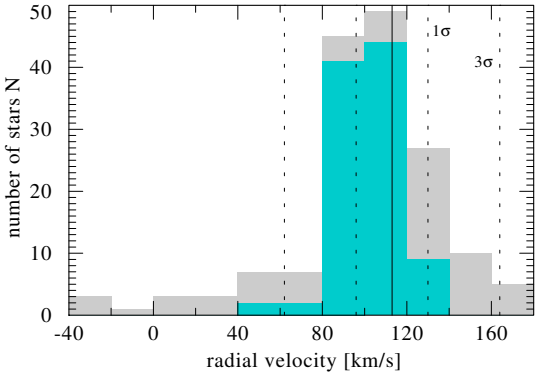

Figure 5.4: Same as Fig. 5.3 but overplotted is the RV distribution of early-type stars. Both distributions peak within the intervals assumed for cluster membership, albeit more pronounced for the early-type stars.

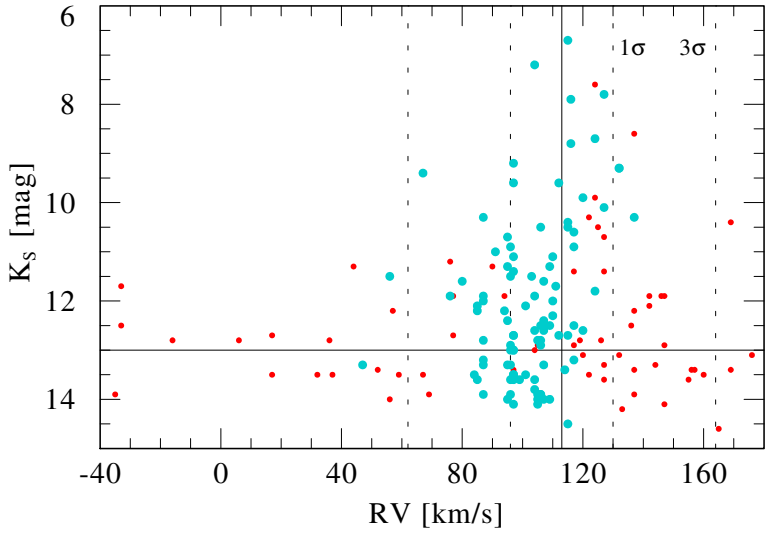

Figure 5.5: Distribution of K_s magnitudes over radial velocities for all stars in the LHO catalog. The photometric completeness at $K_s = 13$ mag is indicated by the horizontal line, while the vertical lines refer to the different RV intervals.

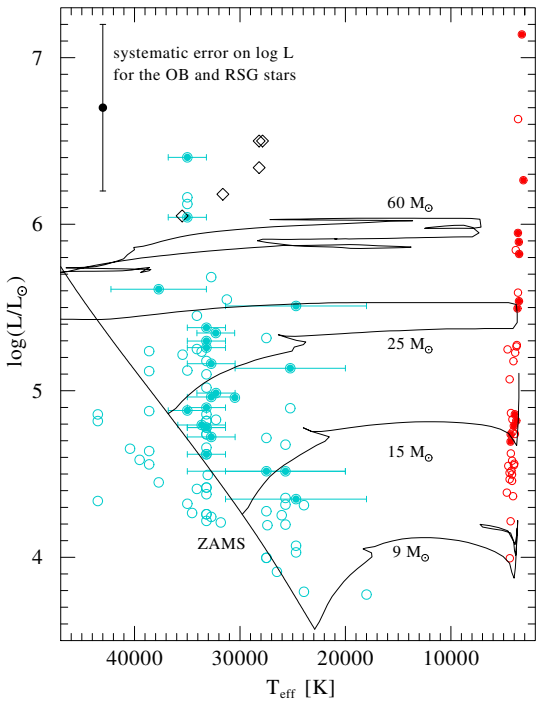

Figure 5.6: HRD of the corrected sample. Blue circles are for the OB stars, red ones for the late-type stars, and open diamonds for the WN stars. The ZAMS and evolutionary models with rotation are shown (Meynet & Maeder 2003b, solid lines).

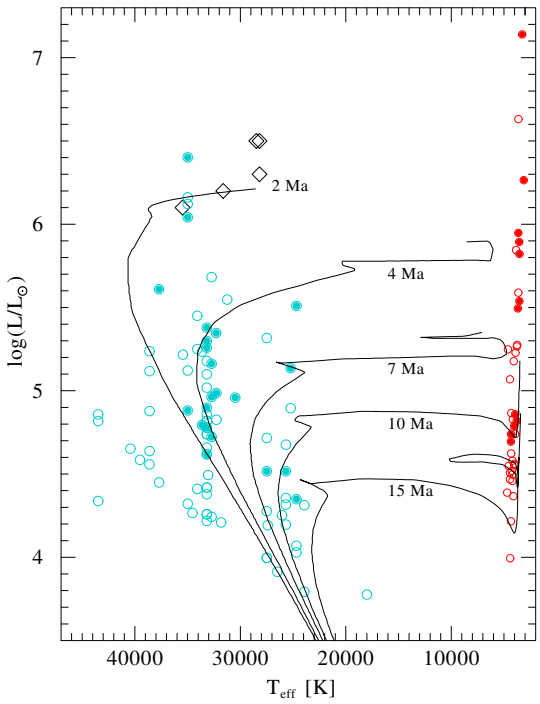

Figure 5.7: Same as Fig 5.6 but with theoretical isochrones for different cluster ages. The isochrones were compiled by Lejeune & Schaerer (2001) on the basis of the stellar evolutionary models by Meynet et al. (1994).

to be emphasized that all stars in the corrected sample are *assumed* to be cluster members. This allows a uniform cluster distance and cluster reddening to be applied for all objects. The absolute magnitudes are transformed then to stellar luminosities

$$\log\left(\frac{L}{L_\odot}\right) = -0.4\,(M_K - \mathrm{BC}_K - M_{\mathrm{bol},\odot})\,, \tag{5.3}$$

with $M_{\mathrm{bol},\odot} = 4.74\,\mathrm{mag}$ for the bolometric luminosity of the Sun. The obtained results are shown in Fig.5.6, blue circles refer to the early-type OB stars and red circles to the late-type stars. The filled symbols refer to stars in the corrected sample which fulfill even stricter conditions concerning cluster membership; they lie within the $1\,\sigma$ interval of the cluster radial velocity, have K_s magnitudes within the photometric completeness limit (see Sect. 2.2.3 or Fig. 5.5), and their RVs are not marked as uncertain in the LHO catalog (noisy spectra), i.e. the restricted sample. The error bars on the temperatures for the late-type stars vanish within the symbol size, and for the OB stars they refer to the spectral classification range as an upper and lower temperature. The systematic error on the luminosity is dominated by the error of the mean cluster extinction.

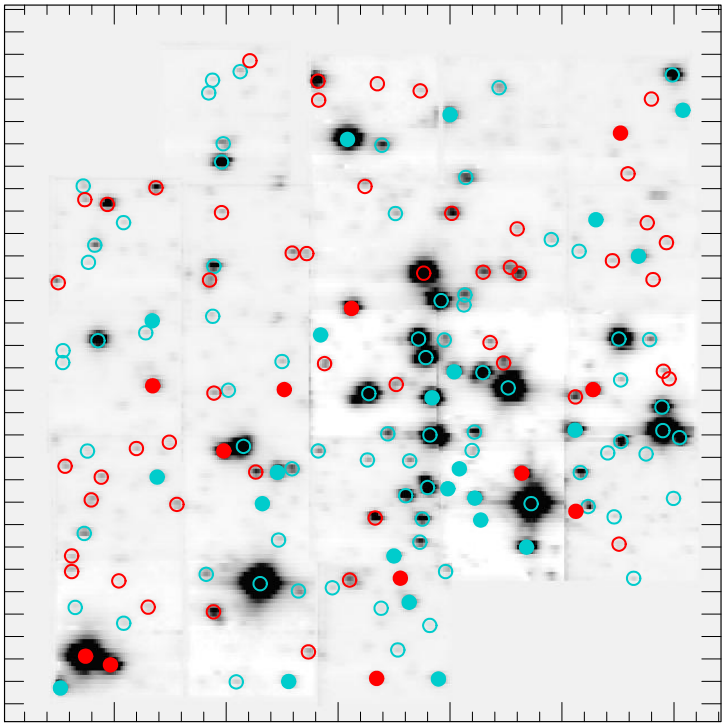

Figure 5.8: Spatial distribution of late-type and early-type stars within the cluster field.

5.3 Discussion

5.3.1 Evolution

As can be clearly seen from Fig 5.6, the different spectral classes form two distinct groups in the HRD. The early-type stars scatter more or less along the zero-age main sequence (ZAMS), while the late-type stars interestingly line up in the low-temperature regime $T_{\rm eff} < 10\,000\,{\rm K}$ but over the same luminosity range as the OB stars. Evolutionary tracks including the effects of rotation (Meynet & Maeder 2003b) for initial masses of 9, 12, 15 and 60 $M_\odot$ show that all stars would be massive stars in the classical definition ($M_{\rm init} > 8\,M_\odot$). Concerning their position in the HRD and the evolutionary tracks, the late-type stars would have to be considered evolved massive stars, i.e. red supergiants (RSG).

The coexistence of RSGs, main sequence OB stars, and WR stars is not expected a priori under the assumption of a coeval evolution of the Quintuplet cluster due to the different life times of these stars. From the *RV*s and the spatial distribution of the stars in the cluster field no separation in subclusters with two distinct populations is found, see Fig. 5.8. However, Hunter et al. (2000) discuss the possibility of an extended star formation event over a few million years, which could explain the simultaneous presence of WR stars and RSGs. In Fig. 5.7 the HRD with isochrones compiled by Lejeune & Schaerer (2001) is shown for different cluster ages of 2, 4, 7, 10, and 15 Ma. The assumed cluster main sequence of OB stars corresponds well with the 4 Ma isochrone, while the RSGs need about 10 Ma to evolve. If this range in age is considered "a few million years" for continuous star formation, the cluster might still be coeval.

Also other Galactic open cluster are known to contain simultaneously evolved early-type stars, such as luminous blue variables (LBVs) and WR stars, and RSGs. Westerlund 1 (Wd 1)

Table 5.2: Number ratios for WR stars based on van der Hucht (2001, 2006). The number of binaries and binary candidates (?) are given in separate columns.

	$N_{\rm WR}$	$N_{\rm WN}$		$N_{\rm WC}$		$N_{\rm WC} : N_{\rm WN}$	$N_{\rm RSG} : N_{\rm WR}$
		all	binary	all	binary		
Quintuplet*	21	8	1?	13	7?	1.6	12:21
Arches	17	17	5?	0	0	0.0	-
Central Parsec	42	18	0	24	10?	1.3	-
Westerlund 1	27	19	3+6?	8	6?	0.4	10:27‡
Milky Way†	63	25	6	38	19	1.5	-

* Numbers from van der Hucht (2006) corrected for the WR stars newly identified in this work: WN9h - LHO 110, WC9d - LHO 76 and LHO 79. The number of RSGs was estimated from the restricted sample of late-type stars.

‡ Four RSGs by Mengel & Tacconi-Garman (2007) and six YHG by Clark et al. (2005b).

† Numbers from van der Hucht (2001) not including the Galactic center regions.

is the most prominent example that shows this mixed stellar population. It hosts four RSGs (Mengel & Tacconi-Garman 2007) and six yellow hypergiants (YHG) (Clark et al. 2005b). Crowther et al. (2006) concluded from an earlier number ratio of $N_{\rm RSG+YHG}/N_{\rm WR}$ = 8:24 a cluster age of 4.5-5 Ma for Wd 1. The revised number of WR stars and RSGs in Wd 1 changes the number ratio only slightly. For the Quintuplet cluster a number of 12 RSG candidates is found from the restricted sample of late-type stars, which results in about the same ratio as in Wd 1 (Table 5.2). This also might indicate that the Quintuplet cluster is older than 4 Ma.

In comparison with other Galactic center clusters, the Quintuplet cluster shows the same number ratio of binary stars to single stars (Table 5.2). Binary candidates from van der Hucht (2001) are listed with a question mark until their status is confirmed. The WC binary candidates show an IR excess in their spectra, which is suspected to arise from circumstellar dust produced in colliding wind binaries. Crowther et al. (2006) discuss six further WN stars in Wd 1 as binary candidates by the detection of low-luminosity hard X-ray emission and the Arches binary candidates are found by Lang et al. (2005) to show variable radio emission. For the Quintuplet, van der Hucht (2006) lists one WN binary candidate, WR 102i, which can well be fitted as single star with the PoWR models. Instead LHO 110 is given as binary candidate due to its unclear status, see Sect. 4.2. Additionally, two further WCd stars are newly identified in the LHO catalog and listed as WC binary candidates.

The Quintuplet cluster also has a similar ratio of $N_{\rm WC}/N_{\rm WN}$ as the Central Parsec cluster (van der Hucht 2006) and the solar neighborhood (van der Hucht 2001). In this respect, the cluster seems not to be too different from other Galactic regions.

5.3.2 Luminosity function and mass function

Further diagnostic tools to study the cluster properties are the purely observational luminosity function (LF) and the initial mass function (IMF) involving some mass–luminosity relation.

The LF was established for the Quintuplet cluster by counting the number of stars per

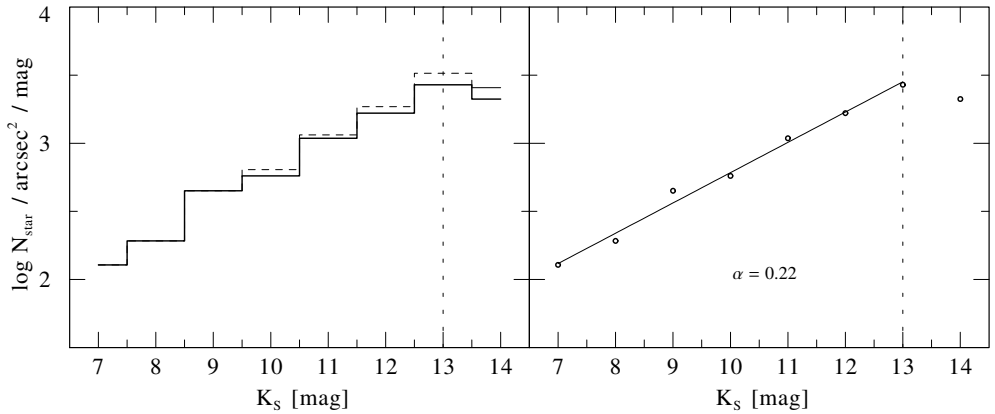

Figure 5.9: Luminosity function of the Quintuplet cluster. The photometric completeness at $K_\mathrm{s} = 13\,\mathrm{mag}$ is indicated by the vertical dashed line. *Left:* Histogram of all stars in the LHO catalog (dashed line) and corrected for foreground stars (solid line). *Right:* Fit to the corrected sample distribution (solid line) with respect the photometric completeness limit (dashed line).

observed field and per magnitude bin. The resulting distribution is shown in Fig. 5.9 for the total cluster sample (dashed line) and the corrected sample (solid line). A power law with an exponent $\alpha = 0.22$ can be fitted to the latter distribution. Figer et al. (1999c) argue that such kind of shallow distribution is expected for young coeval clusters. For example, Harayama et al. (2008) found $\alpha = 0.27$ for the young massive star-forming region NGC 3606.

For a young coeval cluster it also is expected that the stellar population still resembles the initial mass distribution. However, the evolved WR stars (WC subtypes!) and the presence of RSGs imply that the Quintuplet might have had a more complicated star formation and evolution history, as described above. Nevertheless, to obtain a first guess on the initial mass function, the sample of stars will exclude the evolved objects. As can be seen from Fig. 5.7 the early-type OB stars are well located around the isochrone of 4 Ma. Thus, the OB stars are considered to be formed during one almost recent star formation event and will provide the sample in the following. Again, this sample results from the corrected sample of LHO stars of spectral types OB, i.e. all stars outside the $3\,\sigma$ interval of the cluster RV are ignored, and for the even more restricted sample the $1\,\sigma$ interval is applied in addition to the photometric completeness limit and the exclusion of stars with uncertain RVs (noisy spectra).

From the 4 Ma isochrone a mass-luminosity relation is derived and applied to the corrected OB sample stars. Initial masses are determined, yielding the IMF shown in Fig. 5.10. A power law is fitted to the different distributions, which results in a shallow exponent $\Gamma = -0.85 \pm 0.33$ for the restricted OB sample and a steep exponent of -1.65 ± 0.38 for the corrected sample. The canonical Salpeter-IMF would follow $\Gamma = -1.35$ (Salpeter 1955). However, top-heavy IMFs for massive stellar cluster are discussed throughout the Galaxy. For example, Maness et al. (2007) find $\Gamma = -0.85$ for the Central Parsec cluster assuming continuous star formation, while Paumard et al. (2006) favor a star burst. The Arches cluster was analyzed by Stolte et al. (2005) who discuss a flat present-day mass function with $\Gamma = -0.9$ to -1.1, but Portegies Zwart et al. (2002) do not exclude a regular Salpeter-IMF when mass segregation is taken into account. Thus, indications for a top-heavy IMF in the GC are present but the details of star and cluster formation are not yet well understood.

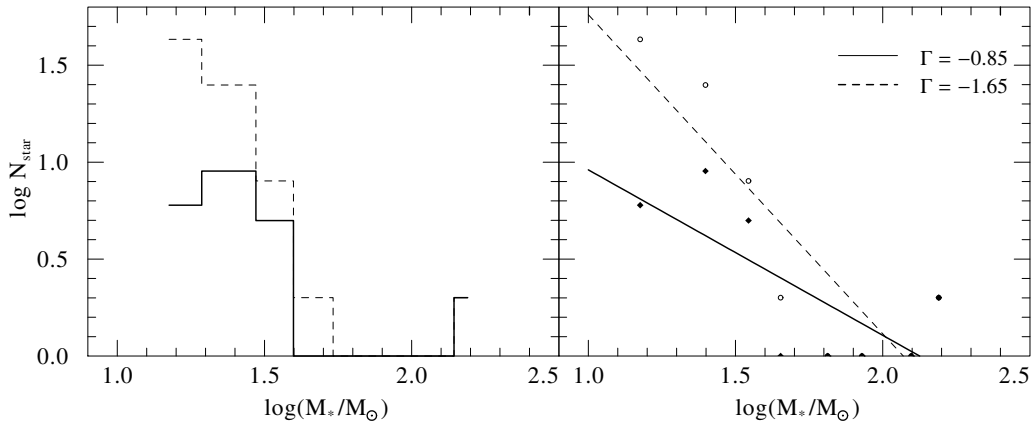

Figure 5.10: Initial mass function of the Quintuplet cluster. *Left:* Histogram of all early-type stars in the corrected sample (dashed line) and the restricted sample (solid line). *Right:* Fits to the two distributions (dashed and solid line).

5.4 Summary

From a model rotation curve of the Milky Way the predicted rotational velocity was compared with the radial velocity derived for the Quintuplet cluster. The difference can be attributed to projection effects resulting in a corrected cluster distance of 49 to 64 pc to the Galactic center.

Stellar temperatures and luminosities were determined for all stars assumed to be cluster members and an HRD was established. Two stellar populations are found, a group of main sequence OB stars and a group of evolved late-type stars. The main sequence stars indicate a cluster age of 4 million years, which would be too young for red supergiants to be observed. The number ratio $N_{\mathrm{RSG}}/N_{\mathrm{WR}}$ of 12:21 requires that the cluster is slightly older. To reconcile this discrepancy one can assume that the star-formation period in the Quintuplet cluster extended over a few million years. Besides, the observed number ratio $N_{\mathrm{WN}}/N_{\mathrm{WC}}$ and the binary fraction are comparable to the rest of the Galaxy.

The luminosity function and initial mass function are derived, the latter does not exclude a top-heavy IMF for the star formation in the Quintuplet cluster. But the details of stars formation and cluster evolution are not yet well constrained.

Chapter 6

Summary and Outlook

At the end of this thesis project it is interesting to look back and see what was accomplished. Besides being tired of writing all night long and sad about this phase being almost finished, there are notions of things not being finalized, of projects that might, should and will follow.

6.1 Summary

The presented thesis describes the observations of the Galactic center Quintuplet cluster, the spectral analysis of the cluster Wolf-Rayet stars to determine their fundamental stellar parameters, and discusses the obtained results in the general context of the cluster. Massive stars passing the Wolf-Rayet phase are characterized by short lifetimes, strong radiation fields, and strong stellar winds by which they give fast feedback to the ambient medium: mechanical energy, ionizing photons, and nuclear processed material. In this way, they are important for the chemical evolution of the universe, since they enrich the interstellar medium with metals, blow circumstellar bubbles and drive shocks in the ISM that might trigger or terminate stars formation processes nearby. These stars are also suspected to represent the first generation of stars after the Big Bang, which re-ionized the universe and enriched it chemically for further generations of stars. This renders it even more important to understand the present-day population of massive stars and their evolution.

The Quintuplet cluster was discovered in one of the first infrared surveys of the Galactic center region. A prominent constellation of five IR-bright stars gave reason to name the cluster the "Quintuplet cluster" (Okuda et al. 1987, 1989). It is located at about 30 pc projected distance to the Galactic Center. A cluster radius of about 1 pc was determined and an age of about 4 million years estimated (Okuda et al. 1990; Figer et al. 1999a).

Observations were obtained with the ESO-VLT integral field instrument SINFONI-SPIFFI and the subsequent data reduction was performed in parts with a self-written pipeline to obtain flux-calibrated spectra of all objects detected in the imaged field of view. First results of the observation were compiled and published in a spectral catalog of 160 flux-calibrated K-band spectra in the range of 1.95 to 2.45 μm, containing 98 early-type and 62 late-type stars (Liermann et al. 2009). About 100 of these stars are cataloged for the first time, including coordinates, spectral classification and derived K_s magnitudes. In addition, radial velocities of the individual stars were derived and employed as indicator for cluster membership. From a model rotation curve of the Milky Way the predicted rotational velocity was compared with the average radial velocity derived for the Quintuplet cluster. The difference is attributed to projection effects resulting in a Galactocentric cluster distance of about 49 to 64 pc for a circular orbit around the Galactic center with an orbital period of 1.6 million years.

Among the early-type stars in the catalog there are 13 Wolf-Rayet stars, 4 of the nitrogen sequence (WN) and 7 of the carbon sequence (WC). The main part of the thesis project was concentrated on the analysis of the WN stars and one further identified emission line star (Of/WN). For the first time, tailored Potsdam Wolf-Rayet (PoWR) models for expanding atmospheres are applied to derive the stellar parameters of these stars from a spectroscopic study. The atomic input data of the PoWR models was extended for this purpose. Further line transitions in the near-infrared spectral range were implemented to enable more detailed model spectra to be calculated. These models were fitted to the observed spectra. Stellar temperatures of 28 000 to 35 000 K are derived, which corresponds to their late spectral subtype (WN9). Also a significant amount of hydrogen of up to $X_\mathrm{H} \sim 0.2$ by mass fraction is still present in their stellar atmospheres. The stars are also found to be very luminous $\log(L/L_\odot) > 6.0$ and show mass-loss rates and wind characteristics typical for radiation-driven winds. These wind parameters also indicate that the WN stars in the Quintuplet

cluster are not metal enriched as generally suspected for the Galactic center. From comparison with evolutionary models (Meynet & Maeder 2003a; Langer et al. 1994), the initial masses were estimated and indicate that the Quintuplet WN stars are descendants from the most massive O stars with $M_{\rm init} > 60 M_\odot$ and their ages correspond to a cluster age of 3-5 million years. This comparison also indicates that these stars are still core-hydrogen burning objects, in contrast to more evolved Wolf-Rayet stars that are expected to be core-helium burning. The results of the spectral analysis of the WN stars are prepared for publication (Liermann et al., submitted).

The analysis of the individual WN stars revealed an average extinction of $A_K = 3.1 \pm 0.5$ mag ($A_V = 27 \pm 4$) towards the Quintuplet cluster. This extinction was applied to derive the stellar luminosities of the remaining early-type and late-type stars in the catalog. With the stellar temperatures assigned from spectral-type–temperature calibration or equivalent width measurements, a Hertzsprung-Russell diagram was established for all presumed cluster members from their radial velocities. Surprisingly, two stellar populations are found, a group of main sequence OB stars and a group of evolved late-type stars, i.e. red supergiants (RSG). The main sequence stars indicate a cluster age of 4 million years, which would be too young for red supergiants to be already present. However, a star formation event lasting for a few million years might explain the Quintuplets' stellar population and the cluster might still be considered coeval. The observed number ratios $N_{\rm RSG}/N_{\rm WR}$ of 12:21, $N_{\rm WN}/N_{\rm WC}$ of 8:13, and the binary fraction are consistent with other Galactic regions.

Under the assumption that at least the main sequence stars have formed in one star formation event the luminosity function and the initial mass function are derived. The latter does not exclude a top-heavy cluster IMF, but also could follow the canonical Salpeter law. However, the unexpected and simultaneous presence of red supergiants and Wolf-Rayet stars in the cluster point out that the details of stars formation and cluster evolution are not yet well constrained for the Quintuplet cluster.

6.2 Outlook

Some results of this thesis might be considered in the overall framework that was sketched at the beginning, ranging from high-mass star formation to cluster evolution. The following comments certainly need further study and consideration, and are meant as a shy glance beyond the own nose.

Subsequent projects The careful reader will have noticed that the Wolf-Rayet stars of the carbon sequence were quite ignored in the preceeding chapters. This was not out of acting in bad faith. PoWR models were already tested to fit the WC stars, but two facts render it more difficult to proceed than in the case of the WN stars. First, out of 13 WC stars two are confirmed binaries (Tuthill et al. 2006) and further 6 binary candidates are identified based on the infrared excess in their spectra which is thought to arise from circumstellar dust produced in colliding wind binaries. Second, this dust dilutes the observed spectral features. Thus, the spectra of the WC stars have to be prepared before they can be an fitted with the PoWR models. The dust excess can either be removed by assuming a black body of adequate temperature that will be subtracted from the observed flux-calibrated spectrum, or by applying dedicated models, e.g. DUSTY (Ivezić & Elitzur 1997). The next steps would be to examine the dust-free spectra for features of the binary companion, which would have to be subtracted by a template spectrum, or to estimate the flux contribution of the companion.

Finally the decomposed WC spectrum can be analyzed with the PoWR models.

These models were also applied for O stars in the past (Oskinova et al. 2006). A recent upgrade implements the Stark effect to the formal integral of the emergent synthetic spectrum, which should allow an even more dedicated analysis of the O stars to be performed.

Star formation in the Galactic center It is observed for other galaxies of similar spiral structure as the Milky Way that star formation can be triggered in a ring around the central region. The trigger mechanism is explained by perturbation of the galaxy potential, which might be caused by the presence of a satellite galaxy and/or the presence of a bar in the central region. The Milky Way was long assumed to be a regular spiral galaxy. First indications for the presence of a bar discussed by de Vaucouleurs (1964) are now widely accepted and constrained by a variety of further observations (Blitz et al. 1993; Kuijken 1996; Weiner & Sellwood 1999).

The density wave theory indicates resonance points in the potential of bared spiral galaxies, known as the inner and outer Lindblad resonance , ILR and OLR respectively. Following Stark et al. (2004) the ILR of the Milky Way is located at approximately 450 pc from the Galactic center with stable orbits that allow for gas to be accumulated at these points. Thus, a gaseous ring can be build via accretion and transport of gas into the central regions. The material can be supplied by the cannibalic disruption of a satellite galaxy, which would result in the accretion of about 100-1000 $M_\odot$ per year onto the Milky Way. Another way with much lower accretion rates is to retain matter from evolved bulge stars and interstellar (neutral) gas with about 0.2-1.2 $M_\odot$ per year (P. Richter priv. communication). However, the gaseous ring itself is not stable. Variable accretion rates are considered one contributor to the ring instability, but the major impact is assumed to result from the number density of the gas. The gas is expected to collapse into self-gravitating giant molecular clouds when the critical density $n_{\rm crit} \geq 10^{3.5}\,{\rm cm}^{-1}$ is exceeded. The fragmentation of the ring into clouds leads to the release of those clouds from the ILR orbits, usually directed inwards to the Galactic center by dynamical friction. On their way the clouds might get disrupted by tidal forces or survive and might undergo star formation. The ILR can now accumulate fresh material into a gaseous ring until the critical density is reached and again fragmentation brings further molecular clouds to the Galactic center. The period of this process depends strongly on the accretion rate, ranging from a few million years (accretion of a satellite galaxy) to some 10^9 years (accretion from the intergalactic medium).

From observations not only the presence of a gaseous ring around the ILR is know, but also giant molecular clouds are found within ca. 100 pc distance of the Galactic center. For example the Sgr B1, Sgr B2, Sgr C and Sgr D complexes with several associated H II regions are detected in thermal radio emission (Lang et al. 2008), in X-ray emission (Koyama et al. 2007) and further maser and molecular line emission (Law & Yusef-Zadeh 2005). Tsuboi et al. (1999) measured the CS molecular line flux and estimated the mass of the Sgr B complex to about 4 to $10{\times}10^6\,M_\odot$, which could certainly provide enough material for the formation of a massive or supermassive stellar cluster. Thus, the existence of the Arches and Quintuplet cluster in the innermost part of the Milky Way might be explained in principle.

To confirm the general scheme of the periodic release of molecular clouds from the circum nuclear ring to the Galactic center, the structure of the innermost region of the Milky Way has to be studied. Models of the Galactic rotation curve need to be confirmed by further observation; tangential point measurements can be considered for the clouds within 100 pc Galactocentric radius. Other observations can constrain the gaseous and stellar structure of the Galactic bar. Additionally, the accretion rate from halo material onto the Milky Way and its transport to the center needs to be understood. In this aspect, the interplay of processes

releasing material into the Galactic halo (disk wind, Galactic fountains), the intermediate and high-velocity clouds in the halo returning material to the disk, and the contribution of the Magellanic stream play a crucial role in the dynamical evolution of the Milky Way. Radio emission from the gaseous components as well as absorption features in the spectra of background sources could be studied to reveal their chemical composition and possible deposition processes on the Galaxy.

Formation of the Quintuplet cluster stars So, there is a way to bring giant molecular clouds in the innermost region around the Galactic center. But the question remains how the star formation in these clouds is triggered and the Quintuplet stars itself are formed. As already indicated in Chapter 5, the cluster population shows a dichotomy that might either be understood assuming two subsequent burst-like events or by an extended star formation.

Sofue (1999) found shell-like structures underneath the prominent radio arc emission detected by Yusef-Zadeh & Morris (1987), which form almost concentric circles with radii of 5 to 10 pc around the Pistol-Sickle region. This thermal emission is considered to arise from ionized interstellar gas, which might either originate from a supernova explosion or the combined stellar winds from massive stars. The shells might also be attributed to a previous nebula of similar kind as the present Pistol nebula. Since the most massive stars in the cluster are expected to already have exploded as supernovae this would certainly have influenced star formation processes and cluster dynamics. From Lang et al. (2005) three radio sources, QR 1, QR 2, and QR 3, are known for which no stellar counterparts were found in the near-IR. The authors discuss the possibility that these sources are ultracompact H II regions in which star formation is still going on. Is there a supply with new-formed stars migrating to the cluster?

The analysis of dynamical processes in the cluster region might start with precise radial-velocity measurements to distinguish the true cluster members from non-members. In the following, different cluster evolutionary scenarios can be tested by comparison with numerical simulations, which will help to constrain the initial mass function better, test for the resistance against tidal disruption and the extended versus burst-like star formation.

High-mass star formation Not only the formation of massive clusters in the Galactic center is not yet well understood, but also many details in the process of high-mass star formation (HMSF) are unknown.

In general, stars are formed of rather cold molecular clouds of temperatures about 10 K, and stars are expected to form in clusters. The process starts with an almost spherical symmetric collapse of a self-gravitating molecular cloud. From angular momentum conservation the formation of an accretion disk can be expected to feed the protostellar object with further material. This scenario applies for low-mass as well as for high-mass stars and the question arises, if HMSF is (just) a scaled up version of low-mass star formation. But in high-mass protostellar cores the temperature, radiation pressure and ionizing flux will increase very fast and will counteract the further accretion process. The expected limit for initial masses of massive protostars formed in this way, ranges from 10 to 40 $M_\odot$ from hydrodynamic calculations (Yorke & Sonnhalter 2002). So far, protostellar equivalents of spectral types up to B0 star can be explained by the accretion disk scheme. How to form high-mass O stars that are progenitors to WR stars?

It is discussed how outflow mechanisms, such as disk winds and jets, influence the accretion process and might help to build even more massive protostars. Alternatively, the coalescence of low-mass protostellar cores is considered for the formation of massive stars (Zinnecker & Yorke 2007). Interestingly, this scenario brings binary effects on the agenda, which have been ignored

completely so far. The most massive stars found at present are the components of binary systems, e. g. NGC 3603-A1 with $116 + 89\,M_{\odot}$ (Schnurr et al. 2008).

Unfortunately, high-mass stars form at larger distances compared to known low-mass star forming regions, which reduces the sample of observable targets, and the involved timescales are so very short, that high-mass protostars enter the main sequence phase while still deeply embedded in their natal clouds. But molecular emission lines that trace star formation, accretion and outflows can be studied in the infrared spectral range. Thus it should be possible to determine accretion rates, outflow characteristics, as well as the influence of dust on the star formation. Hopefully, many details will be unveiled from these studies of star forming regions as have been discovered in the Galactic center ...

Appendix A

Constants etc.

Table A.1: Constants

Sun	
Mass	$M_\odot = 1.99 \cdot 10^{30}\,\mathrm{kg} = 1.99 \cdot 10^{33}\,\mathrm{g}$
Radius	$R_\odot = 6.96 \cdot 10^{8}\,\mathrm{m}$
Surface Temperature	$T_\odot = 5800\,\mathrm{K}$
Luminosity	$L_\odot = 3.85 \cdot 10^{26}\,\mathrm{W} = 3.85 \cdot 10^{33}\,\mathrm{erg/s}$
Gravitational acceleration	$g_\odot = 274\ \mathrm{m\,s^{-2}}$
mean density	$\rho_\odot = 1.41\ \mathrm{g\,cm^{-3}}$
Mass-loss rate (solar wind)	$\dot{M} \sim 10^{-14}\,M_\odot/\mathrm{a}$
Distance Sun–Earth	$1\ \mathrm{AU} = 149.6 \cdot 10^{9}\,\mathrm{m}$
Milky Way	
Mass	$M \approx 2.2 \cdot 10^{11}\,M_\odot$
Mass of central black hole	$M \approx 3 \cdot 10^{6}\,M_\odot$
Number of stars (ca.)	$N \approx 2 \cdot 10^{11}$
Disk diameter	$D \approx 30\,000\,\mathrm{pc} \approx 98\,000\,\mathrm{ly}$
Disk height	$H \approx 5\,000\,\mathrm{pc} \approx 16\,000\,\mathrm{ly}$
Rotational velocity of the Sun	$V_\odot \approx 220\,\mathrm{km/s}$
Distance of the Sun to the Galactic center	$R = 8\,000\,\mathrm{pc} \approx 26\,000\,\mathrm{ly}$
Orbital period of the Sun around the Galactic center	$P \approx 220 \cdot 10^{6}\,\mathrm{a}$
Lightyear	$1\ \mathrm{ly} = 9.461 \cdot 10^{15}\,\mathrm{m}$
Parsec	$1\ \mathrm{pc} = 3.086 \cdot 10^{16}\,\mathrm{m}$
Speed of Light	$c = 2.99792\ \cdot 10^{8}\ \mathrm{m\,s^{-1}}$
Gravitational constant	$G = 6.67 \cdot 10^{-11}\ \mathrm{m^3\,kg^{-1}\,s^{-2}}$
Stefan-Boltzmann constant	$\sigma = 5.67 \cdot 10^{-8}\ \mathrm{W\,m^{-2}\,K^{-4}}$
Planck's constant	$h = 6.626\ \cdot 10^{-34}\ \mathrm{J\,s}$

Table A.2: Spectral range

Filter	wavelength range
Gamma rays	$< 0.01\,\mathrm{nm}$
X-rays	0.01 to 20 nm
Ultraviolet (UV)	20 to 400 nm
Visible light (VIS, opt.)	400 to 700 nm
Infrared	0.7 to 300 μm
near-IR	*0.7 to 5 μm*
mid-IR	*5 to 30 μm*
far-IR	*30 to 300 μm*
Radio	$> 0.3\,\mathrm{mm}$

Table A.3: Filter systems

Filter	$\lambda_{\mathrm{center}}$ [μm]	Filter	$\lambda_{\mathrm{center}}$ [μm]	Filter	$\lambda_{\mathrm{center}}$ [μm]
Johnson[1]		*Smith*[2]		*2MASS*[3]	
U	0.36	u	0.37		
B	0.44	b	0.43		
V	0.55	v	0.52		
R	0.70				
I	0.90				
J	1.25			J	1.25
				H	1.65
K	2.22			K_s	2.16

[1] Scheffler & Elsasser (1990) [2] Smith (1968) [3] Skrutskie et al. (2006)

Table A.4: ESO-VLT SINFONI-SPIFFI filter gratings

Filter	$\lambda_{\mathrm{center}}$ [μm]	wavelength range [μm]	Spectral resolution with 250 mas platescale
J	1.25	1.10-1.40	1870
H	1.65	1.45-1.85	2920
K	2.20	1.95-2.45	4490
H+K	1.95	1.45-2.45	1640

from the SINFONI User Manual P84

Appendix B

Spectral catalog

The Catalog comprises the Table B.1 and the K-band spectra (1.95 – 2.45 μm) of 160 stars in the field of the Quintuplet cluster, 98 stars are of early spectral type (O, B and WR), and 62 of late type (K and M).

Table B.1 lists all stars in the observed field of the Quintuplet cluster with arunning number (LHO number - column 1), the right ascension and declination (columns 2 and 3), synthetic K_s magnitude (column 4), spectral classification (column 5), and radial velocities (column 6). Cross-references for identification of previously known stars are given in column 7.

The "LHO" numbers in the spectral atlas refers to Table B.1. The spectra are flux-calibrated, and binned in wavelength over 4 Å. The wavelength scale refers to the local standard of rest. A few spectra are dominated by dust emission.

B.1 Catalog table

Explanations to the catalog table.
List of SIMBAD identifier and reference:

GCS – Kobayashi et al. (1983) Q → GMM catalog – Glass et al. (1990) [NWS90] – Nagata et al. (1990) MGM – Moneti et al. (1992, 1994) [NHS93] – Nagata et al. (1993) qF – Figer et al. (1999a) [FMG99] – Figer et al. (1999b) [GMC99] – Glass et al. (1999) QR – Lang et al. (1999, 2003, 2005, LFG99) [GSL2002] – Giveon et al. (2002) QX – Law & Yusef-Zadeh (2004, LY2004) WR – van der Hucht (2006)

Spectral classification:

OB stars – Hanson et al. (1996, 2005) and Morris et al. (1996): using H I 2.1661 μm Br γ, He I 2.0587 μm, 2.1127/37 μm, 2.1499 μm, 2.1623 μm, He II 2.1891 μm, C IV triplet around 2.0796 μm, N III/C III 2.1155 μm

WR stars – Crowther et al. (2006): applying line ratio C IV (2.079)/C III (2.108) for WC and He II (2.189)/Br γ (2.166) for WN stars

KM giant stars – Wallace & Hinkle (1997); Kleinmann & Hall (1986); Goorvitch (1994): ^{12}CO and ^{13}CO bands, subclasses following González-Fernández et al. (2008), see text Sect. 2.2.2

Magnitudes:

Synthetic K_s magnitudes from our calibrated spectra, see Sect. 2.2.3 for details.

Radial velocity and Cluster membership:

RV measured with the position of the Br γ line for early-type stars and CO (2-0) band head for late-type stars. Uncertain measurements are marked with ":", foreground objects are indicated by "f", see Sect. 2.2.4.

Table B.1: Catalog of Quintuplet stars

LHO No.	R.A. $17^h\ 46^m$ [s]	Dec. $-28^\circ\ 49'$ [″]	K_s [mag]	Spectral type	RV [km/s]	Comments
1	16.70	51.4	10.9	O3-8 I fe	117	[FMG99] 8 em. line star
2	15.95	51.3	13.2	O7.5-B2 I-II e	117	
3	15.73	51.3	12.5	O6-8 I f	117	
4	15.37	51.0	13.0	M1 II	104	
5	15.11	51.0	12.6	O6.5-9 I f:	104	
6	16.49	50.3	9.9	M7 I	124	
7	16.59	49.8	7.6	M6 I	124	**Q 7**, qF 192, NSV 23780, MGM 5-7
8	15.66	49.4	12.8	K2 I	-16f	
9	15.28	49.3	13.6	O4-6 I f:	99	
10	15.15	47.9	14.0	O7-9 I f	109	
11	16.42	47.9	13.4	O3-7 I-II e	114	
12	16.05	47.2	11.3	M1 I	44f	[GMC99] D 3605
13	16.64	47.0	13.5	O6-B2 I	84:	
14	16.33	47.0	13.3	K3 II	144	
15	15.35	46.9	13.8	O4-7 I f	104	
16	15.24	46.5	11.9	O8.5-9.7 I ab: f:	104	qF 197?
17	15.69	46.0	12.2	O3-7 I-II f:	94	
18	15.56	45.7	13.6	O7-8 I f	104	
19	15.85	45.6	7.2	WC8/9d +OB	104	**Q 3**, WR 102ha, qF 211, GCS 4 MGM 5-3, QX 3, [GSL2002] 66 [NHS93] 26, "pinwheel" star
20	16.45	45.5	13.5	K5 II	160	
21	15.49	45.3	11.9	K4 I	94	
22	15.27	45.1	12.8	K2 I	119	
23	14.27	45.3	13.6	O3-6 I-II f	85	
24	16.08	45.1	12.4	O7-9 I f: e	95	
25	16.65	44.9	13.1	M0 II	120	
26	15.08	44.8	13.3	O5-B0 I f:	95	
27	16.65	44.0	13.9	K1 II	-35:f	
28	15.28	44.0	12.3	O7-9 I e	110	
29	14.72	43.5	9.9	O9-B2 I f: e	120	
30	14.33	43.3	13.6	K5 II	155:	
31	15.17	43.2	12.1	O9-B1 I f:	85	
32	15.77	43.1	13.3	B1.5-3 I f:	47:f	
33	16.60	42.7	12.8	O9-B3 I-II f	87	
34	15.16	41.9	11.3	WC8	95:	WR 102g, qF 235S
35	14.91	41.9	12.8	O9-B2 I e:	105	
36	15.36	41.8	11.3	K0? I	90	USNO-B1.000611-0602187? (Monet et al. 2003)
37	14.35	41.7	14.1	O9-B3 I-II	105:	
38	14.51	41.4	12.9	K2 II	105	
39	14.46	41.1	12.2	O7-B1 I f:	85:	[GMC99] D 3606
40	16.20	41.0	13.5	M1 II	37f	
41	15.84	41.0	12.5	O9-B1 I f	107	

Table B.1: Continued.

LHO No.	R.A. $17^h\ 46^m$ [s]	Dec. $-28^\circ\ 49'$ [″]	K_s [mag]	Spectral type	RV [km/s]	Comments
42	14.70	41.0	6.7	WC9d + OB	115	**Q 2**, WR 102dc, qF 231, QR 7 GCS 3-2, MGM 5-1, QX 5, [NHS93] 24, "pinwheel" star
43	16.57	40.8	13.1	K0 I	132	
44	14.94	40.6	11.1	O7-9 I f:	110	
45	14.10	40.7	14.0	O7-B1 I	105	
46	15.23	40.5	10.7	O7-B1 I f:	95	MGM 5-11b?
47	15.14	40.0	10.4	WC8	115	**Q 11**, WR 102f, qF 235N, [NWS90] G, MGM 5-11a, [FMG99] 2, binary? (van der Hucht 2006)
48	15.05	40.1	12.0	O7.5-9.5 I f:	110	
49	16.52	39.4	13.4	K0? I	157	
50	16.29	39.4	12.7	O7-B1 I f	97	QX 4?
51	15.78	39.2	11.4	O7-9 I f	97	
52	15.87	39.1	11.9	M0 I	147	[GMC99] D 334
53	14.74	39.2	10.5	M3 I	125	
54	14.49	39.2	11.6	O7-9 I-II f:	80:	
55	15.72	38.9	12.0	O7-9 I f	87	
56	15.00	38.9	12.6	O7-9 I f:	120	
57	16.68	38.8	13.3	K1 I	127	
58	15.22	38.5	12.9	O9-B1 I-II p:	96:	
59	15.39	38.5	13.3	O9-B1 I	96:	
60	14.21	38.1	13.0	O9-B1 I f:	96:	
61	14.38	38.0	13.6	O7-9 I f:	96:	
62	16.58	37.9	14.0	O7-B1 I-II f	107	
63	16.00	37.9	10.3	M2 I	122	
64	15.60	37.9	12.9	O7-9 I f:	106:	
65	14.95	37.9	12.8	O3-7 I eq:	106:	
66	16.38	37.8	13.6	K3 II	127	
67	15.92	37.6	9.6	WN9	112	**Q 8**, WR 102hb, MGM 5-8, qF 240
68	16.24	37.4	14.1	K2 II	147	
69	14.32	37.4	11.5	O6-9.7 I f:	96:	
70	14.07	37.1	11.0	O7-8 I f	91	
71	15.13	37.0	8.8	WN9	116	**Q 10**, qF 241, WR 102ea, QR 5 MGM 5-10, [NWS90] F,
72	15.31	36.9	11.9	O4-6 I eq:	76	
73	14.94	36.8	11.7	O6.5-7 I f:	111:	
74	14.51	36.7	10.9	O9.5-B1 I ab: f	96	QX 1, qF 242?, [GMC99] D 309
75	14.14	36.7	7.9	WC9:d	116:	**Q 1**, WR 102da, qF 243,MGM 5-1, GCS 3-4, narrow & weak lines
76	14.15	35.4	10.3	WC9d	137:	NEW!!!
77	15.12	34.8	9.6	O6-8 I f eq	97	**Q 12**, qF 278, MGM 5-12, [NWS90] E
78	14.51	34.8	11.9	M1 I	142	qF 252?

Table B.1: Continued.

LHO No.	R.A. $17^h\ 46^m$ [s]	Dec. $-28^\circ\ 49'$ [″]	K_s [mag]	Spectral type	RV [km/s]	Comments
79	15.39	34.6	9.3	WC9d	132	**Q 6**, qF 250, MGM 5-6, [NWS90] B, re-classified
80	16.05	34.6	12.9	K4 I-II	147	
81	15.99	34.4	13.2	O3-4 II/III: f	87:	
82	15.75	34.3	12.9	K5 II	117	
83	14.44	34.4	11.4	M2 I	117	qF 252?
84	14.80	34.2	7.8	WC9d	127:	**Q 4**, WR 102dd, qF 251 GCS 3-1, MGM 5-4
85	16.31	34.1	11.4	M3 I	127	
86	15.27	34.0	12.2	K0? I	137:	
87	14.11	33.7	13.4	K4 II	52f	
88	14.32	33.8	13.3	O3-4 III f	107:	
89	15.03	33.3	11.1	O7.5-8.5 I f	97	QX 2?
90	14.91	33.4	10.3	O7-9.5 I f e:	87	[GSL2002] 63?, GCS 3I H II region?
91	14.14	33.3	13.5	K5 II	67	
92	16.69	32.8	13.9	O8-9.7 I	87	
93	15.58	32.8	12.5	K3 I	-33f	
94	15.76	32.7	13.3	O7-B1 I f:	87	
95	14.82	32.8	11.9	K1 I	77	[GSL2002] 63?, GCS 3I H II region?
96	15.15	32.5	9.3	O6-8 I f e	132	MGM 5-13b?
97	16.69	32.1	14.1	O7-B2 I-II	97:	
98	14.87	31.6	12.7	K4 I	77	
99	16.54	31.5	10.1	WN9	127	WR 102i, qF 256, [GMC99] D 215
100	15.18	31.4	9.4	O6-8 I f e	67	**Q 13**, qF 257, MGM 5-13a, [NWS90] D, QR 6
101	15.07	31.5	11.9	O6-8 I f:e:	87	
102	14.33	31.4	9.2	WC9:d	97	**Q 9**, WR 102db, qF 258, MGM 5-9 GCS 3-3, narrow & weak lines
103	14.20	31.4	12.7	O7-9 I f	97:	
104	16.34	31.1	13.6	O9-B2 I-II f:	97	
105	15.60	31.2	12.6	O7-9 I f:	107	
106	16.31	30.4	12.7	O7-9.5 I	112	
107	16.05	30.1	13.9	O7-9 I f:	106:	
108	15.46	29.6	10.7	M3 I	127	qF 269, [GMC99] D 322, [NWS90] A
109	14.99	29.7	13.0	O7-9 I f:	97:	
110	15.09	29.4	10.6	O6-8 I f (Of/WN?)	117	**Q 15**, qF 270S, MGM 5-15, QR 4, [NWS90] C
111	14.99	29.1	12.4	O8-9 I f:	107:	
112	16.72	28.4	12.8	K4 I-II	6f	
113	16.07	28.2	12.5	K2 I	136	
114	14.19	28.2	13.9	K4 II	137	
115	15.16	27.8	8.6	M2 I	137	**Q 5**, qF 270N, V 4646 Sgr, MGM 5-5
116	14.76	27.9	12.2	M1 I-II	57f	
117	14.91	27.8	12.1	K0? I	142:	

Table B.1: Continued.

LHO No.	R.A. $17^h\ 46^m$ [s]	Dec. $-28^\circ\ 49'$ [″]	K_s [mag]	Spectral type	RV [km/s]	Comments
118	16.05	27.4	11.5	O6-9 I f:	56f	
119	14.80	27.5	12.7	K0? I	17:f	
120	16.59	27.2	13.9	O5-9 I-II f:	106:	
121	14.36	27.1	13.4	K1 I	97	
122	14.25	26.9	11.6	O7-9.7 I e	107	
123	15.72	26.7	12.8	K1 I	36f	
124	15.66	26.8	13.5	K0? I	32:f	
125	14.50	26.6	13.5	O7-9 I-II	97:	
126	16.56	26.2	12.5	O7-9 I f:	106:	
127	14.13	26.1	13.5	K1 II	97:	
128	14.62	25.9	13.5	O3-5 I	97:	
129	14.77	25.3	13.4	K3 II	137	
130	16.44	24.9	13.9	O7.5-9 I-II e:	96:	
131	14.22	24.9	13.5	K2 II	17f	
132	14.43	24.7	13.0	O7-9 I-II f:	97	
133	16.02	24.3	13.4	K3 II	156:	
134	15.28	24.4	13.5	O9-B2 I f:	97:	
135	15.05	24.4	11.7	K4 I	-33f	
136	16.51	23.9	11.2	M2 I	76	
137	16.60	23.6	13.1	K2 I	176	
138	16.30	22.9	11.9	M1 I	146	
139	16.61	22.8	13.5	O7-9 I f:	101:	
140	15.41	22.8	14.2	K3 II	133:	
141	14.99	22.3	11.5	O9.7-B1 I	103:	
142	14.30	22.1	13.5	K3 II	122	
143	16.02	21.4	10.5	O7-B0 I	115:	qF 301, [GMC99] D 271
144	15.34	20.4	11.8	O7-9 I	124:	
145	16.01	20.3	12.7	O7-9 I	115:	
146	15.49	20.1	8.7	O6-8 I f:	124	**Q 14**, qF 307A, MGM 5-14
147	14.27	19.96	12.8	M0 II	126	
148	15.05	18.9	11.3	O7-9 I	109	
149	14.00	18.6	12.1	O7-9.7 I	101	
150	15.61	18.1	13.4	K1 I	169:	
151	14.14	17.99	14.0	K0? II	56f	
152	16.08	17.6	14.0	O6.5-8 I-II f	95	
153	15.18	17.5	13.5	K4 II	59f	
154	14.85	17.3	12.5	O7-9 I	109:	
155	15.36	17.1	13.9	K2 II	69:	
156	15.61	16.9	10.4	M0 I	169	[GMC99] D 307
157	16.06	16.9	14.5	O3-4 II/III:	115	
158	14.05	16.6	10.5	WN9	106	WR 102d, QR 8, qF 320 [GMC99] D278?
159	15.94	16.4	13.9	O7-9 I	105	
160	15.90	15.8	14.6	K1 II	165	

B.2 Spectral atlas

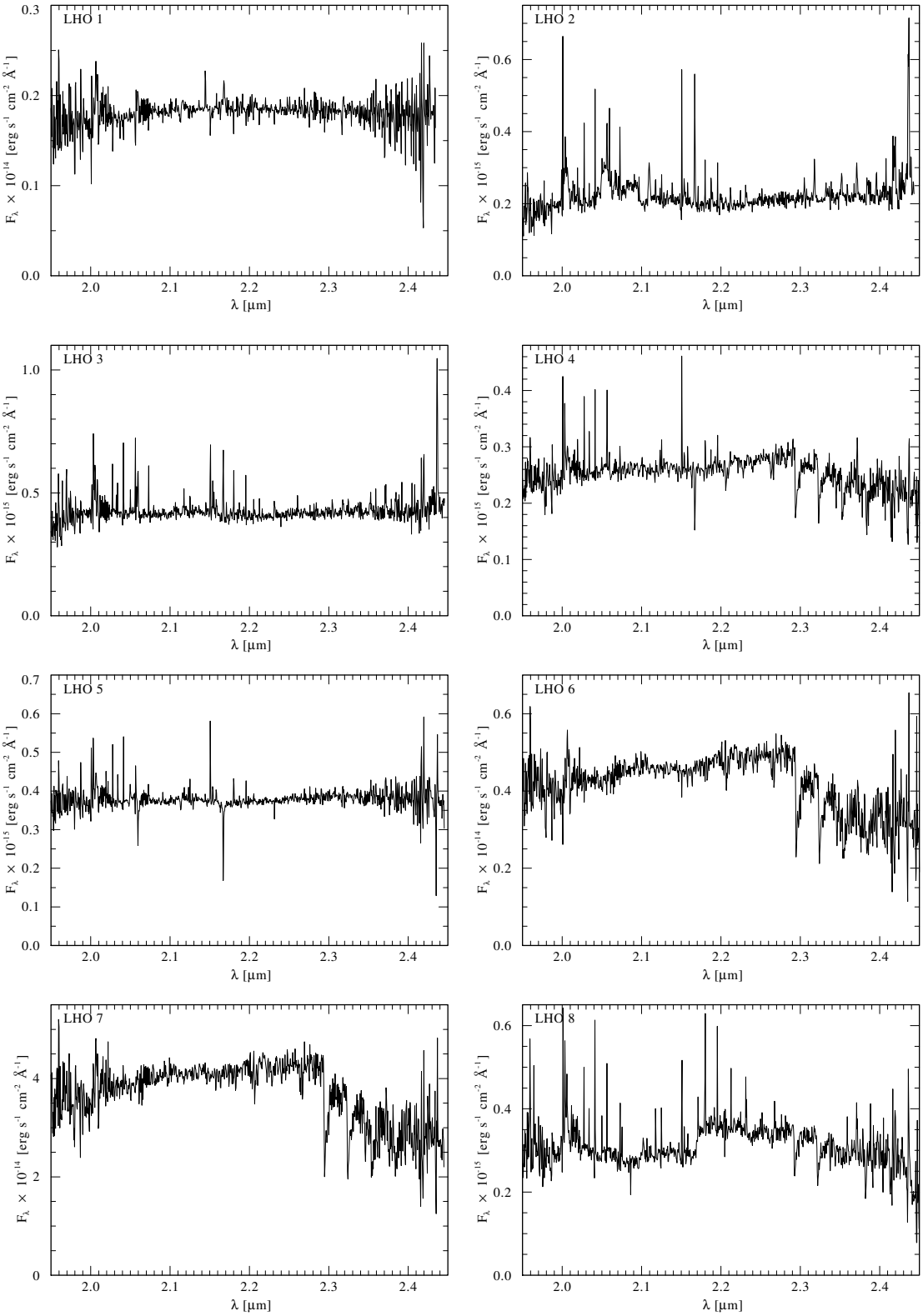

Figure B.1: Spectral atlas, spectra are rebinned with 4 Å.

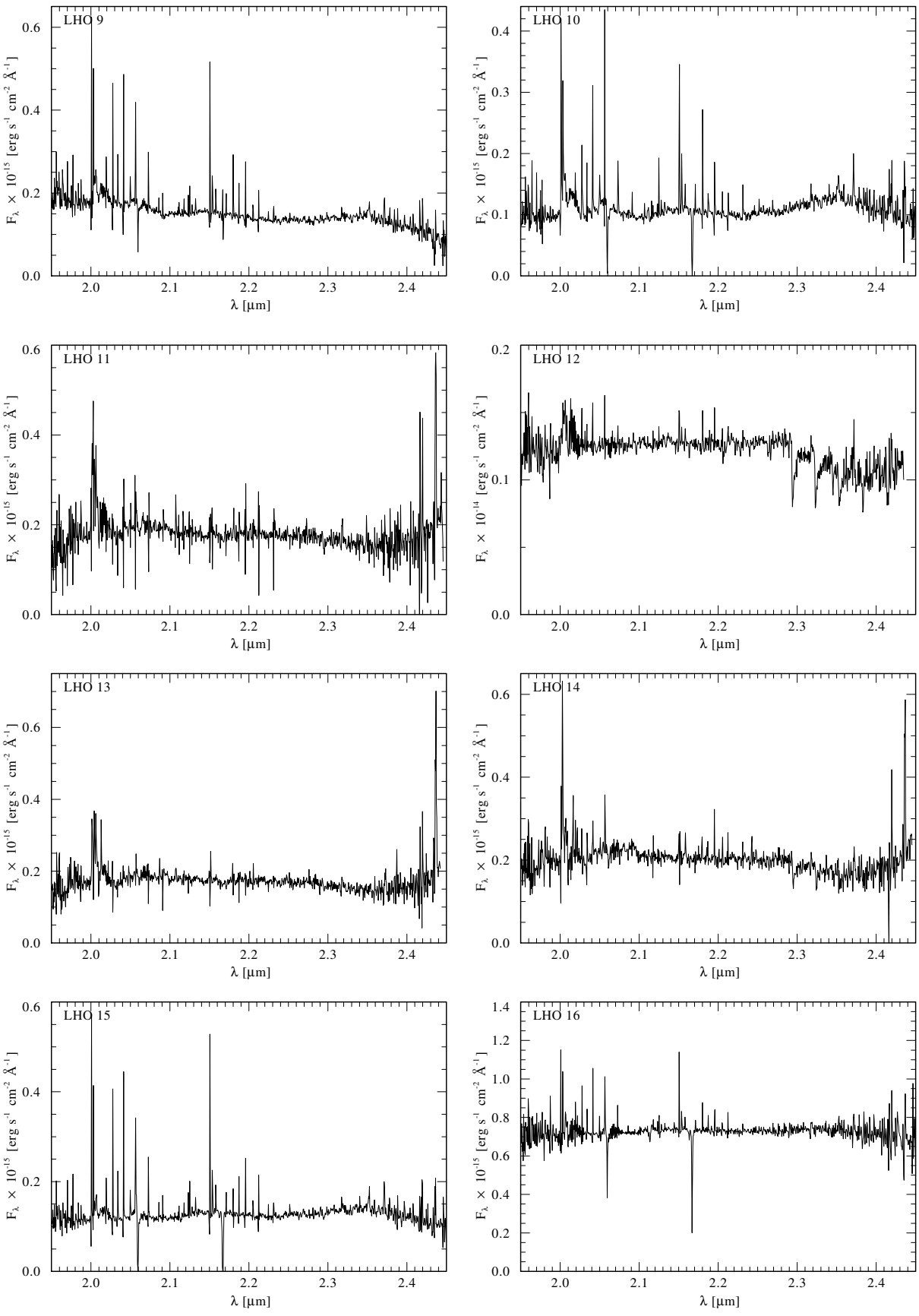

Figure B.1: Spectral atlas (continued).

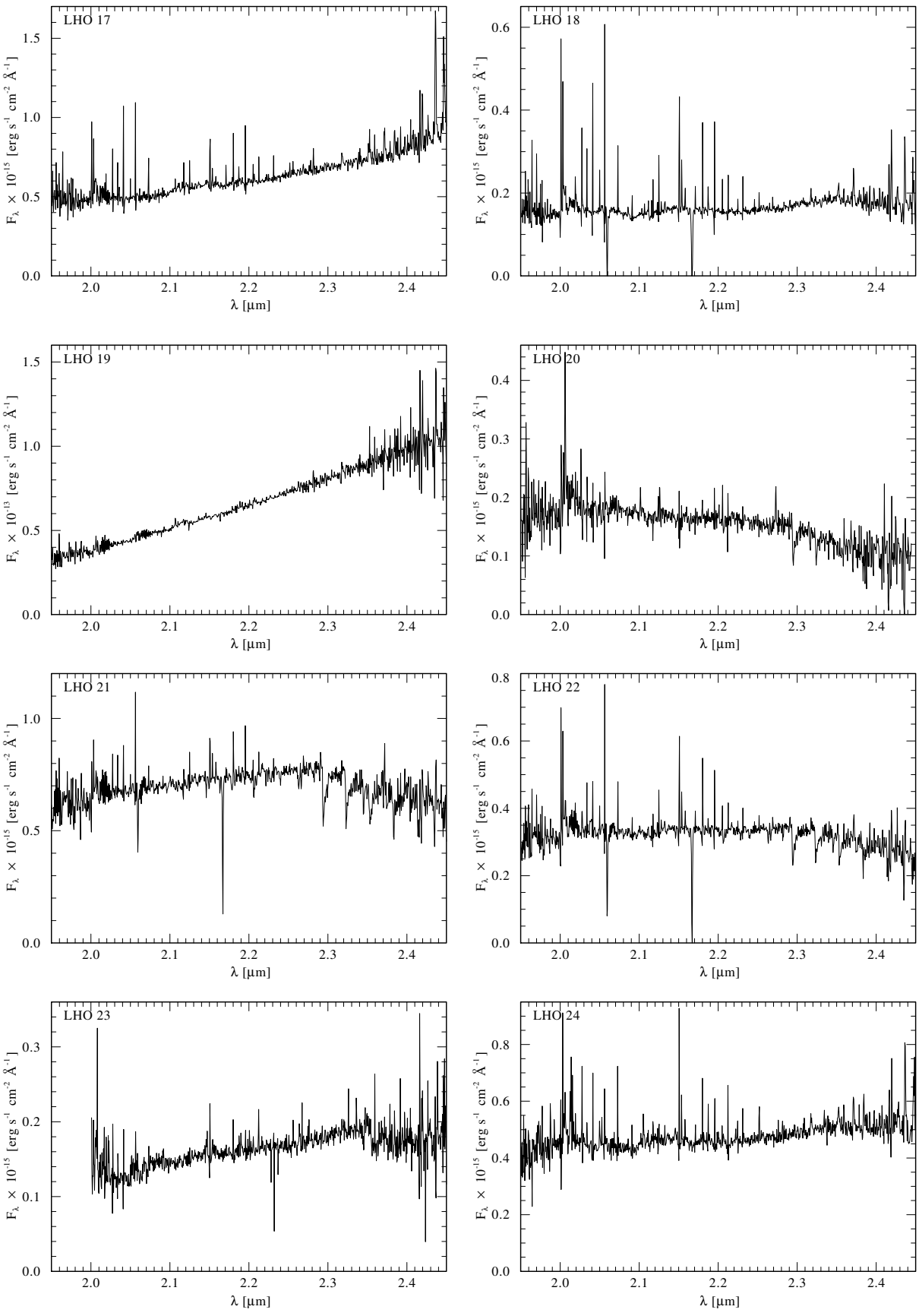

Figure B.1: Spectral atlas (continued).

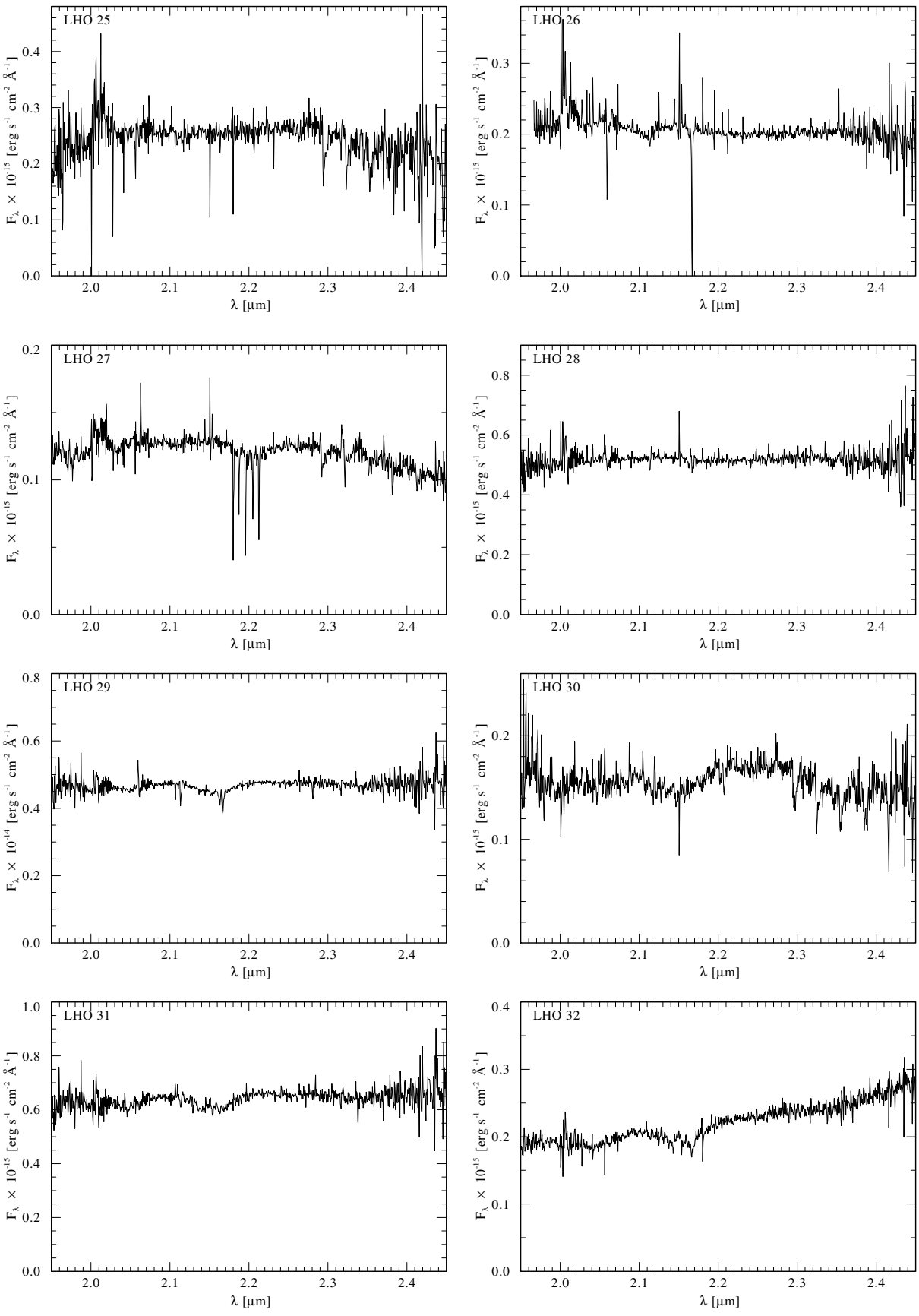

Figure B.1: Spectral atlas (continued).

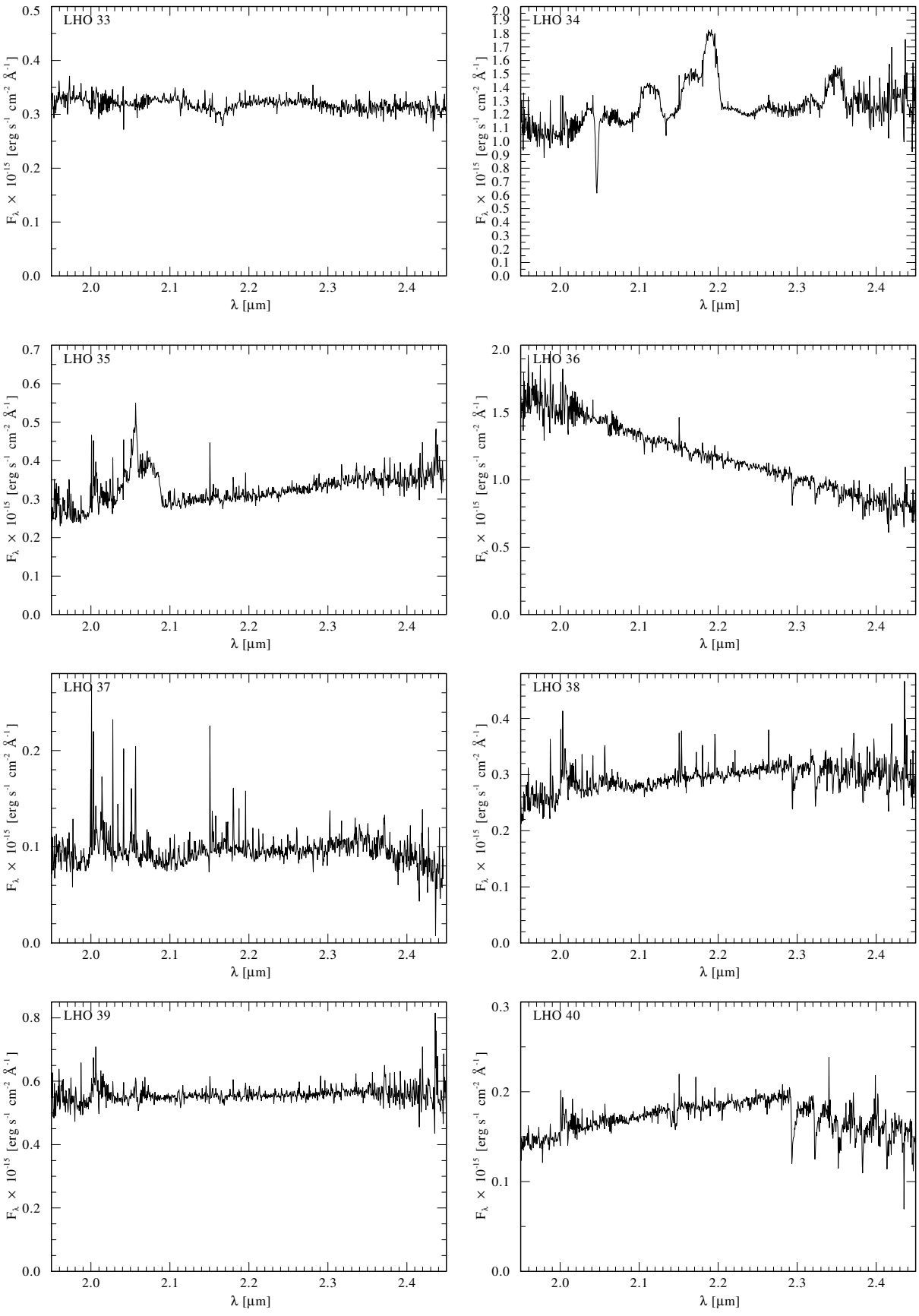

Figure B.1: Spectral atlas (continued).

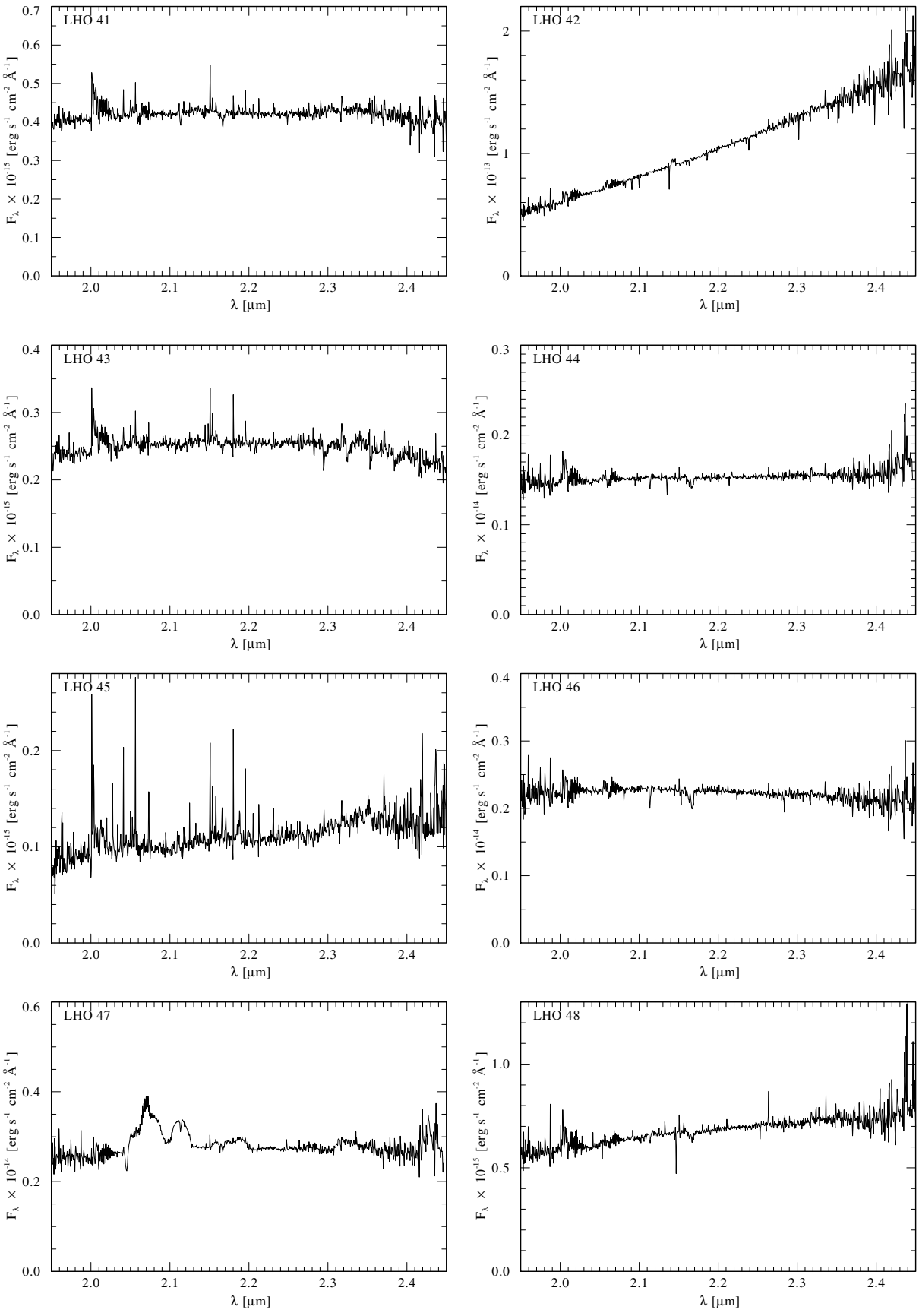

Figure B.1: Spectral atlas (continued).

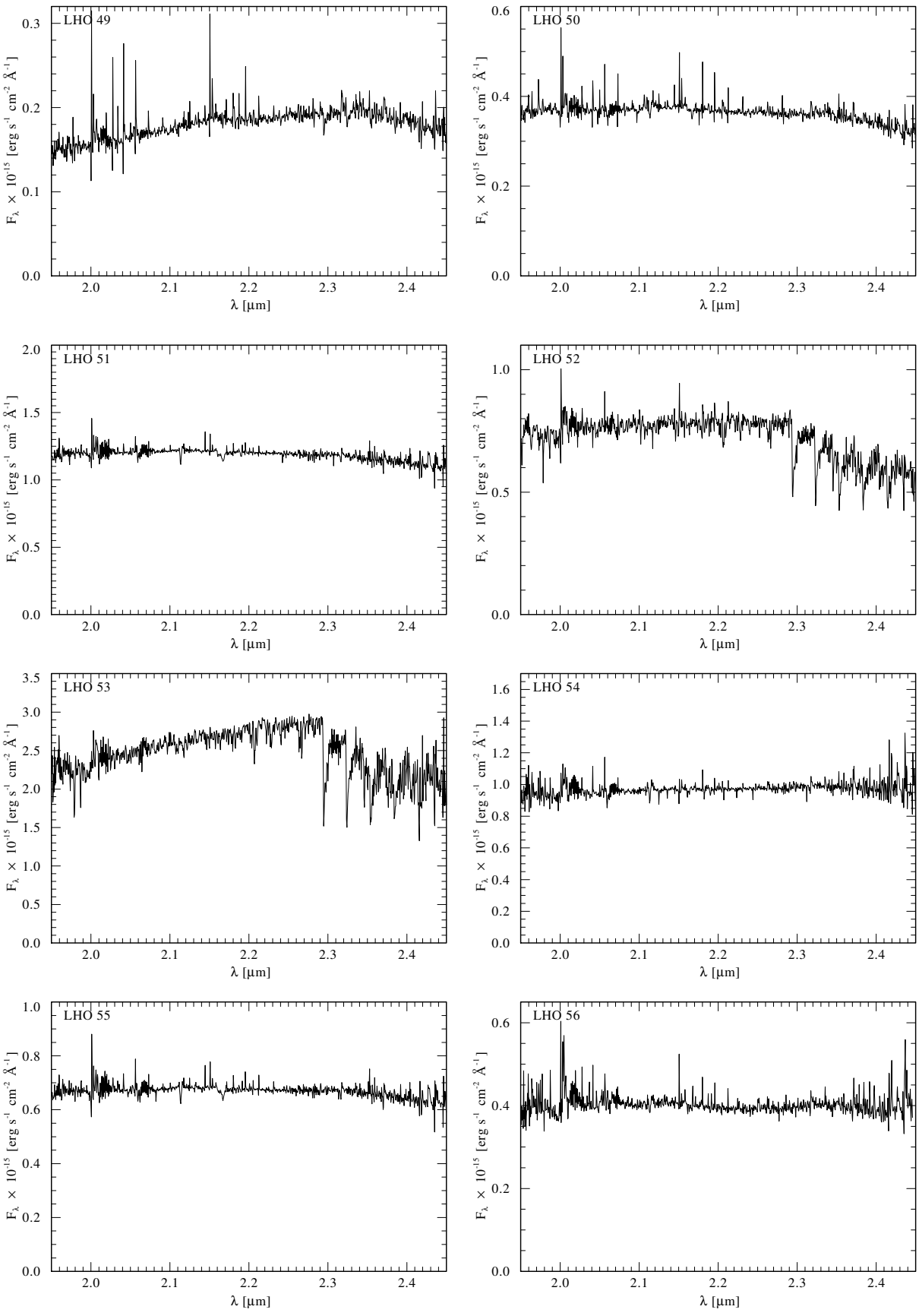

Figure B.1: Spectral atlas (continued).

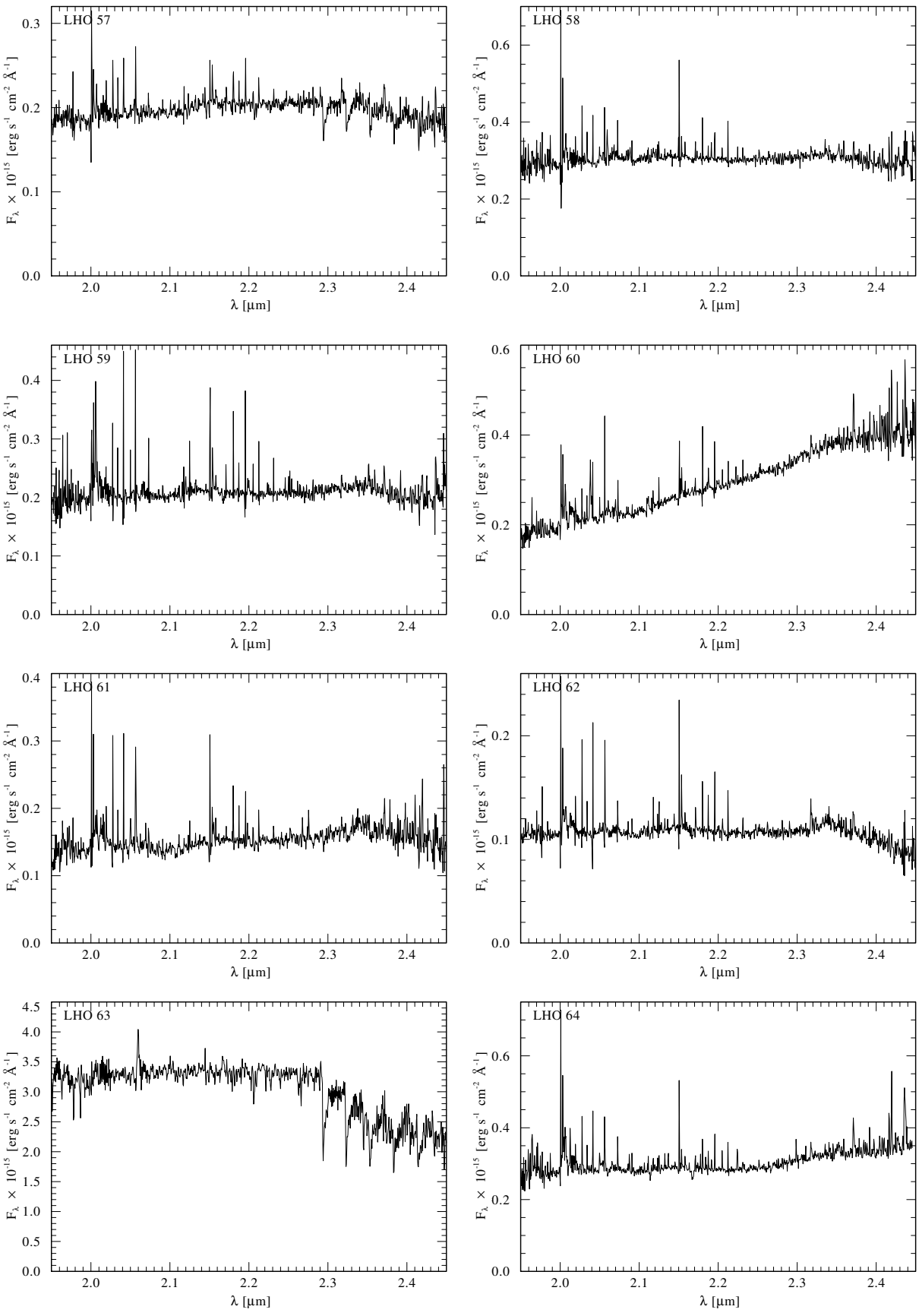

Figure B.1: Spectral atlas (continued).

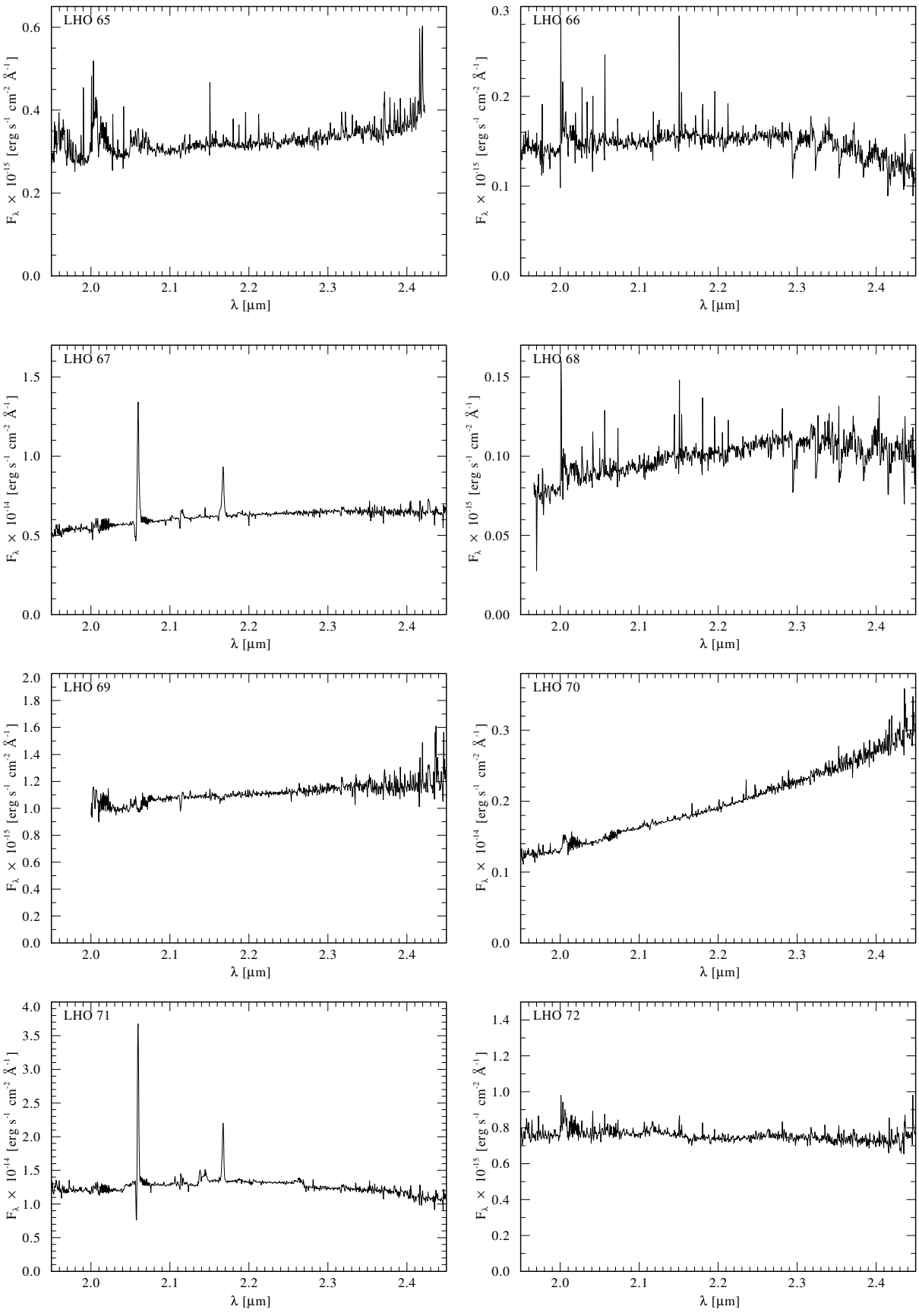

Figure B.1: Spectral atlas (continued).

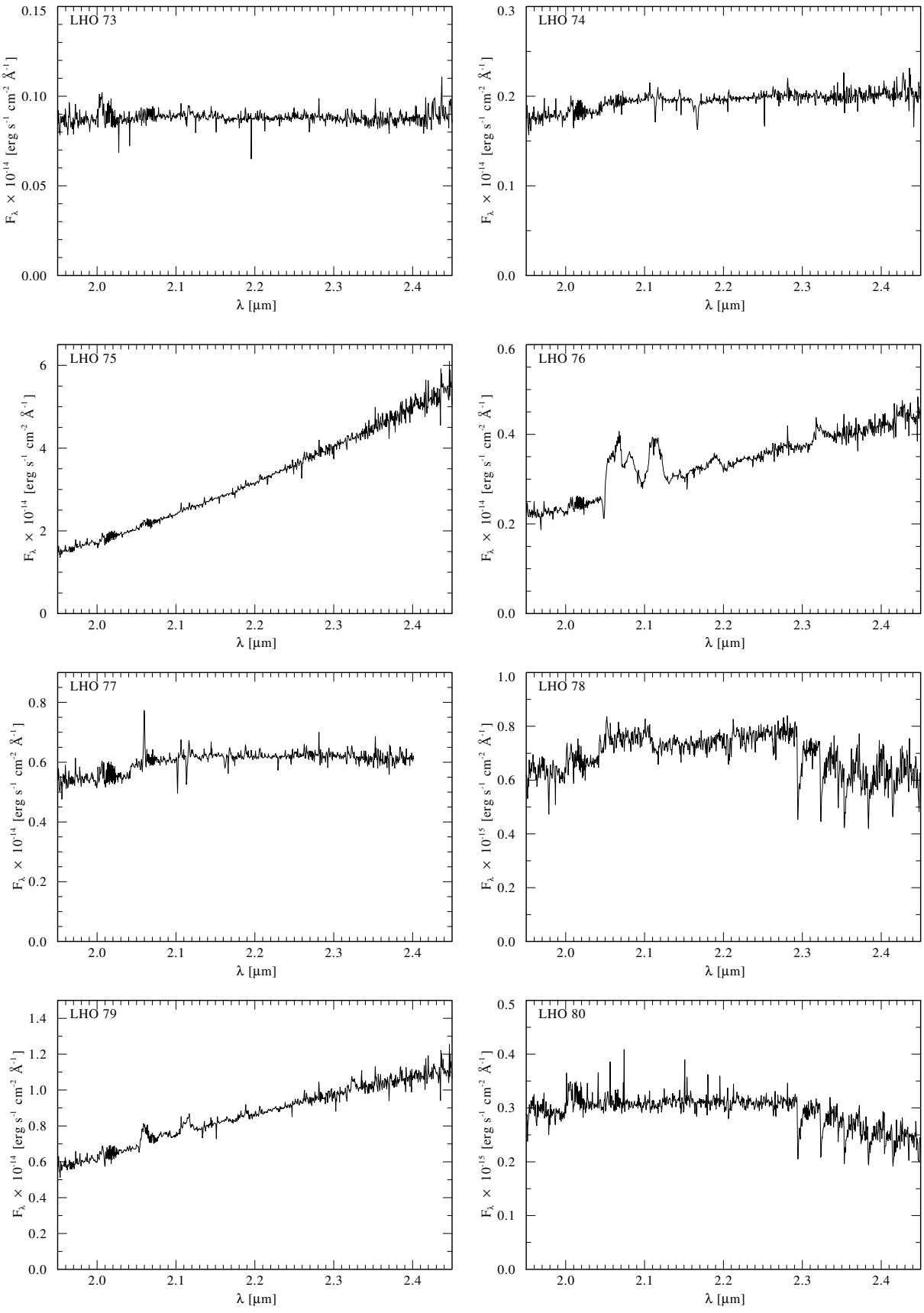

Figure B.1: Spectral atlas (continued).

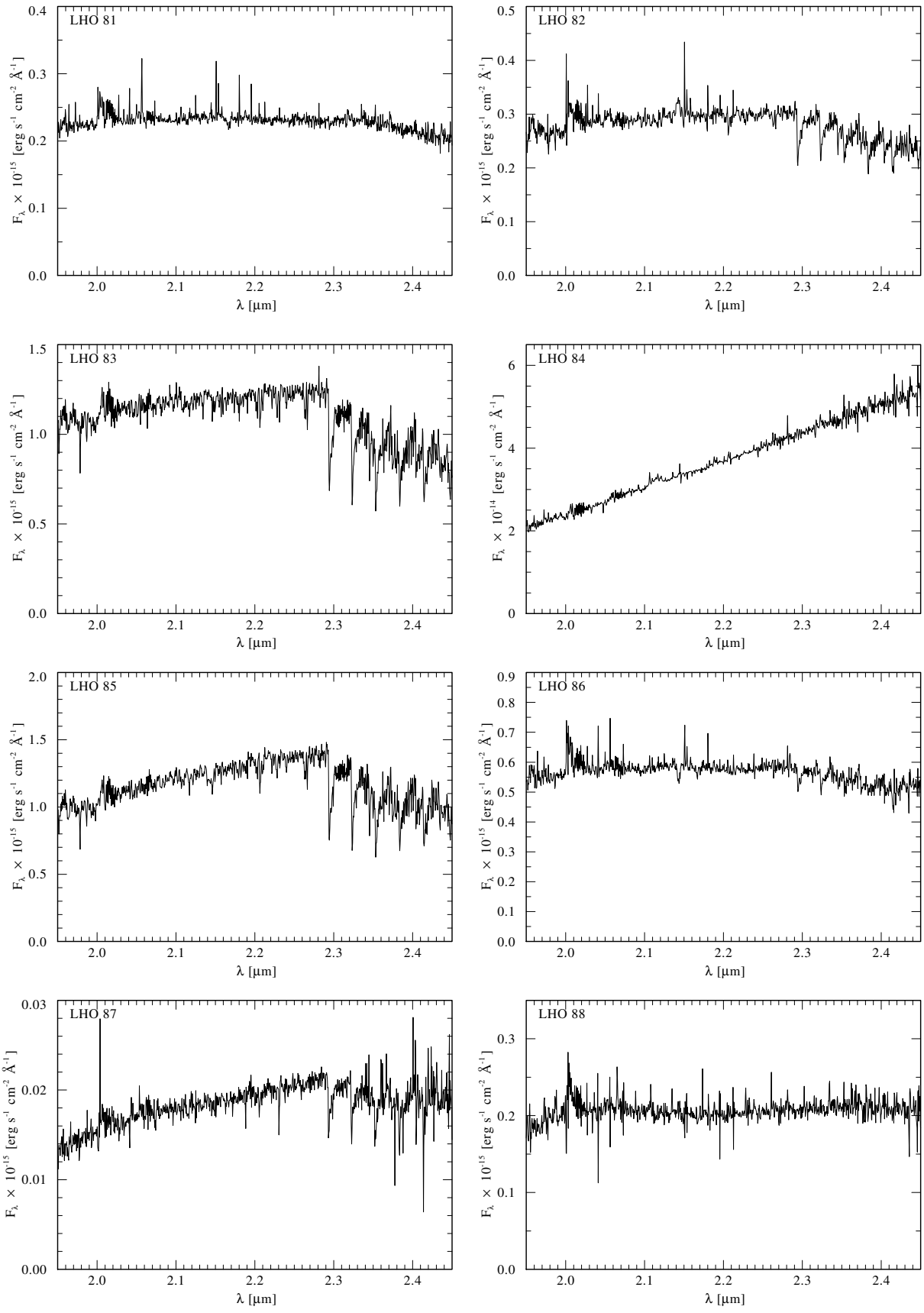

Figure B.1: Spectral atlas (continued).

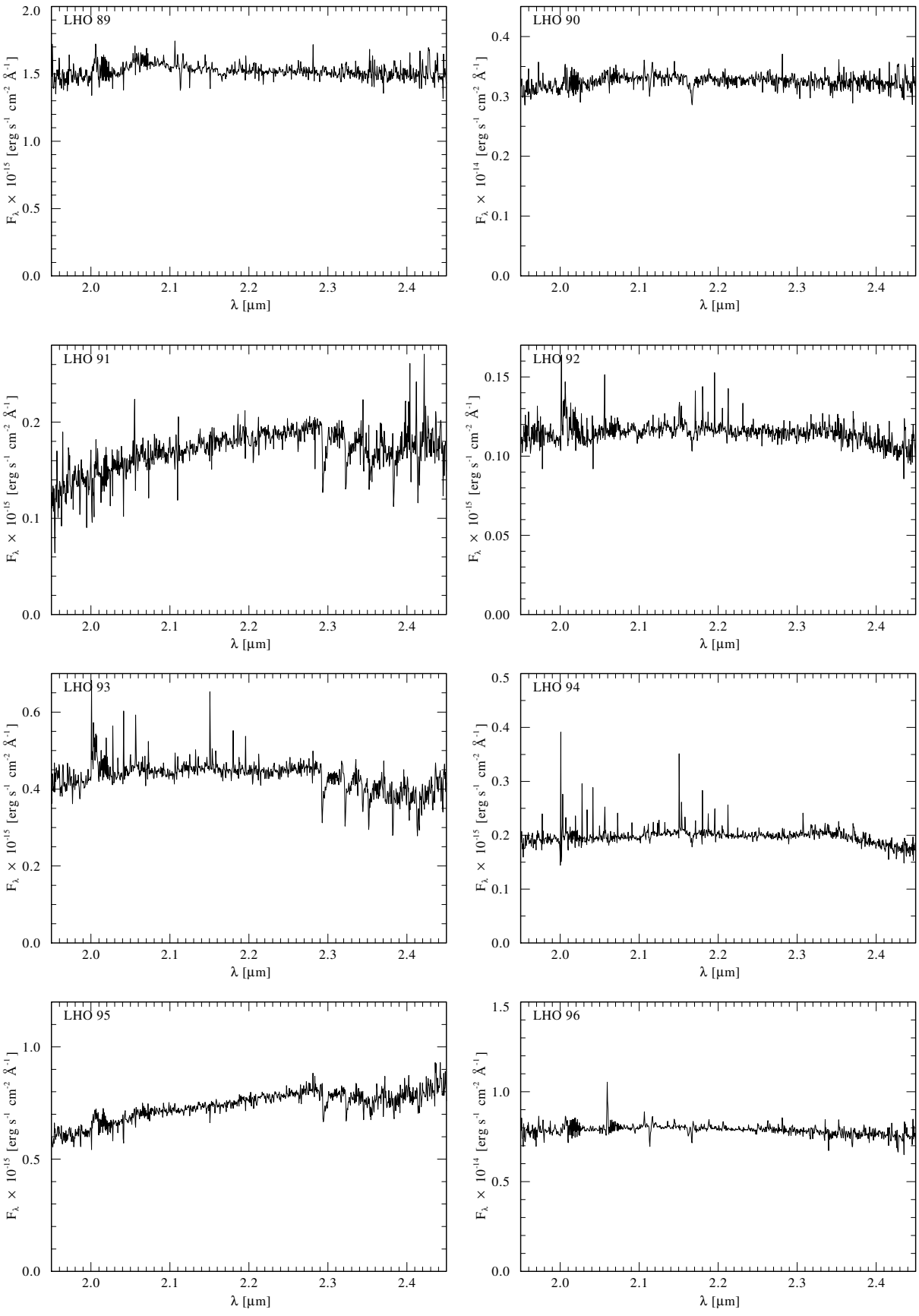

Figure B.1: Spectral atlas (continued).

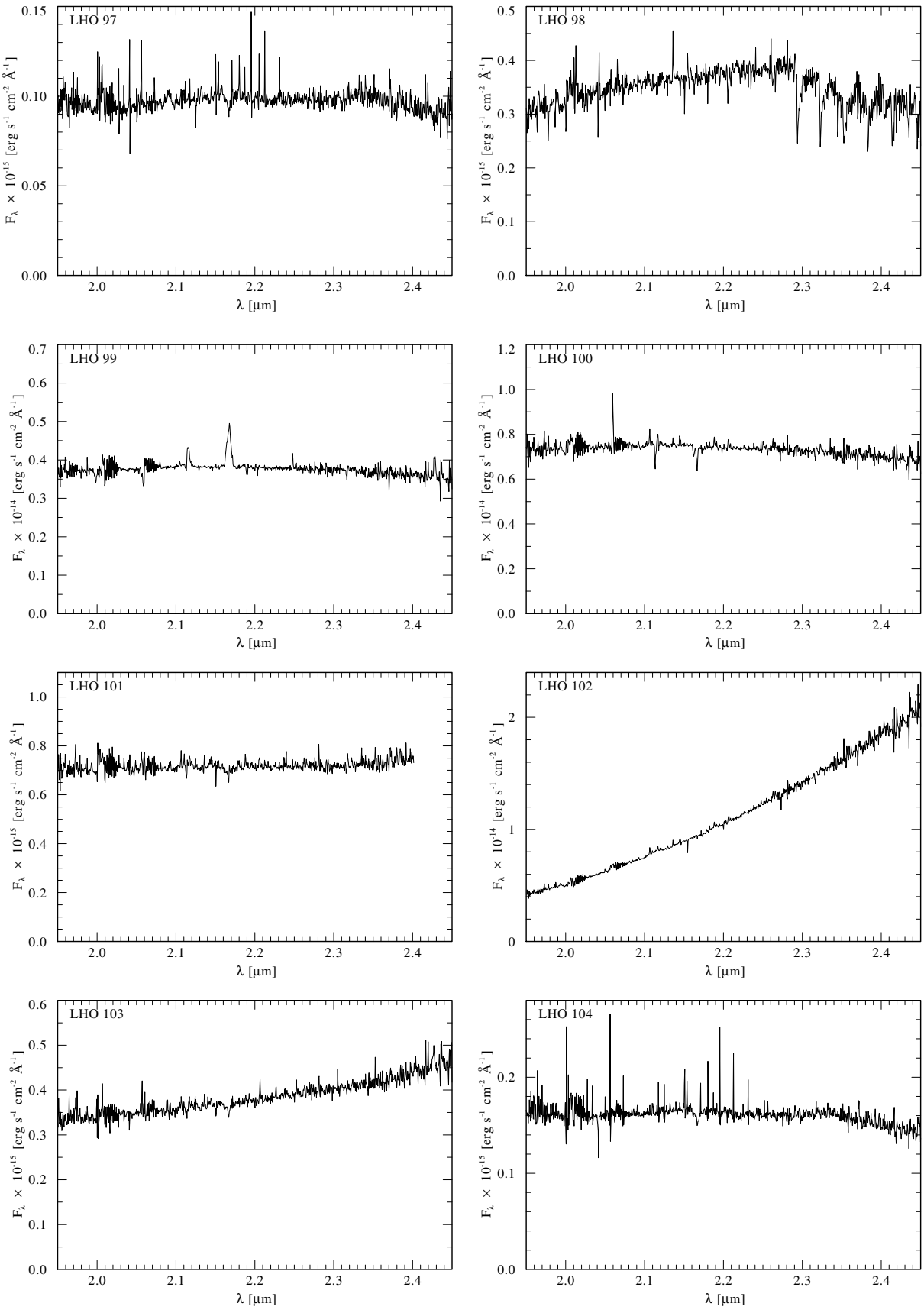

Figure B.1: Spectral atlas (continued).

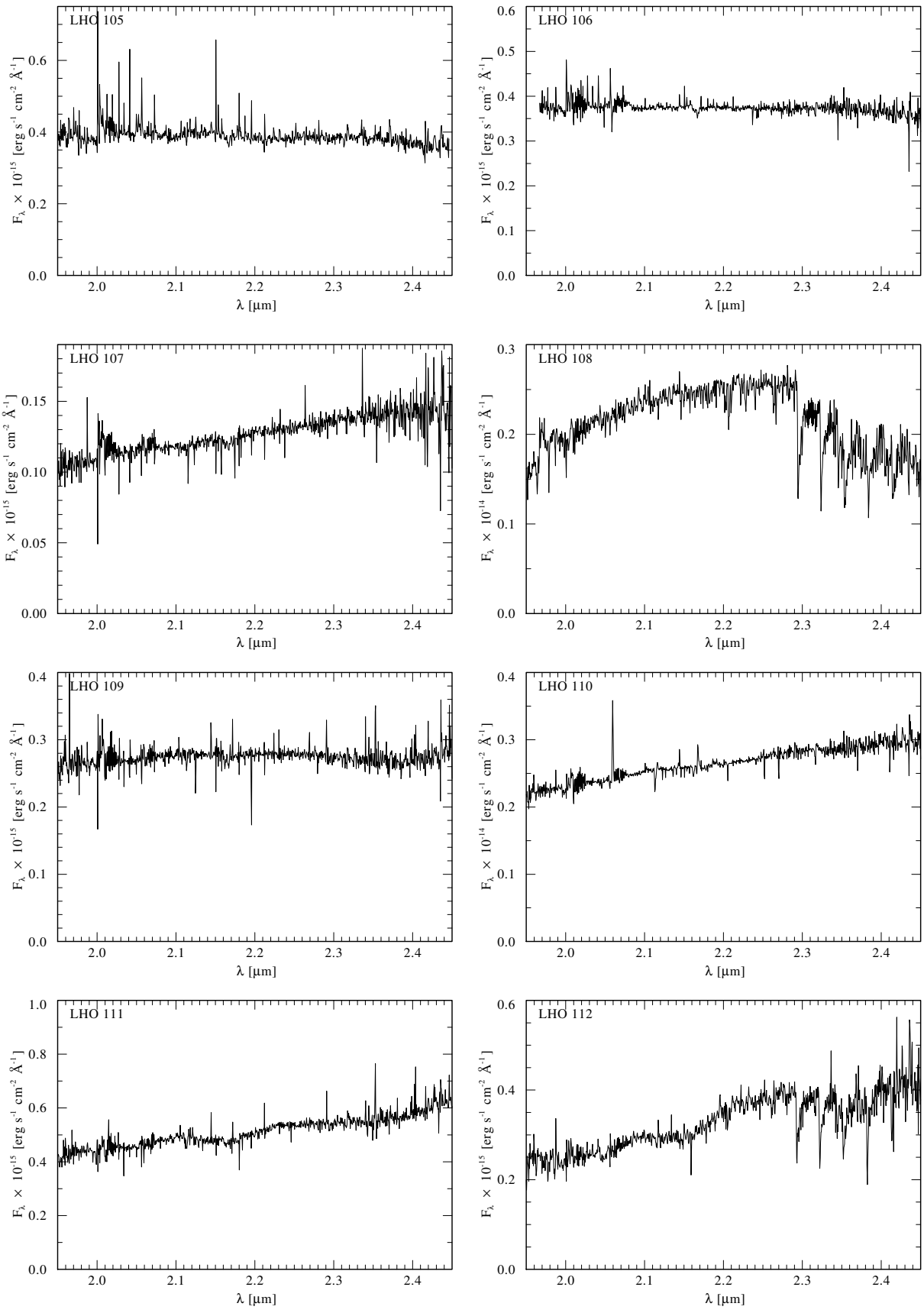

Figure B.1: Spectral atlas (continued).

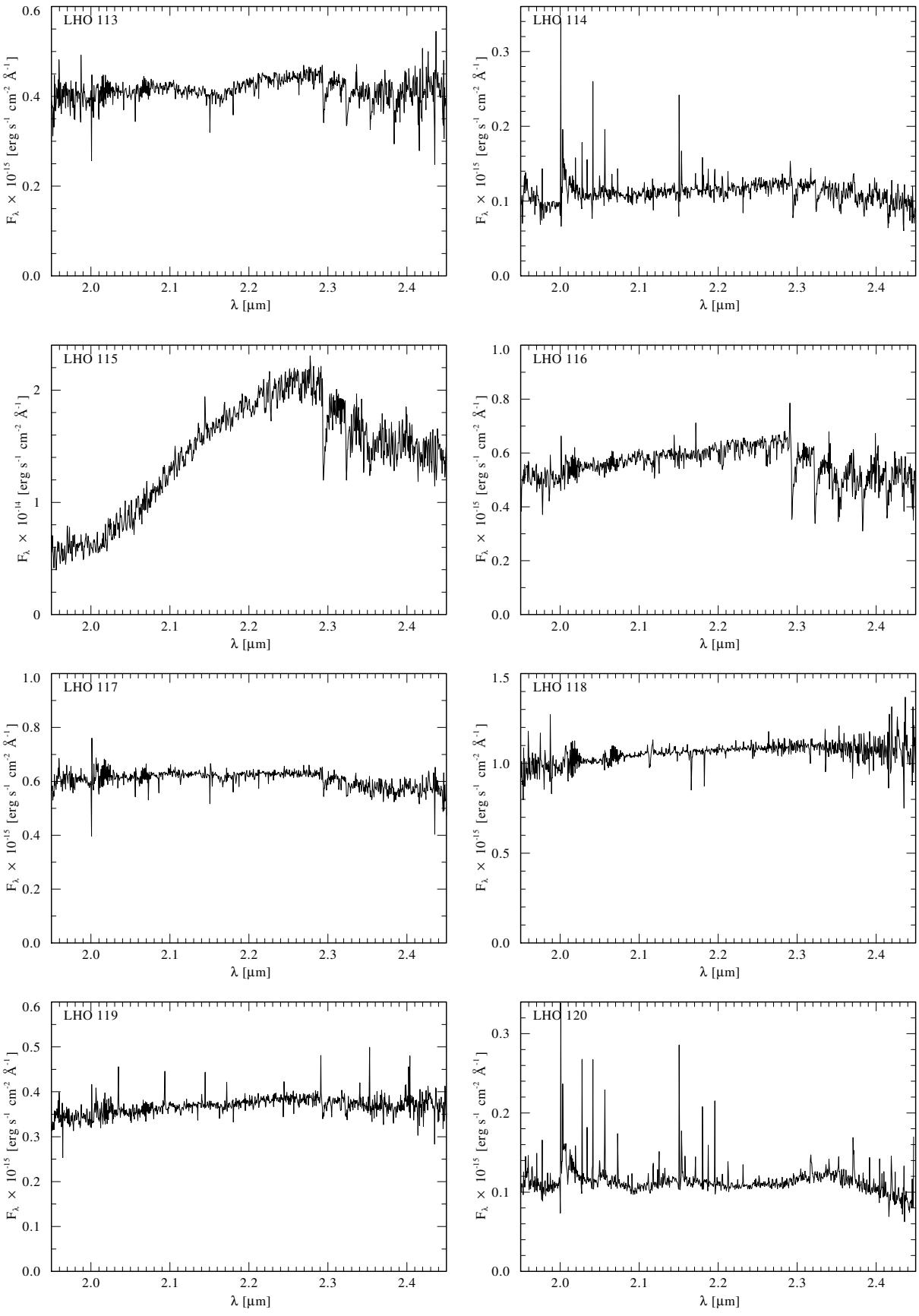

Figure B.1: Spectral atlas (continued).

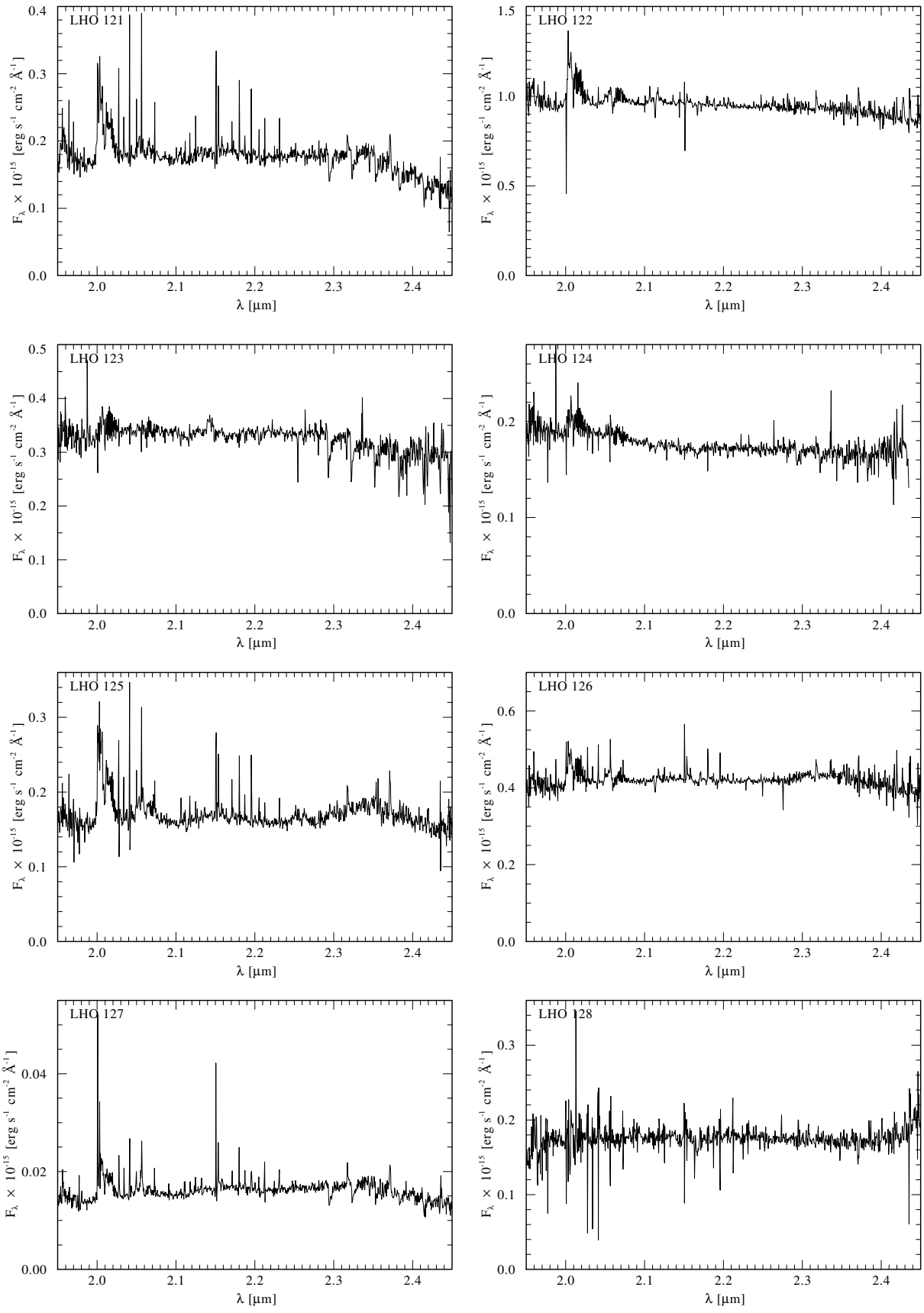

Figure B.1: Spectral atlas (continued).

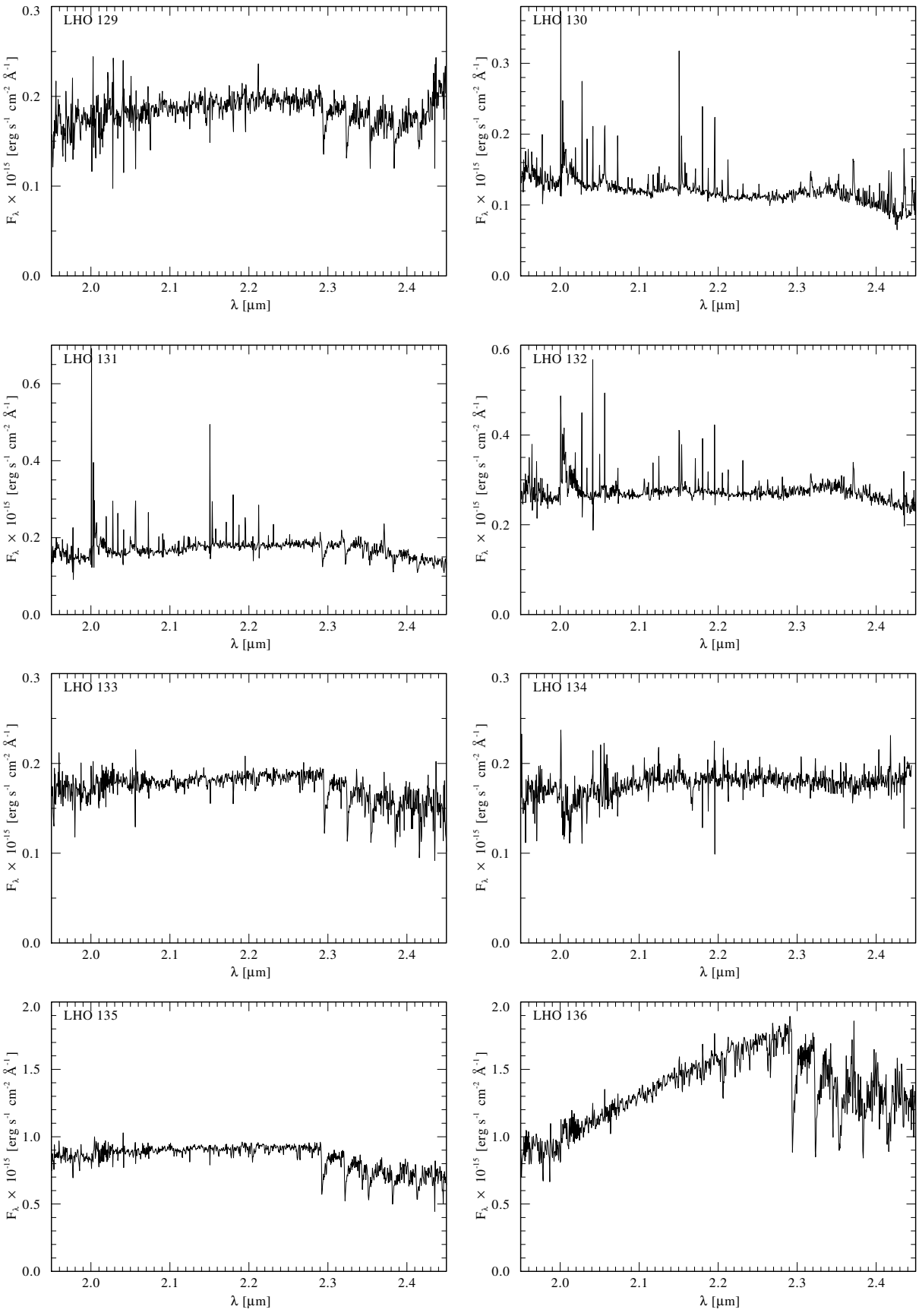

Figure B.1: Spectral atlas (continued).

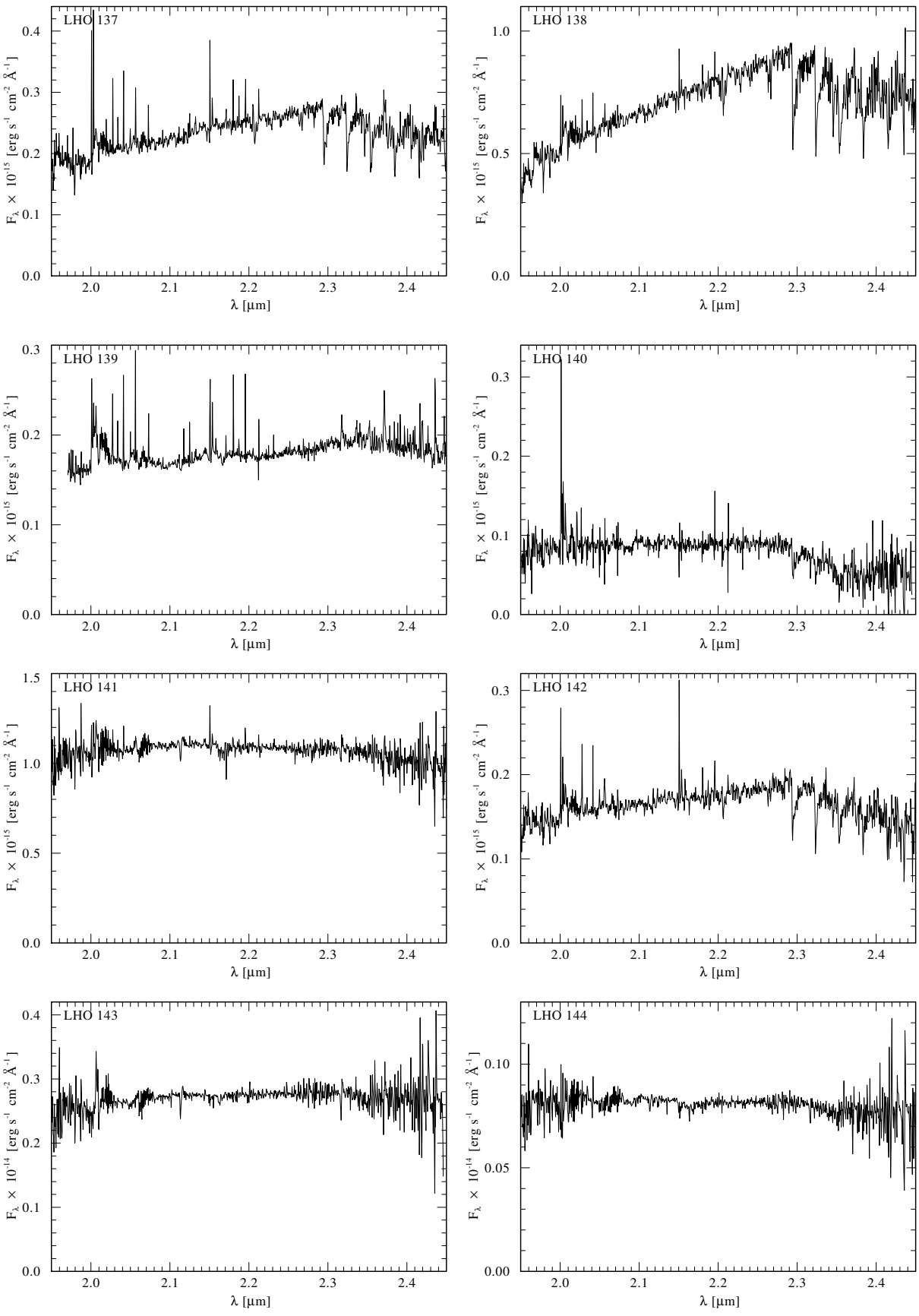

Figure B.1: Spectral atlas (continued).

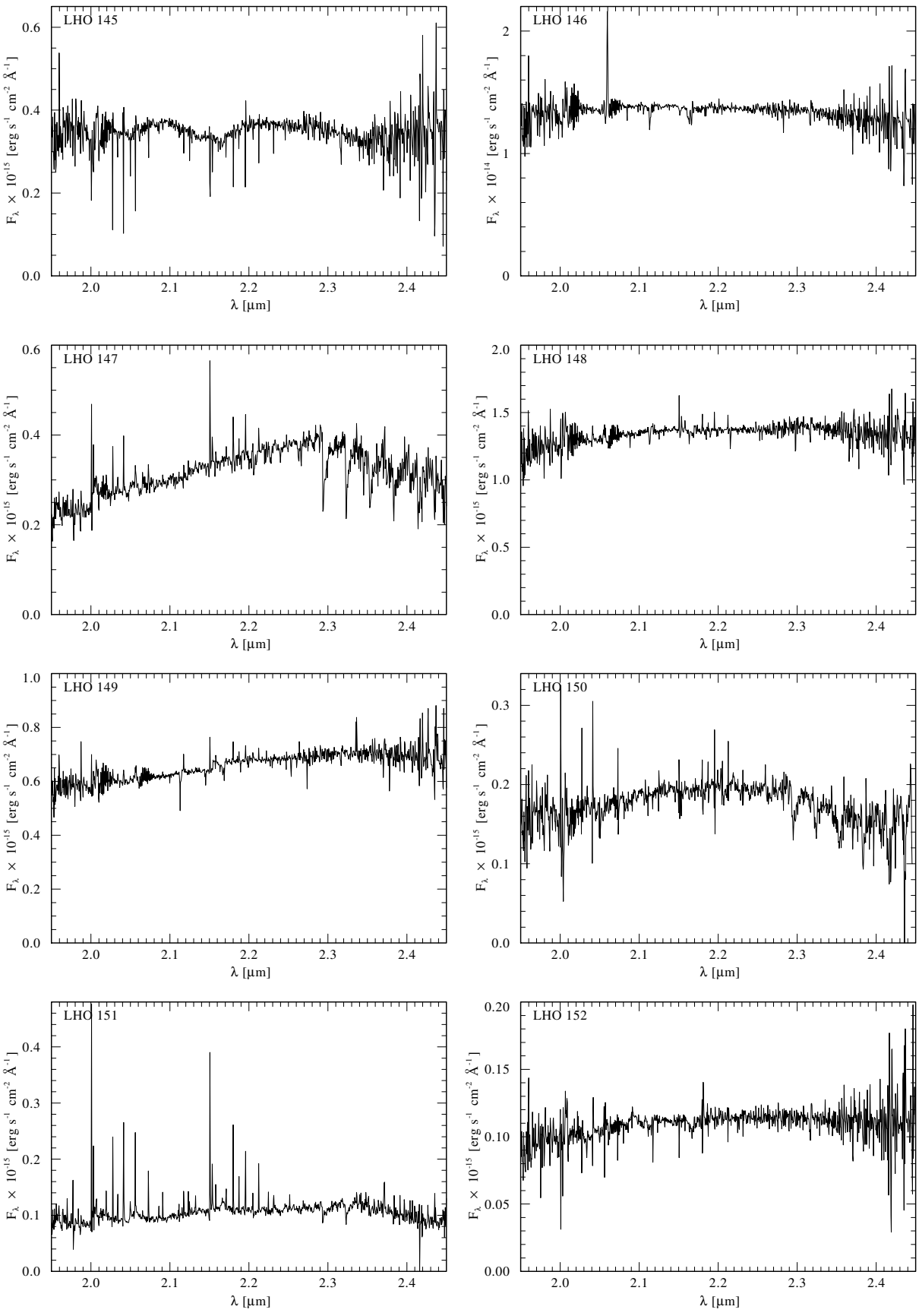

Figure B.1: Spectral atlas (continued).

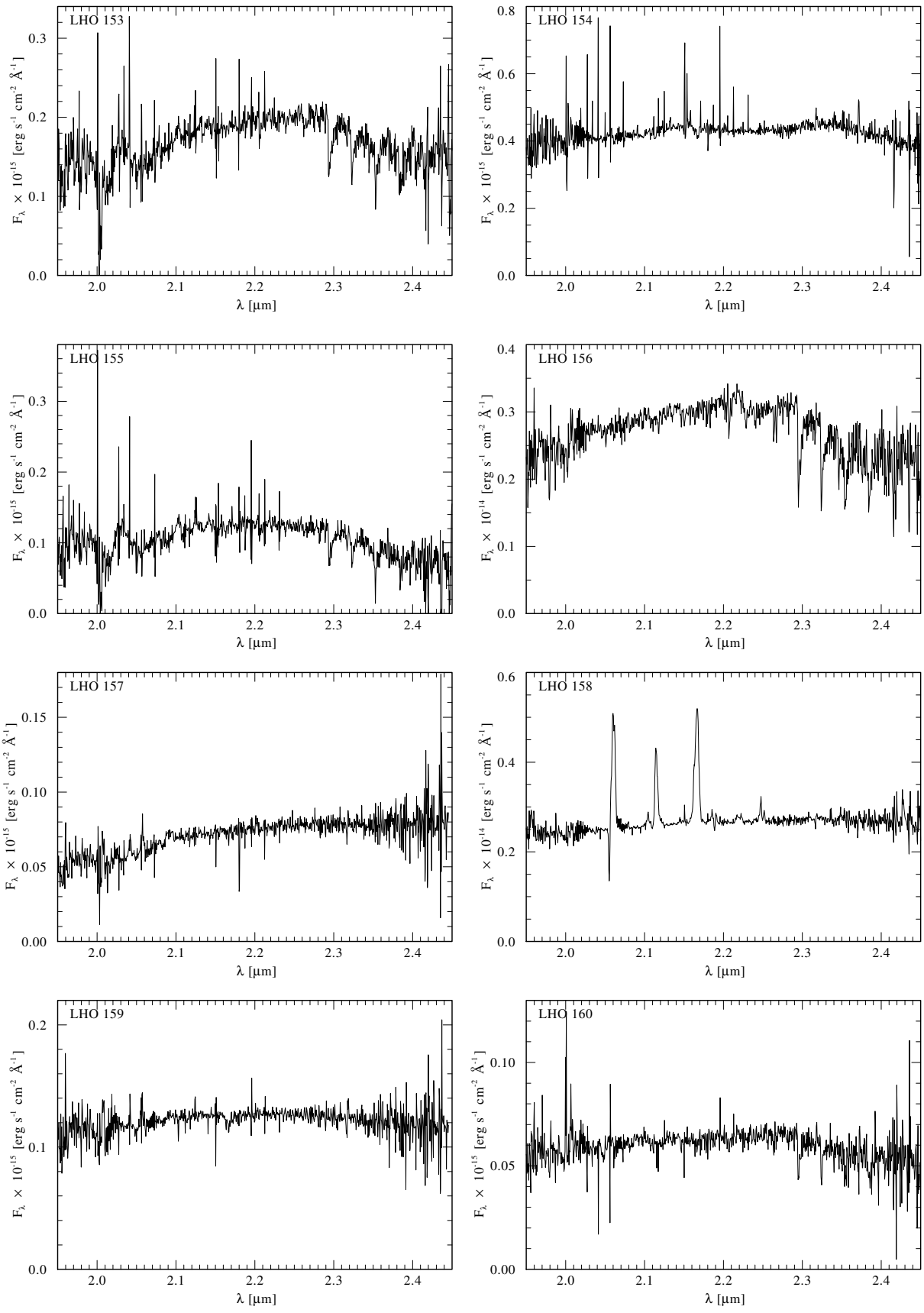

Figure B.1: Spectral atlas (continued).

Bibliography

Abuter, R., Schreiber, J., Eisenhauer, F., et al. 2006, New Astronomy Review, 50, 398

Auer, L. H. & Mihalas, D. 1970, MNRAS, 149, 65

Barniske, A. 2008, PhD thesis, Universität Postdam

Barniske, A., Oskinova, L. M., & Hamann, W.-R. 2008, A&A, 486, 971

Blitz, L., Binney, J., Lo, K. Y., Bally, J., & Ho, P. T. P. 1993, Nature, 361, 417

Blum, R. D., Schaerer, D., Pasquali, A., et al. 2001, AJ, 122, 1875

Burton, W. B. & Gordon, M. A. 1978, A&A, 63, 7

Castor, J. I., Abbott, D. C., & Klein, R. I. 1975, ApJ, 195, 157

Clark, J. S., Larionov, V. M., & Arkharov, A. 2005a, A&A, 435, 239

Clark, J. S., Negueruela, I., Crowther, P. A., & Goodwin, S. P. 2005b, A&A, 434, 949

Cohen, M., Wheaton, W. A., & Megeath, S. T. 2003, AJ, 126, 1090

Crowther, P. A. 2007, ARA&A, 45, 177

Crowther, P. A., Hadfield, L. J., Clark, J. S., Negueruela, I., & Vacca, W. D. 2006, MNRAS, 372, 1407

Davies, B., Origlia, L., Kudritzki, R.-P., et al. 2009, ApJ, 694, 46

de Vaucouleurs, G. 1964, in IAU Symposium, Vol. 20, The Galaxy and the Magellanic Clouds, ed. F. J. Kerr, 195

Eckart, A., Moultaka, J., Viehmann, T., Straubmeier, C., & Mouawad, N. 2004, ApJ, 602, 760

Figer, D. F. 1995, PhD thesis, AA(UNIVERSITY OF CALIFORNIA, LOS ANGELES.)

Figer, D. F. 2004, in Astronomical Society of the Pacific Conference Series, Vol. 322, The Formation and Evolution of Massive Young Star Clusters, ed. H. J. G. L. M. Lamers, L. J. Smith, & A. Nota, 49

Figer, D. F., McLean, I. S., & Morris, M. 1999a, ApJ, 514, 202

Figer, D. F., McLean, I. S., & Najarro, F. 1997, ApJ, 486, 420

Figer, D. F., Morris, M., Geballe, T. R., et al. 1999b, ApJ, 525, 759

Figer, D. F., Morris, M., Kim, S. S., & Serabyn, E. 1999c, in Astronomical Society of the Pacific Conference Series, Vol. 186, The Central Parsecs of the Galaxy, ed. H. Falcke, A. Cotera, W. J. Duschl, F. Melia, & M. J. Rieke, 329

Figer, D. F., Najarro, F., Morris, M., et al. 1998, ApJ, 506, 384

Geballe, T. R., Najarro, F., & Figer, D. F. 2000, ApJ, 530, L97

Giveon, U., Sternberg, A., Lutz, D., Feuchtgruber, H., & Pauldrach, A. W. A. 2002, ApJ, 566, 880

Glass, I. S., Matsumoto, S., Carter, B. S., & Sekiguchi, K. 1999, MNRAS, 304, L10

Glass, I. S., Moneti, A., & Moorwood, A. F. M. 1990, MNRAS, 242, 55P

González-Fernández, C., Cabrera-Lavers, A., Hammersley, P. L., & Garzón, F. 2008, A&A, 479, 131

Goorvitch, D. 1994, ApJS, 95, 535

Gorlova, N., Lobel, A., Burgasser, A. J., et al. 2006, ApJ, 651, 1130

Gräfener, G. & Hamann, W.-R. 2003, in IAU Symposium, 190

Gräfener, G. 1999, PhD thesis, Universität Postdam

Gräfener, G. & Hamann, W.-R. 2005, A&A, 432, 633

Gräfener, G. & Hamann, W.-R. 2008, A&A, 482, 945

Gräfener, G., Koesterke, L., & Hamann, W.-R. 2002, A&A, 387, 244

Groh, J. H., Hillier, D. J., Damineli, A., et al. 2009, ArXiv e-prints

Hamann, W.-R. & Gräfener, G. 2004, A&A, 427, 697

Hamann, W.-R., Gräfener, G., & Liermann, A. 2006, A&A, 457, 1015

Hamann, W.-R. & Koesterke, L. 1998, A&A, 333, 251

Hamann, W.-R., Koesterke, L., & Wessolowski, U. 1995, A&A, 299, 151

Hanson, M. M., Conti, P. S., & Rieke, M. J. 1996, ApJS, 107, 281

Hanson, M. M., Kudritzki, R.-P., Kenworthy, M. A., Puls, J., & Tokunaga, A. T. 2005, ApJS, 161, 154

Harayama, Y., Eisenhauer, F., & Martins, F. 2008, ApJ, 675, 1319

Hunter, D. A., O'Connell, R. W., Gallagher, J. S., & Smecker-Hane, T. A. 2000, AJ, 120, 2383

Ivezić, Ž. & Elitzur, M. 1997, MNRAS, 287, 799

Kleinmann, S. G. & Hall, D. N. B. 1986, ApJS, 62, 501

Kobayashi, Y., Okuda, H., Sato, S., Jugaku, J., & Dyck, H. M. 1983, PASJ, 35, 101

Koyama, K., Inui, T., Hyodo, Y., et al. 2007, PASJ, 59, 221

Kraus, M. 2009, A&A, 494, 253

Kroupa, P. 2002, MNRAS, 330, 707

Kudritzki, R.-P. & Puls, J. 2000, ARA&A, 38, 613

Kuijken, K. 1996, in Astronomical Society of the Pacific Conference Series, Vol. 91, IAU Colloq. 157: Barred Galaxies, ed. R. Buta, D. A. Crocker, & B. G. Elmegreen, 504

Kurucz, R. L. 1993, VizieR Online Data Catalog, 6039, 0

Lang, C. C., Figer, D. F., Goss, W. M., & Morris, M. 1999, AJ, 118, 2327

Lang, C. C., Goss, W. M., & Wood, D. O. S. 1997, ApJ, 474, 275

Lang, C. C., Johnson, K. E., Goss, W. M., & Rodríguez, L. F. 2005, AJ, 130, 2185

Lang, C. C., Palmer, P., & Goss, W. M. 2008, ArXiv e-prints

Langer, N. 1989, A&A, 210, 93

Langer, N., Hamann, W.-R., Lennon, M., et al. 1994, A&A, 290, 819

Law, C. & Yusef-Zadeh, F. 2004, ApJ, 611, 858

Law, C. & Yusef-Zadeh, F. 2005, in X-Ray and Radio Connections (eds. L.O. Sjouwerman and K.K Dyer) Published electronically by NRAO, http://www.aoc.nrao.edu/events/xraydio Held 3-6 February 2004 in Santa Fe, New Mexico, USA, (E3.06) 5 pages, ed. L. O. Sjouwerman & K. K. Dyer

Leitherer, C. & Robert, C. 1991, ApJ, 377, 629

Lejeune, T. & Schaerer, D. 2001, A&A, 366, 538

Levesque, E. M., Massey, P., Olsen, K. A. G., et al. 2005, ApJ, 628, 973

Liermann, A. & Hamann, W.-R. 2008, in Clumping in Hot-Star Winds, ed. W.-R. Hamann, A. Feldmeier, & L. M. Oskinova, 247

Liermann, A., Hamann, W.-R., & Oskinova, L. M. 2009, A&A, 494, 1137

Maeder, A., Meynet, G., Ekström, S., Hirschi, R., & Georgy, C. 2008, in IAU Symposium, Vol. 250, IAU Symposium, 3–16

Maness, H., Martins, F., Trippe, S., et al. 2007, ApJ, 669, 1024

Martins, F., Hillier, D. J., Paumard, T., et al. 2008, A&A, 478, 219

Martins, F., Schaerer, D., & Hillier, D. J. 2005, A&A, 436, 1049

Mengel, S. & Tacconi-Garman, L. E. 2007, A&A, 466, 151

Meynet, G. & Maeder, A. 2003a, A&A, 404, 975

Meynet, G. & Maeder, A. 2003b, A&A, 404, 975

Meynet, G., Maeder, A., Schaller, G., Schaerer, D., & Charbonnel, C. 1994, A&AS, 103, 97

Mihalas, D., Kunasz, P. B., & Hummer, D. G. 1976, ApJ, 210, 419

Mihalas, D. & Mihalas, B. W. 1984, Foundations of Radiation Hydrodynamics (Oxford University Press, Inc.)

Moffat, A. F. J., Drissen, L., Lamontagne, R., & Robert, C. 1988, ApJ, 334, 1038

Monet, D. G., Levine, S. E., Canzian, B., et al. 2003, AJ, 125, 984

Moneti, A., Glass, I., & Moorwood, A. 1992, MNRAS, 258, 705

Moneti, A., Glass, I. S., & Moorwood, A. F. M. 1994, MNRAS, 268, 194

Moneti, A., Stolovy, S., Blommaert, J. A. D. L., Figer, D. F., & Najarro, F. 2001, A&A, 366, 106

Morris, P. W., Eenens, P. R. J., Hanson, M. M., Conti, P. S., & Blum, R. D. 1996, ApJ, 470, 597

Nagata, T., Hyland, A. R., Straw, S. M., Sato, S., & Kawara, K. 1993, ApJ, 406, 501

Nagata, T., Woodward, C. E., Shure, M., Pipher, J. L., & Okuda, H. 1990, ApJ, 351, 83

Najarro, F. 2006, Journal of Physics Conference Series, 54, 224

Najarro, F., Figer, D. F., Hillier, D. J., Geballe, T. R., & Kudritzki, R. P. 2009, ApJ, 691, 1816

Najarro, F., Figer, D. F., Hillier, D. J., & Kudritzki, R. P. 2004, ApJ, 611, L105

Nakanishi, H. & Sofue, Y. 2006, PASJ, 58, 847

Nugis, T. & Lamers, H. J. G. L. M. 2000, A&A, 360, 227

Okuda, H., Shibai, H., Kobayashi, Y., et al. 1987, in IAU Symposium, Vol. 115, Star Forming Regions, ed. M. Peimbert & J. Jugaku, 556

Okuda, H., Shibai, H., Nakagawa, T., et al. 1989, in IAU Symposium, Vol. 136, The Center of the Galaxy, ed. M. Morris, 281

Okuda, H., Shibai, H., Nakagawa, T., et al. 1990, ApJ, 351, 89

Oskinova, L. M., Feldmeier, A., & Hamann, W.-R. 2006, MNRAS, 372, 313

Paumard, T., Genzel, R., Martins, F., et al. 2006, ApJ, 643, 1011

Portegies Zwart, S. F., Makino, J., McMillan, S. L. W., & Hut, P. 2002, ApJ, 565, 265

Prinja, R. K. & Howarth, I. D. 1988, MNRAS, 233, 123

Puls, J., Kudritzki, R.-P., Herrero, A., et al. 1996, A&A, 305, 171

Puls, J., Markova, N., Scuderi, S., et al. 2006, A&A, 454, 625

Reid, M. J. 1993, ARA&A, 31, 345

Rousselot, P., Lidman, C., Cuby, J.-G., Moreels, G., & Monnet, G. 2000, A&A, 354, 1134

Salpeter, E. E. 1955, ApJ, 121, 161

Scheffler, H. & Elsasser, H. 1990, Physik der Sterne und der Sonne, 2nd edn. (Mannheim: BI-Wissenschaftsverlag)

Schmutz, W., Hamann, W.-R., & Wessolowski, U. 1989, A&A, 210, 236

Schnurr, O., Casoli, J., Chené, A.-N., Moffat, A. F. J., & St-Louis, N. 2008, MNRAS, 389, L38

Seaton, M. J. 1958, Reviews of Modern Physics, 30, 979

Skrutskie, M. F., Cutri, R. M., Stiening, R., et al. 2006, AJ, 131, 1163

Skrutskie, M. F., Schneider, S. E., Stiening, R., et al. 1997, in Astrophysics and Space Science Library, Vol. 210, The Impact of Large Scale Near-IR Sky Surveys, ed. F. Garzon, N. Epchtein, A. Omont, B. Burton, & P. Persi, 25

Smith, L. F. 1968, MNRAS, 140, 409

Sofue, Y. 1999, in Star Formation 1999, Proceedings of Star Formation 1999, held in Nagoya, Japan, June 21 - 25, 1999, Editor: T. Nakamoto, Nobeyama Radio Observatory, p. 322-326, ed. T. Nakamoto, 322–326

Sofue, Y., Honma, M., & Omodaka, T. 2009, PASJ, 61, 227

Stahl, O., Jankovics, I., Kovács, J., et al. 2001, A&A, 375, 54

Stark, A. A., Martin, C. L., Walsh, W. M., et al. 2004, ApJ, 614, L41

Stolte, A., Brandner, W., Grebel, E. K., Lenzen, R., & Lagrange, A.-M. 2005, ApJ, 628, L113

Tsuboi, M., Handa, T., & Ukita, N. 1999, ApJS, 120, 1

Tuthill, P., Monnier, J., Tanner, A., et al. 2006, Science, 313, 935

van der Hucht, K. A. 2001, VizieR Online Data Catalog, 3215, 0

van der Hucht, K. A. 2006, A&A, 458, 453

van Genderen, A. M. 2001, A&A, 366, 508

Vink, J. S., de Koter, A., & Lamers, H. J. G. L. M. 2000, A&A, 362, 295

Wallace, L. & Hinkle, K. 1997, ApJS, 111, 445

Wang, Q. D., Dong, H., & Lang, C. 2006, MNRAS, 371, 38

Weiner, B. J. & Sellwood, J. A. 1999, ApJ, 524, 112

Wright, A. E. & Barlow, M. J. 1975, MNRAS, 170, 41

Yorke, H. W. & Sonnhalter, C. 2002, ApJ, 569, 846

Yusef-Zadeh, F. & Morris, M. 1987, ApJ, 322, 721

Zinnecker, H. & Yorke, H. W. 2007, ARA&A, 45, 481

Acknowledgments – Danksagung

> "We have a habit in writing articles published in scientific journals to make the work as finished as possible, to cover all the tracks, to not worry about the blind alleys or to describe how you had the wrong idea first, and so on. So there isn't any place to publish, in a dignified manner, what you actually did in order to get to do the work, although, there has been in these days, some interest in this kind of thing."
>
> R. Feynman, Nobel lecture (1965)

Nun, auch diese Arbeit ist mit Sicherheit nicht *as finished as possible*, obwohl ich mein Bestes gegeben habe. Für viele interessante Dinge am Wegesrand fehlte oft schlicht die Zeit, bei anderen das Fachwissen (How is this cluster dynamcis actually working out?). Und auch in dieser Arbeit finden sich keine Beschreibungen der (technischen) Fehlschläge, Sackgassen und Diskussionen, die unterwegs zu meistern waren, ebensowenig der Verzweiflung, des vorsichtigen Optimismus und der seltenen Momente des *Heureka* – das liegt sowohl am Seitenlimit, dem Anspruch nach allgemeiner Vorstellung eine wissenschaftliche Arbeit abzuliefern, und nicht zuletzt meiner fehlenden Fähigkeit dies in der geforderten *dignified manner* zu tun. Das sei der Poesie überlassen.
Stattdessen möchte ich mich bei all den Menschen bedanken, die mir während dieser Zeit so tatkräftig, diskussionfreudig, aufmunternd und helfend zu Seite gestanden haben:
Dank an ...

... Wolf-Rainer Hamann, für die Möglichkeit, die Herausforderung und das Abenteuer,

... Achim Feldmeier, für Abstecher in die Philosophie, Neurobiologie ... und Geometrie,

... Andrea Brockhaus, für die Rückendeckung,

... Ute, Cora, Lida, Helge und Thorsten für das Leben drum herum, Tee, Espressoraketen und die exzellente Keksversorgung.

Meiner Familie danke ich für ihre Geduld, Ausdauer und Unterstützung. Euer Vertrauen in mich hat mir stets Kraft gegeben.